Masterarbeit

High precision excitation, manipulation and detection of Rydberg atoms

Thomas Schmid

12. November 2013

5. Physikalisches Institut
Universität Stuttgart

Stuttgart
Universität

Hauptberichter:	Prof. Dr. Tilman Pfau
Mitberichter:	Prof. Dr. Peter Michler

A ma famille

Eingedenk der Neubegierde und Faszination – zum Beispiel
über einen vollschlanken Arm mit altertümlichem
Knochengerüst – verfasst

Contents

List of Figures

List of Tables

1. Zusammenfassung

Rydberg-Atome sind Atome mit einem Elektron oder mehreren Elektronen in einem hochangeregten Zustand, d. h. in einem Zustand mit großer Hauptquantenzahl n. Aufgrund ihrer Größe weisen Rydberg-Atome eine große Polarisierbarkeit auf, was zu einer starken Wechselwirkung zwischen den Rydberg-Atomen führt. Dieser starken Wechselwirkung verdanken die Rydberg-Atome ihren Einsatz im Feld der Quanteninformationsverarbeitung und im Feld der Quantenkommunikation.

Im Rahmen dieser Arbeit wurde ein Apparat zur hochpräzisen Anregung, Manipulation und Detektion von ^{87}Rb Rydberg-Atomen in einem ultrakalten Gas vollends aufgebaut und in Betrieb genommen.

In einem zwei Kammern umfassenden Vakuumaufbau wurde eine in einer magnetischen Falle gefangene ultrakalte Atomwolke hergestellt, entweder eine noch thermische Wolke oder ein Bose-Einstein Kondensat. Für die präzise Kontrolle des elektrischen Feldes am Ort der gefangen Atome und zur Ionendetektion wurde ein Experimentkäfig zusammengebaut und in die Vakuumkammer eingeführt. Dort umgibt er die gefangene Atomwolke.

In der gefangenen ultrakalten thermischen Atomwolke wurden mittels Zwei-Photonen-Anregung Rydberg-Atome im Zustand $40S_{1/2}$ angeregt. Durch ein starkes elektrisches Feld, erzeugt mit Hilfe des Experimentkäfigs, wurden die Rydberg-Atome ionisiert und die Rydberg-Ionen wurden mit einem der zwei an den Experimentkäfig angebrachten Ionendetektoren nachgewiesen. Die erfolgreiche Anregung und Detektion der Rydberg-Atome ermöglichte die Aufnahme eines Spektrums des ^{87}Rb $40S_{1/2}$ Zustandes. Weiterhin wurde der Einfluss eines elektrostatischen Feldes auf diesen Rydberg-Zustand untersucht und es wurde eine quadratische Verschiebung des Rydberg-Energieniveaus in Abhängigkeit des angelegten Feldes aufgrund des Stark-Effekts beobachtet.

Schließlich wurde ein Vorschlag zur Sichtbarmachung der Wellenfunktion eines Rydberg-Elektrons [Bal13] auf seine experimentelle Realisierbarkeit überprüft. Wie Simulationen zeigten wird unter geeigneten experimentellen Parametern bei aufeinanderfolgender Anregung von Rydberg-Atomen im Zentrum eines Bose-Einstein Kondensats die Wahrscheinlichkeitsdichteverteilung, d. h. das Quadrat der Wellenfunktion des Rydberg-Elektrons in die Atomdichteverteilung des Kondensats eingeprägt. Wie weitere Simulationen und Berechnungen zeigten, sollte es möglich sein mit Hilfe der Phasenkontrastabbildung ein Bild der Atomdichteverteilung des Kondensats aufzunehmen, auf dem die Struktur der eingeprägten Rydberg-Elektronen-Wellenfunktion deutlich erkennbar ist.

2. Introduction

Rydberg atoms are atoms with one or more electrons excited into a state of high principal quantum number n [Gal94].

They are named after Johannes Robert Rydberg who in the late 19th century found a formula, that now bears his name, which could describe the distribution of the spectral lines which at that time had been observed in the absorption spectra or the emission spectra of numerous different chemical elements [Whi34; MC05].

Rydberg atoms are atoms with exaggerated properties [Gal94]. The extreme properties of Rydberg atoms become clear if one considers the scaling of several atomic properties with the principal quantum number n (where n can only be used to describe the scalings for hydrogen; for alkali atoms the effective principal quantum number n^* has to be used instead, see [Gal94] and section 5.1). Since the binding energy scales with n^{-2} [Gal94] the Rydberg electron is very loosely bound. For example, the binding energy of the ^{87}Rb 40S Rydberg state (Rydberg state with $n = 40$ and orbital angular quantum number $l = 0$ of the rubidium (Rb) isotope with mass number 87) amounts to 10.0 meV [Mac11], whereas the 5S ground state of ^{87}Rb has a binding energy of 4.18 eV [Low12]. Additionally, Rydberg atoms are very large as the orbital radius scales with n^2 [Gal94]. The orbital radius of the ^{87}Rb 40S Rydberg state is approximately given by 108 nm and thus is 360 times bigger than the ^{87}Rb 5S ground state orbital radius of roughly 3 Å [RS85]. Moreover, Rydberg states are very long-lived since the lifetime scales with n^3 [Gal94]. The lifetime of the ^{87}Rb 40S Rydberg state is approximately 36 µs [Bet09], whereas the lifetime of the low lying ^{87}Rb $5P_{3/2}$ state ($j = 3/2$ is the total angular quantum number) amounts to roughly 26 ns [Ste10].

The interaction between Rydberg atoms is very strong due to their large polarizability resulting from their large orbital radii: the C_6 coefficient describing the van der Waals interaction between the Rydberg atoms scales with n^{11} [SWM10]. For Rydberg experiments with ultracold atomic gases, first done in the late 1990's [AVG98; Mou98], the interaction-induced energy shifts, which are much larger than the thermal energy of the atoms, block the excitation of multiple Rydberg atoms within a confined volume, an effect referred to as the Rydberg blockade [Luk01; Ton04; Sin04]. The N atoms inside the Rydberg blockade volume are often denoted as a "superatom" with a collective ground state and a collective excited state, where any, but only one, atom can be excited into the Rydberg state [SC09]. For Rabi oscillations between this collective ground and excited state of the "superatom", the collective Rabi frequency is expected to be faster by a factor of $\sqrt{N}$ compared to the isolated-atom Rabi frequency [SC09]. The enhanced collective Rabi frequency was experimentally observed first for an ensemble of "superatoms" [Hei07], and later also for a single "superatom" which comprised either only $N = 2$ atoms [Gae09] or several hundred individual atoms [Dud12].

The idea of a quantum computer, i. e. a computational device based on quantum physics, was brought forward in the 1980's by, among others, Richard Feynman [Fey82] and David Deutsch [Deu85] in the context of quantum simulation, as it was recognized that a universal quantum computer could perfectly simulate any finitely realizable quantum system [Deu85]. When in the 1990's Peter Shor devised an algorithm for rapidly

factorizing integers on a quantum computer, encryption turned out to be another possible field of application for quantum computers [Sho95]. Since then, quantum bits (qubits) and quantum gates have been implemented in several quantum systems, including trapped ions [BW08], NV color centers in diamond [Doh13], quantum dots in semiconductors [KL13], and superconductors [CW08]. The implementation of neutral atom quantum gates taking advantage of the mentioned strong interaction between Rydberg atoms was proposed in the early 2000's [Jak00; Luk01]. The first experimental demonstration of a controlled-NOT quantum gate between two neutral atoms using the Rydberg blockade was done in 2010 [Ise10]. The entanglement generation between a pair of neutral atoms utilizing the Rydberg blockade was first experimentally demonstrated in 2010 as well [Wil10]. The use of Rydberg quantum gates for the quantum simulation of spin models involving n-body interactions was proposed in [Wei10], however, this Rydberg quantum simulator has not yet been experimentally realized. An overview of the use of Rydberg atoms for quantum computation is given in [SWM10].

The Rydberg blockade can also be exploited in the field of quantum communication for example to realize a single photon source [DK12], a single photon absorber [Hon11], or quantum repeaters [Han10; Zha10].

Most recently, the coupling of a single Rydberg electron to a Bose-Einstein condensate (BEC) was demonstrated [Bal13]. Due to the large radius of the Rydberg electron orbital, up to 30 000 ground state condensate atoms were located inside the electron orbital and thus interacted with the electron impurity, which resulted in a measurable coupling-induced loss of condensate atoms.

About this thesis In this master thesis the highly precise excitation, manipulation and detection of ^{87}Rb Rydberg atoms in an ultracold gas is described.

The production of either a trapped ultracold, but thermal cloud of ^{87}Rb atoms, or a trapped Bose-Einstein condensate of ^{87}Rb atoms in a two-chamber vacuum setup is described in chapter 3.

The assembly and insertion into the vacuum chamber of the experiment cage, an indispensable part of the setup for the manipulation and detection of Rydberg atoms, is described in chapter 4.

Chapter 5 forms the main part of this thesis. First, the two-photon excitation of ^{87}Rb S-state Rydberg atoms is discussed in section 5.1. The electric field ionization of the Rydberg atoms and the detection of the Rydberg ions is described in section 5.2. Recorded spectra of the ^{87}Rb $40S_{1/2}$ Rydberg state are presented and discussed in section 5.3. Finally, the effect of a dc electric field on the ^{87}Rb $40S_{1/2}$ Rydberg state is investigated in section 5.4 and a Stark map of this Rydberg state is presented.

The mentioned observation of the coupling between a single Rydberg electron and a BEC [Bal13] has initiated the idea to image the Rydberg electron wavefunction, more precisely the square of it, via its imprint onto the in-trap density distribution of the BEC. In chapter 6, simulations are presented which suggest that the experimental realization of this idea is feasible. First, simulations of the in-trap BEC density distribution after several consecutive Rydberg excitations at the center of the BEC into either the 110S-

state or the 160D-state are shown. Afterwards, the in-trap detection of the imprint of the Rydberg electron wavefunction onto the BEC density distribution via the phase contrast imaging technique is discussed.

3. The two-chamber setup for an ultracold gas

Exciting Rydberg atoms in an ultracold trapped gas facilitates precision spectroscopy of the Rydberg state [Low12]. Due to the low temperature of the atomic sample, the Doppler effect is very small (see section 5.1.3). Besides, the collision rate between the ultracold atoms is almost negligible. Therefore the time for coherent coupling between the atoms and the excitation light (see section 5.1) is not limited by collisions but by the finite lifetime of the Rydberg state (see section 5.1.2). The low temperature also allows for the reliable preparation of a specific quantum state since the thermal redistribution of the population from the target state into other states is not significant.

In this chapter the preparation procedure used in the scope of this thesis for the production of an ultracold atomic sample is presented. The underlying cooling and trapping techniques are not described in detail, however, references are given where a detailed discussion of these techniques can be found.

The production of an ultracold trapped atomic sample has necessarily to be done in a vacuum chamber. Under normal pressure, the very frequent collisions with the background gas would, firstly, heat up the atomic sample considerably, and secondly would kick the atoms out of the trap. We use a two-chamber vacuum setup as is depicted in figure 3.1. The element we use is the alkali metal rubidium (Rb), more specifically we utilize the stable isotope ^{87}Rb which has a relative natural abundance of approximately 28 % [Ste10]. There is a second stable isotope of rubidium, ^{85}Rb, which has a relative natural abundance of 72 % [Ste13]. However, the production of ^{85}Rb Bose-Einstein condensates with atom numbers roughly comparable with those of ^{87}Rb condensates (see section 3.3) is only possible by using a Feshbach resonance [Cor00]. In the MOT chamber (see figure 3.1; MOT: magneto-optical trap) the ^{87}Rb atoms are captured and pre-cooled (see section 3.1). Then, the atoms are magnetically transported over a distance of roughly 45 cm through a narrow tube (see section 3.2) into the second chamber, the experiment chamber. In the experiment chamber, a glass cell, the atoms are held in a QUIC-trap (quadrupole-Ioffe-configuration-trap) and evaporatively cooled down either to a very cold thermal gas or to a quantum degenerate gas, a Bose-Einstein condensate (see section 3.3). Having prepared the ultracold atomic sample, the Rydberg experiments can be done in the glass cell which is why the glass cell is referred to as the experiment chamber.

The long and narrow tube which connects the MOT chamber with the experiment chamber allows for differential pumping [The05], i. e. there can be a permanent pressure difference between the MOT and the experiment chamber. With the vacuum pumps we use, a pressure difference of roughly two orders of magnitude can be achieved with a pressure p_{MOT} of usually around 8×10^{-9} mbar in the MOT chamber and a pressure $p_{\mathrm{exp}} \approx 2 \times 10^{-11}$ mbar in the experiment chamber. Therefore, with the higher pressure in the MOT chamber the collection of ^{87}Rb atoms from the background vapor pressure is fast which provides the possibility of short experiment cycles and thus high repetition rates. On the other hand, the low pressure in the experiment chamber allows for a long lifetime of the trapped ultracold atomic sample as there are only few collisions with the background gas. Hence, the time per experiment cycle in which the Rydberg experiments can be carried out is long.

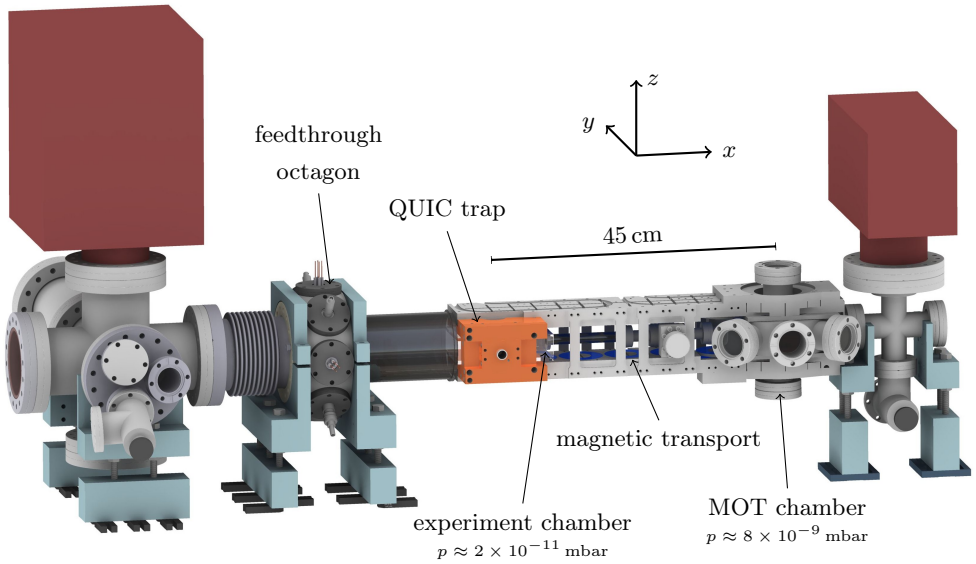

Figure 3.1: Engineering drawing of the two-chamber vacuum setup.

3.1. The MOT chamber

Figure 3.2a displays an engineering drawing of the steel MOT chamber. A rubidium reservoir, a glass tube containing 5 g of elemental Rb, is mounted to this chamber. The Rb background pressure in the MOT chamber can be regulated with a valve between the Rb reservoir and the chamber.

A magneto-optical trap (MOT) is loaded from the background Rb pressure. A detailed description of the working principle of a MOT can be found in [MS99]. In the following only the basic principles of the MOT will be outlined. The first constituent of the magneto-optic trap is a magnetic quadrupole field inside the MOT chamber, produced by one coil on top and one coil below the steel chamber (see figure 3.2a), operated in anti-Helmholtz configuration. The second component of the MOT are three orthogonal pairs of counter-propagating laser beams with diameter of two inches which cross one another at the center of the MOT chamber (see figure 3.2a). In the intersection region the atoms get decelerated in all three spatial directions by these laser beams. The slowing radiative force is based on the repeated scattering of photons with momentum $\hbar k$ by the atoms. One scattering process, i. e. the process of absorption of a photon and subsequent spontaneous emission of a photon, effectively reduces the atoms' momentum by the amount $\hbar k$. The reason for this is that the spontaneous emission occurs in a random spatial direction which results in an average of zero net momentum transfer on the atom due to the spontaneous emission. To allow for repeated photon scattering, the cooling laser has to drive a cycling transition in the atoms to be slowed down. In the scope of this thesis, the cycling transition from $5S_{1/2}$, $F = 2$ to $5P_{3/2}$, $F' = 3$ was used

to cool the ^{87}Rb atoms (see figure 3.2b). A diode laser seeding a tapered amplifier[1] with maximum output power of 1.5 W was set to a wavelength $\lambda = 780.246\,\text{nm}$ [Ste10] to drive this transition. This laser is referred to as the MOT cooler. Due to off-resonant excitation of the $5P_{3/2}$, $F' = 2$ state a slight amount of population is lost to the $5S_{1/2}$, $F = 1$ level via spontaneous decay into this level. In order to transfer this population back to the cooling cycle, a second laser[2], the MOT repumper, is used. It drives the transition from $5S_{1/2}$, $F = 1$ to $5P_{3/2}$, $F' = 2$ (see figure 3.2b), operating at a wavelength $\lambda = 780.233\,\text{nm}$ [Ste10].

The six laser beams cool the atoms, but they do not trap them [MS99]. However, by adding the mentioned magnetic field and red detuning the cooler light as well as choosing appropriate polarizations for the six laser beams [MS99], a force pointing towards the center of the quadrupole field, where the magnetic field is zero, is produced, i. e. a trapping force is generated.

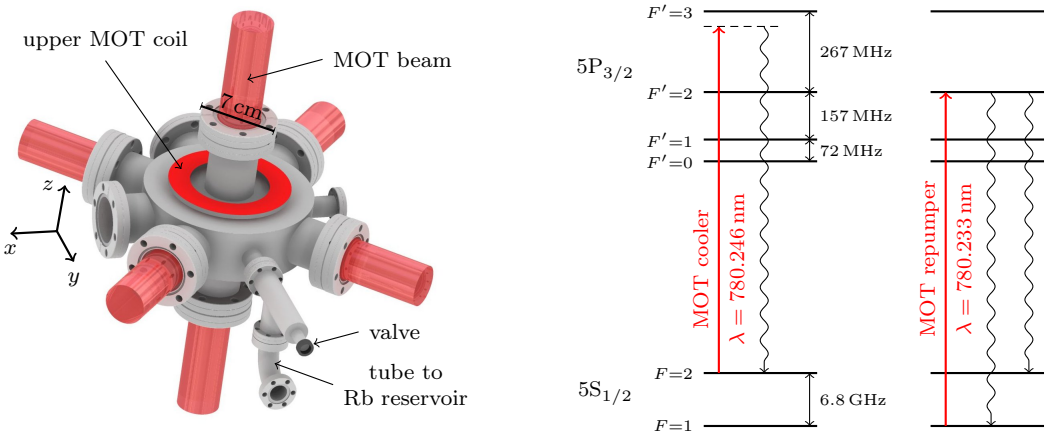

(a) Drawing of the MOT chamber.

(b) Used cooling and repumping transitions.

Figure 3.2: Engineering drawing of the MOT chamber in (a). The upper MOT coil and the MOT laser beams are also displayed. Subfigure (b) shows a part of the ^{87}Rb level scheme to illustrate the cycling transition of the MOT cooler and the effect of the MOT repumper. The plotted frequency splittings between the hyperfine levels are taken from [Ste10].

The loading of the MOT from the Rb background pressure usually takes 6 s (see figure 3.4). After this loading time typically a few billion atoms are trapped, having a temperature of around 200 µK. Figure 3.3a displays a fluorescence picture of the ^{87}Rb MOT in the MOT chamber.

After loading the MOT, the optical molasses cooling technique [MS99] is applied for a short period of time, typically a few milliseconds (see figure 3.4). For this purpose, the magnetic quadrupole field of the MOT is switched off while the MOT lasers re-

[1] Toptica TA pro series
[2] Toptica DL pro series

main switched on, slightly more red detuned than in the MOT phase for optimal cooling [MS99]. Without the magnetic trapping potential heating the atoms, their temperature can be further reduced down to 50 µK in the optical molasses.

Subsequent to the optical molasses, the cold ^{87}Rb atomic sample is spin-polarized in the low-field seeking $5S_{1/2}$, $F = 2$, $m_F = +2$ state (see section 3.2) via optical pumping. During the optical pumping, a homogeneous magnetic field is applied to split up the hyperfine levels into their Zeeman sublevels (see figure 3.3b), and to determine the axis of quantization. The MOT cooler laser is tuned to be resonant to the $5S_{1/2}$, $F = 2 \rightarrow 5P_{3/2}$, $F' = 2$ transition and its polarization is set to σ^+. Thus, the population is transferred into the desired $F = 2$, $m_F = +2$ dark state within a few absorption-emission cycles, as is illustrated in figure 3.3b. Concurrent with the σ^+ spin polarizer laser, the MOT repumper laser is shone in to pump atoms from the $F = 1$ ground state back the $F = 2$ state. The optical pumping typically takes 3 ms (see figure 3.4).

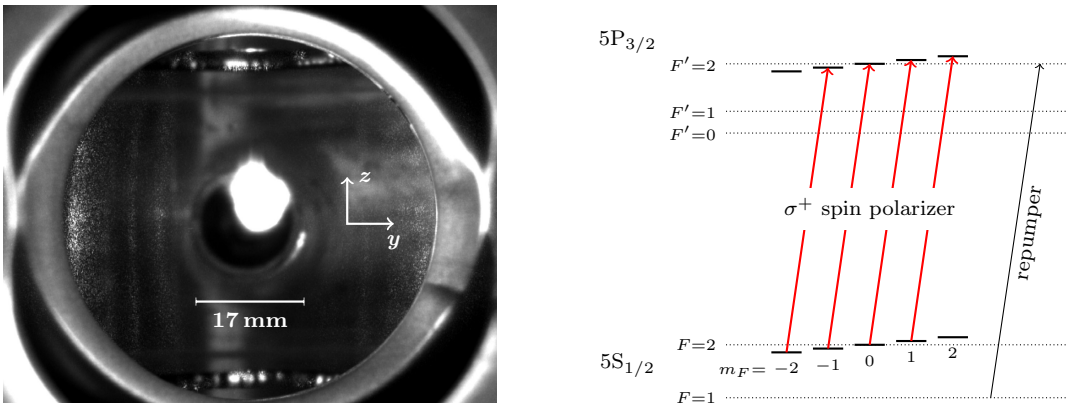

(a) Fluorescence image of the MOT.

(b) Optical pumping scheme for ^{87}Rb.

Figure 3.3: A fluorescence image of the MOT is depicted in (a). The scheme to prepare the ^{87}Rb atoms in the $5S_{1/2}$, $F = 2$, $m_F = +2$ dark state via optical pumping with a σ^+-polarized laser is illustrated in (b).

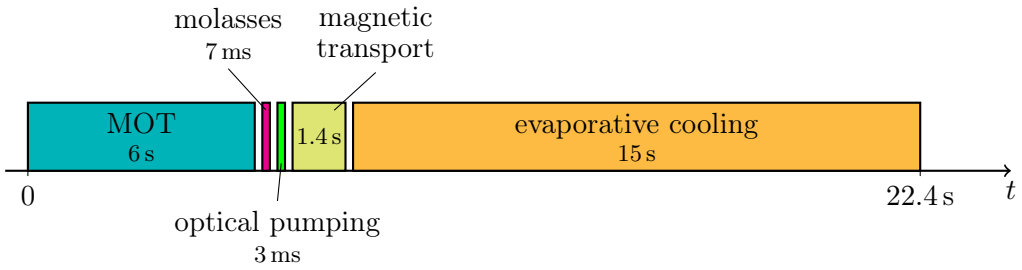

Figure 3.4: Schematic illustration of the experimental sequence used in this thesis for the production of an ultracold atom cloud.

3.2. The magnetic transport

The Zeeman effect [Sch07] can be utilized to confine neutral atoms in a magnetic trap. For an atom exposed to a magnetic field B the energy of a magnetic sublevel $|F, m_F\rangle$ is shifted by the amount $\Delta E_{|F,m_F\rangle} = \mu_\mathrm{B} g_F m_F B$ compared to the case of zero magnetic field, where μ_B is the Bohr magneton and g_F is the Landé g-factor [Ste10]. Therefore, an extremum of the magnetic field B results in a trapping potential for atoms prepared in a magnetic substate $|F, m_F\rangle$ with suitable m_F and g_F. In free space, the magnetic field can only have minima but no maxima [Win84]. Thus, only low-field seeking states can be magnetically trapped, i. e. states for which the energy decreases with decreasing magnetic field, hence states with $g_F m_F > 0$. The state the ^{87}Rb atoms are optically pumped to, the $5\mathrm{S}_{1/2}$, $F = 2$, $m_F = 2$ state (see section 3.1), is such a low-field seeking state as the Landé-factor $g_F = 1/2$ for the $F = 2$ states [Ste10]. Thus, after the optical pumping the spin-polarized Rb atoms are transferred to a magnetic trap in the MOT chamber where the magnetic field minimum is realized by operating the two MOT coils in anti-Helmholtz configuration.

To transport the atom cloud from the MOT chamber to the experiment chamber, the magnetic trapping potential is then moved from the first to the second chamber. The trapping magnetic field minimum has to be shifted sufficiently slowly that the trapped atoms can follow the position shift of the trap center adiabatically. To achieve the required position change of the trapping potential, twelve pairs of coils in anti-Helmholtz configuration are mounted below and above the narrow tube which connects the MOT chamber with the glass cell, as can be seen in figure 3.5. An elaborate current sequence is applied to the overlapping transport coils in order to avoid heating of the atomic sample during the magnetic transport as much as possible [Gre01; The05]. The magnetic transport sequence used in the scope of this work is 1.4 s long (see figure 3.4). Starting with a typical atom number of 4×10^9 in the MOT, approximately 2×10^9 atoms arrive in the glass cell, where most of the atoms get lost at the transfer from the MOT to the magnetic trap in the MOT chamber and not during the actual magnetic transport. The temperature of the atomic cloud after the transport is usually around 400 µK.

3.3. The experiment chamber

As mentioned above, the experiment chamber is a glass cell[3] (see also figure 3.5 and figure 3.6). This allows for good optical access to image the ultracold atomic sample (see below), and to excite Rydberg atoms in the atomic cloud (see section 5.1). Additionally, as the glass cell is more compact than a standard steel vacuum chamber, the coils used to magnetically trap the cold atoms inside the glass cell (see figure 3.6) can be mounted closer to the atoms. Therefore less current is required to trap the atoms, thus less heat is dissipated by the coils.

A trap configuration referred to as the QUIC-trap is used in the scope of this work to trap the atoms in the glass cell (see figure 3.6). The first component of the QUIC-trap is a quadrupole trap, realized by one coil above and a second coil below the glass

[3] Custom made by the Japan Cell company

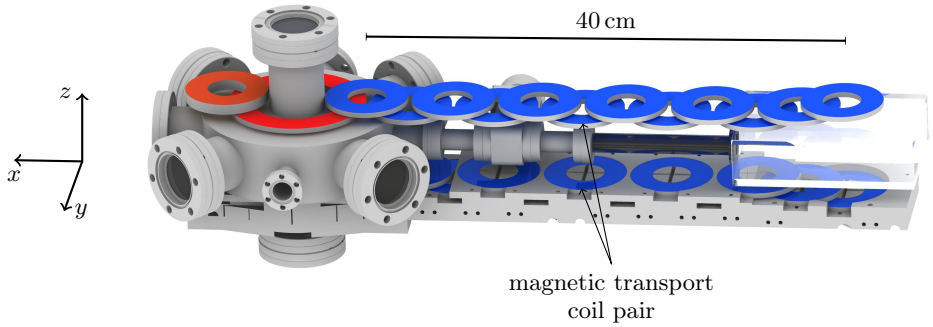

Figure 3.5: Engineering drawing of the magnetic transport line from the MOT chamber (left) to the glass cell (right). The magnetic transport coils are mounted in an aluminium rack (displayed only for the coils below the connection tube) to lead away the dissipated heat.

cell operated in anti-Helmholtz configuration. The quadrupole trap generates a linear trapping potential which is zero at the trap center. However, a finite trap bottom is required in order to prevent the ultracold atoms from escaping the trap by making spin-flip Majorana transitions [BS06]. This finite trap bottom is provided by the second component of the QUIC-trap, the Ioffe coil. It converts the linear trap into an approximately harmonic trap near the trap center with a finite offset field which is approximately 1 G for our setup. The Bose-Einstein condensation of ^{87}Rb atoms in a QUIC-trap was first demonstrated in [EBH98].

We measured the trap frequencies of the QUIC-trip to be $\omega_x = \omega_z = 2\pi \times 214\,\mathrm{Hz}$ in the x- and in the z-direction, respectively, and $\omega_y = 2\pi \times 15\,\mathrm{Hz}$ in the y-direction (see figure 3.6). The used QUIC-trap is therefore a radially symmetric elongated trap, i. e. a cigar-shaped trap, with a tight confinement in the x- and z-axis and a loose confinement in the y-axis. A lifetime measurement for the cold atomic sample in the QUIC-trap yielded a lifetime of approximately 25 s, i. e. after 25 s the number of trapped atoms is reduced to $1/e \approx 37\,\%$ of its initial value.

As mentioned in section 3.2 the QUIC-trap is loaded from the magnetic transport with typically a few billion atoms having a temperature of around 400 µK. The evaporative cooling technique [KD96] is then used to further reduce the atoms' temperature. Evaporative cooling of trapped atoms is based on the removal of "hot" atoms, i. e. atoms traveling with a large velocity, from the trap whereby, after rethermalization, the temperature of the remaining atoms is reduced. We use radio frequency (rf) radiation to transfer the hot ^{87}Rb atoms from the trapped low-field seeking $5S_{1/2}$, $|F{=}2, m_F{=}+2\rangle$ state into the high-field seeking untrapped states $|F{=}2, m_F{=}-1\rangle$ and $|F{=}2, m_F{=}-2\rangle$

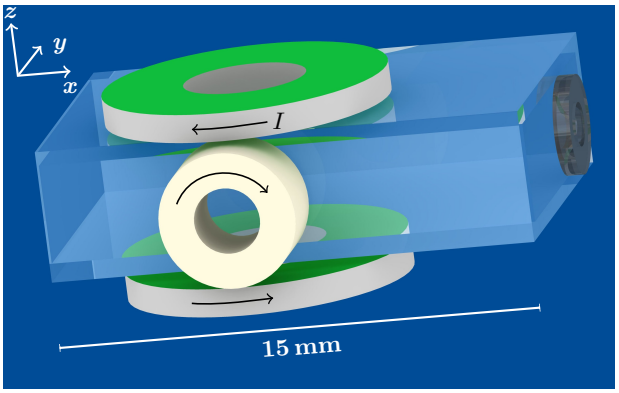

Figure 3.6: Engineering drawing of the QUIC-trap surrounding the glass cell. The QUIC-trap consists of two coils (top and bottom) operated in anti-Helmholtz configuration and thus producing a quadrupole field, and a Ioffe coil (front) which adds a finite offset field to the linear quadrupole trap at the trap center. The direction the current I runs through the respective coils in order to produce the desired trapping potential is also plotted.

(see section 3.2). Starting with a high rf frequency, only atoms in a shell at the edge of the trapped cloud are resonant to the applied rf radiation since the Zeeman energy splitting between the m_F-sublevels is biggest at the edge where the magnetic field is the strongest. Since the fast atoms move at the fringes of the atomic cloud where the trapping potential is the largest, the high rf frequency removes these fast atoms from the trap. Therefore, by ramping down the rf frequency, increasingly slower atoms are removed from the trap and the remaining atomic cloud gets colder and denser. The end frequency of the rf ramp determines the end temperature of the atomic sample, given that this end frequency relates to an energy still larger than the Zeeman splitting of roughly $h \times 0.7\,\mathrm{MHz}$ between the $|F{=}2, m_F{=}2\rangle$ and the $|F{=}2, m_F{=}1\rangle$ state at the trap center. In the scope of this thesis the rf frequency was ramped down from 40 MHz to a few MHz to get an ultracold but still thermal gas, and to a little bit less than 1 MHz to cool the atoms below the phase transition of Bose-Einstein condensation (see below). The whole rf ramp usually took around 15 s (see figure 3.4). The rf radiation was applied to the atoms via a small coil close to the atoms (see section 4.1).

For the Rydberg spectroscopy experiments done in the frame of this work (see chapter 5) an ultracold, yet still thermal atomic sample was used. The temperature T of the cloud typically was in the range from 1 µK to 15 µK. The total number of atoms N in the sample usually was a few millions. Temperature and atom number of the atomic sample were determined via absorption imaging [KDS99] after the cloud was allowed to expand freely for a few milliseconds. For the absorption imaging a diode laser[4] was operated close to resonance of the $^{87}\mathrm{Rb}$ $5\mathrm{S}_{1/2}$, $F = 2 \rightarrow 5\mathrm{P}_{3/2}$, $F' = 3$ transition with a wavelength $\lambda = 780.246\,\mathrm{nm}$ [Ste10] (see figure 3.2b). From the temperature of the cloud and the trap

[4] Toptica DL pro series

frequencies, the in-trap size of the thermal cloud can be calculated with $R_i = \sqrt{\frac{2k_\mathrm{B}T}{m\omega_i^2}}$, $i = x, y, z$, where R is the distance from the trap center where the cloud's density is only $1/e$ of its peak value at the center; k_B is the Boltzmann constant and m the mass of the trapped atoms [PS08]. Inserting the respective values yields $R_x = R_z = 23\,\mu\mathrm{m}$ and $R_y = 328\,\mu\mathrm{m}$ for a temperature $T = 5\,\mu\mathrm{K}$. The in-trap peak density of the thermal cloud is given by $n(\mathbf{r} = 0) = \frac{N}{\pi^{3/2} R_x R_y R_z}$ [PS08], which yields approximately $4.1 \times 10^{12}\,\mathrm{cm}^{-3}$ for a typical atom number $N = 4 \times 10^6$ at $T = 5\,\mu\mathrm{K}$. Since the momentum distribution of the trapped thermal gas is isotropic [PS08], after a time of flight t long enough ($t \gg \frac{1}{\overline{\omega}}$, $\overline{\omega} \equiv (\omega_x \omega_y \omega_z)^{1/3}$) the anisotropic in-trap thermal cloud gets spherically symmetric with a $1/e$-width $\sigma(t) = \sqrt{\frac{2k_\mathrm{B}T}{m}} \cdot t$ in all three spatial directions [PS08].

The capability of the used setup for the production of a ^{87}Rb Bose-Einstein condensate (BEC) was also demonstrated. Figure 3.7a displays an absorption picture of a generated BEC after a time of flight of 30 ms. The absorption picture was taken with a horizontal imaging beam propagating along the y-axis (see figure 3.6). The temperature T of the cloud was determined to be around 100 nK and the atom number N was roughly 1×10^5. In figure 3.7b the optical density summed over the z-axis is plotted as a function of x. In this plot the condensate fraction of the cloud (the narrow peak in the middle) can be distinguished from the thermal component (the broad background on the edges). This is due to the fact that the momentum distribution of the BEC is much narrower than that of the thermal gas [PS08]. Therefore, after some time of flight the BEC emerges as a narrow peak in the broad background of the thermal gas. The full width at half maximum (FWHM) of the thermal component along the x-axis was determined to be approximately 260 µm (see Gaussian fit in figure 3.7b). After subtracting the thermal component in figure 3.7b the Thomas-Fermi radius of the BEC (see below) along the x-axis was determined to be approximately 60 µm. The BEC fraction of the ultracold cloud displayed in figure 3.7a was extracted to be roughly 26 %.

The in-trap size of the condensate can be estimated using the Thomas-Fermi approximation which holds for sufficiently large clouds [PS08]. Within this approximation the Thomas-Fermi radius R^TF denotes the distance from the trap center where the atomic density vanishes. For a harmonic trap with trap frequencies ω_i, $i = x, y, z$, the three Thomas-Fermi radii along the coordinate axes are given by

$$R_i^\mathrm{TF} = \sqrt{\frac{2\mu}{m\omega_i^2}}, \tag{3.1}$$

where μ is the chemical potential and m the mass of the trapped atoms [PS08]. The chemical potential can be calculated from the atom number N with

$$\mu = \frac{15^{2/5}}{2} \left(\frac{Na}{\overline{a}}\right)^{2/5} \hbar\overline{\omega}, \tag{3.2}$$

where a is the scattering length, and $\overline{a} = \sqrt{\frac{\hbar}{m\overline{\omega}}}$ the characteristic length for a harmonic oscillator of frequency $\overline{\omega} = (\omega_x \omega_y \omega_z)^{1/3}$ [PS08]. The scattering length a for the

^{87}Rb $5S_{1/2}$, $F = 2$, $m_F = 2$ state is $(103 \pm 5)a_0 = (5.45 \pm 0.26)\,\mathrm{nm}$ according to reference [Jul97], where a_0 denotes the Bohr radius. Thus, the Thomas-Fermi radii for the ^{87}Rb BEC in the QUIC-trap we used, for which the trap frequencies are cited above, amount to $R_x^{\mathrm{TF}} = R_z^{\mathrm{TF}} = 2.8\,\mu\mathrm{m}$ and $R_y^{\mathrm{TF}} = 40\,\mu\mathrm{m}$.

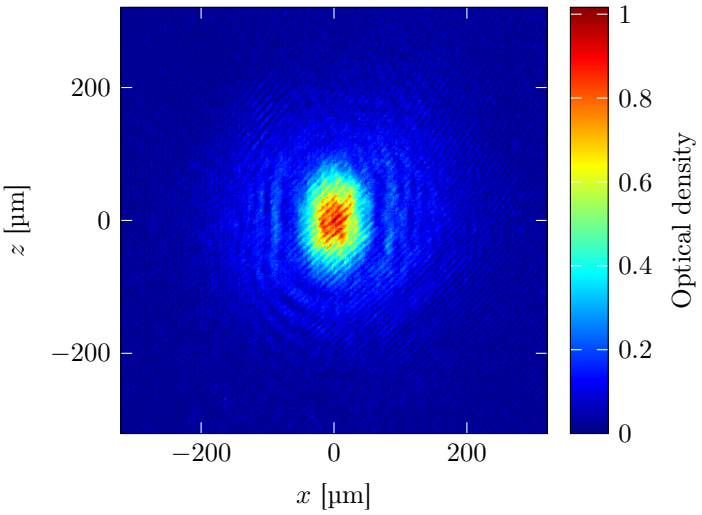

(a) Absorption picture of the BEC.

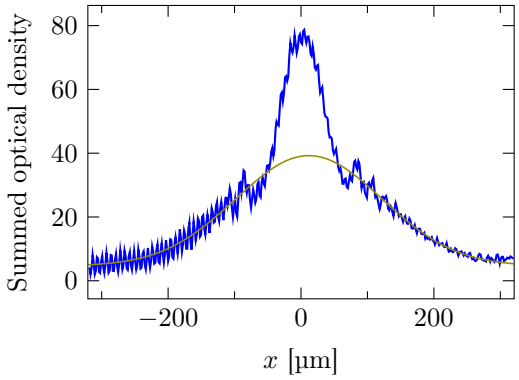

(b) Summed optical density as a function of x.

Figure 3.7: In (a), an absorption image of a ^{87}Rb BEC, that was produced with the setup described in this chapter, is displayed. It was taken after 30 ms time of flight with the imaging beam along the y-axis (see figure 3.6). The temperature of the depicted atomic sample is roughly 100 nK and the cloud contains approximately 1×10^5 atoms. In (b), the optical density summed over the z-axis is plotted as a function of x (blue line). The condensate appears as a narrow peak in the middle over the broad background of the thermal gas. Fitting a Gaussian function to thermal component (olive-green line) yielded a FWHM of roughly 260 µm. After subtracting the thermal component the Thomas-Fermi radius of the BEC along the x-axis was determined to be approximately 60 µm. The BEC fraction was extracted to be roughly 26 %. The ring pattern surrounding the condensate peak is due to the BEC acting as a gradient-index lens [Jen12].

4. The experiment cage

4.1. Introduction

The experiment cage is a small cuboid cage inside the glass cell (see section 3.3) at the center of which the atom cloud is held by the QUIC trap and Rydberg experiments are done. High precision Rydberg experiments need to be done inside a metal cage as Rydberg atoms are very susceptible to electric fields (see section 5.4) and the metal cage screens undesired electric stray fields (Faraday cage [Sch11]). Such electric stray fields may, for example, be caused by surface charges on dielectric surfaces, as e. g. the glass cell walls. Since the experiment cage is placed within a magnetic trap and in ultrahigh vacuum (UHV), the metal titanium (Ti) was chosen for the cage, as it is non-magnetizable [Lid10] and has an outgassing rate comparable or even smaller than stainless steel [MI95], the standard material for UHV applications.

However, the experiment cage does not only screen electric stray fields, the six Ti plates the cage consists of are also six separately addressable electrodes. Macor spacers are used in between the Ti plates to insulate them from each other. Macor is perfectly suited for this purpose as it has a very high dielectric strength (129 kV/mm for DC voltage applied [Cor12]), is compatible with UHV [Cor12], plus it is non-magnetizable [Dav93]. The six separately addressable electrodes allow for the generation of very homogeneous electric fields inside the cage [Tre12], which are for example required to take a high resolution Stark map of a Rydberg state (see section 5.4). One electrode can also be used to produce a strong ionization field, with which the state selective ionization of Rydberg atoms is possible [Tre12].

To provide access to the inside of the experiment cage, e. g. to get the atom cloud in and allow optical access, each of the six Ti sides of the cage has an aperture.

Two ion detectors are added to the experiment cage on two opposing sides. After ionizing the Rydberg atoms at the center of the cage, the Rydberg ions fly to one of the two ion detectors, depending on the direction of the ionization field, leaving the cage through the aperture in front of the respective ion detector. Both ion detectors are electron multiplier tube detectors (see section 5.2). One of them is a microchannel plate (MCP) detector, where many microchannels are arranged in a plate, parallel and close to one another. The other ion detector is a channeltron, comprising only six electron multiplier tubes.

In the top and bottom plate of the experiment cage, aspheric lenses with a high numerical aperture $NA = 0.55$ at the design wavelength $\lambda = 780\,\text{nm}$ are mounted [asp13]. Thereby, a high optical resolution $d_{\text{min}} = \frac{\lambda}{2NA} = 0.7\,\mu\text{m}$ (Abbe diffraction limit [LLL11]) is achieved at the center of the experiment cage for a laser beam with $\lambda = 780\,\text{nm}$ traveling along the vertical axis. The aspheric lenses are also anti-reflexion coated at the four wavelengths 420 nm, 480 nm, 780 nm and 1020 nm.

Several thin Ti wires span each of the six apertures of the experiment cage. They ensure by closing the Faraday cage that electric fields, e. g. caused by surface charges on the aspheric lenses, do not enter the inside of the cage through the apertures. In addition, these wires improve the homogeneity of the electric field which is produced inside the

cage by applying a voltage to two opposing Ti plates [Tre12].

A small coil is mounted around the channeltron. This coil, placed close to the atom cloud at the center of the experiment cage, is used to emit radio frequency (rf) radiation for the evaporative cooling of the trapped atoms (see section 3.3).

Figure 4.1 depicts the experiment cage where the elements of the cage, that were described above, are labeled.

The experiment cage was very well designed by Christoph Tresp during his master thesis [Tre12].

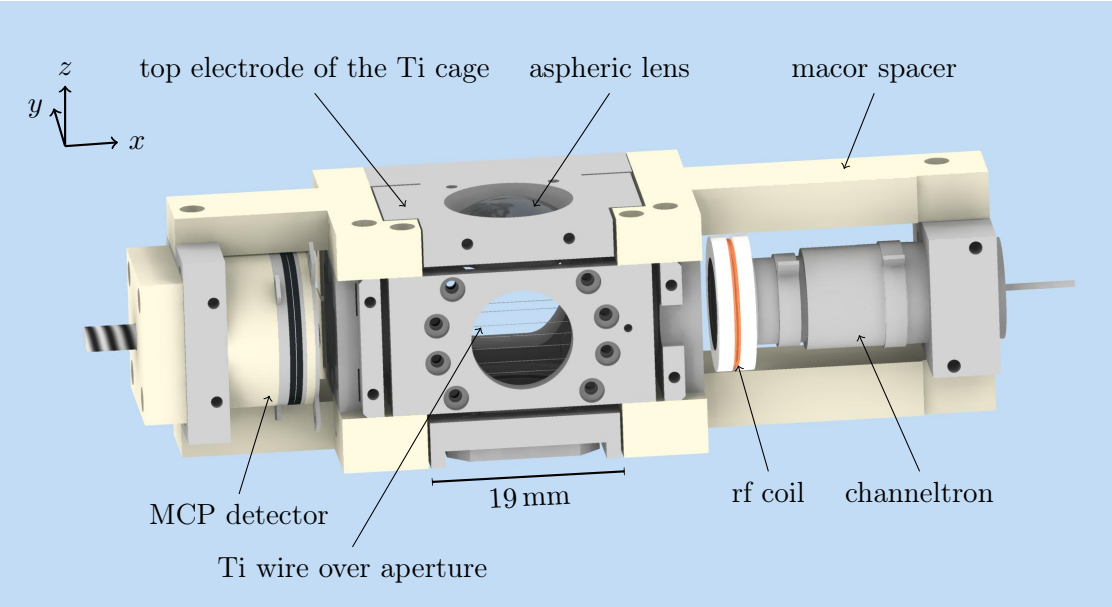

Figure 4.1: Display of the experiment cage with labeled functional elements, scale and coordinate axes.

4.2. Preventing current breakthroughs in the experiment cage

As mentioned in section 4.1, the six Ti sides of the experiment cage are separately addressable electrodes. They are separated either by macor or by air (see figure 4.2) and the minimum spacing d between adjacent sides is roughly 1 mm. The voltage difference between neighboring sides can be as high as a few kilovolts (kV). For example, you have to apply approximately a voltage U_{ion} of 1 kV to ionize a Rb $n = 30$ Rydberg atom that is located at the center of the experiment cage [Tre12]. Hence, the question arises if the maximum voltage difference of a few kV between adjacent Ti electrodes is already larger than the breakthrough voltage U_{b}, which would result in current breakthroughs.

Since the dielectric strength of macor is 129 kV/mm for DC voltages [Cor12], there will not be any current breakthroughs through the macor spacers.

The breakthrough voltage U_b of air can be calculated using Paschen's law [Wad07]

$$U_\mathrm{b}(pd) = \frac{B \cdot pd}{\ln\left(\frac{A}{K} \cdot pd\right)}, \tag{4.1}$$

where p is the pressure of the air which fills the space between two infinitely large parallel electric field plates, separated by the distance d. $K = \ln(1 + \frac{1}{\nu})$, and ν, A as well as B are constants specific for the gas between the parallel electric field plates. For air, typical values of these constants are $A = 1.2\,\mathrm{mbar}^{-1}\,\mathrm{mm}^{-1}$, $B = 36.5\,\mathrm{V}\,\mathrm{mbar}^{-1}\,\mathrm{mm}^{-1}$ and $\nu = 0.02$ [Wad07], thereby $K = 3.93$. Using these constants, figure 4.3 depicts the breakthrough voltage U_b of air as a function of the air's pressure p and the electric field plate spacing d. As can be seen from this graph, the breakthrough voltage strongly increases for pd values smaller than about 8 mbar mm and already for $pd \approx 3.8$ mbar mm the breakthrough voltage is 1 kV. Since the experiment cage stands inside the glass cell, the pressure of the air between adjacent Ti sides is approximately 2×10^{-11} mbar (see chapter 3). With the spacing $d \approx 1$ mm between neighboring sides (see figure 4.2), the product pd takes values as small as 2×10^{-11} mbar mm, for which the breakthrough voltage U_b is much greater than the voltage of at most a few kV, that will be applied to the Ti electrodes.

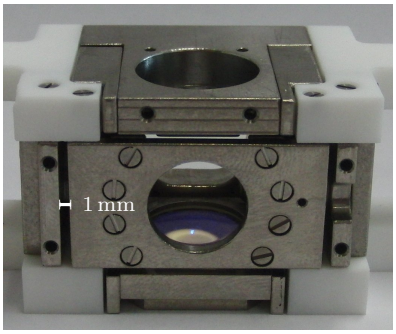

Figure 4.2: Detailed view of the experiment cage to illustrate the spacing d between adjacent Ti sides.

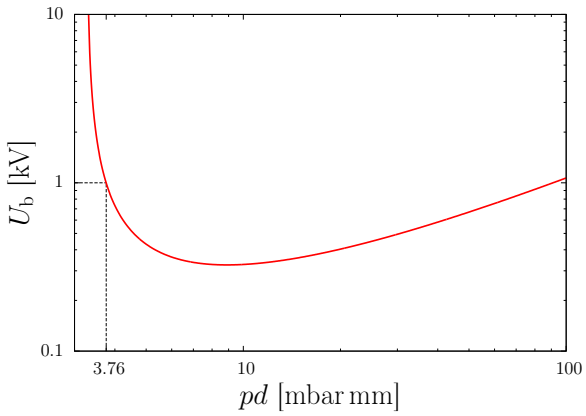

Figure 4.3: The breakthrough voltage U_b of air as a function of the air's pressure p and the electric field plate spacing d, calculated using Paschen's law (equation 4.1) and the material constants specific for air taken from [Wad07]. Assuming a spacing $d = 1$ mm, then U_b is as large as 1 kV already for the rather high pressure p of 3.76 mbar. For pressures smaller than that, U_b increases strongly.

However, the breakthrough voltage calculated with Paschen's law is only valid under the assumption of two infinitely large, perfectly flat, parallel electric field plates with a

homogeneous electric field in between them. As is clear from figure 4.2, this assumption does not hold for the experiment cage. The areas of adjacent Ti plates which face each other are finite. Besides, the surface of the Ti plates will not be perfectly flat and smooth, but it is a little bit rough and uneven, with e. g. tiny scratches and bumps on it. Thus, the electric field between adjacent Ti plates will not be homogeneous, probably there will be local electric field spikes. As a result of these electric field spikes, the actual breakthrough voltage may be much smaller than that calculated with Paschen's law and illustrated in figure 4.3.

4.2.1. Electropolishing of the Ti plates

To prevent current breakthroughs caused by surface roughness of the Ti plates, two measures were undertaken.

First, the Ti plates were handpolished by Gabriele Untereiner from the 1st physical institute of the university of Stuttgart. However, the edges and holes of the Ti plates are not accessible to handpolishing, only the large areas are.

To smoothen the edges, electrolytic polishing, or electropolishing, was chosen. As the name suggests, electrolytic polishing is based upon electrolysis, i. e. a chemical reaction driven by direct electric current. The metal to be polished is made the anode of an electrolytic cell, an electric current is applied and the resulting chemical reaction preferentially dissolves material from peaks on the surface of the anode, thus resulting in a reflective, smooth and even surface [Dav04]. Figure 4.4a displays a schematic illustration of the setup used to electropolish the Ti plates of the experiment cage. The Ti part with a surface area A is the anode in an electrolytic cell, a copper sheet with comparable surface area is the cathode. An electrolyte consisting of roughly 20 % per weight amidosulfonic acid in formamide was used, which is suitable for electropolishing of Ti according to [Buh09]. The process parameters were also taken from [Buh09]:

- A current density of around $1\,\mathrm{A/dm^2}$ was used (current I per surface area A of the Ti part to be polished).
- An electropolishing duration of roughly 10 min was applied.
- The electrolysis was done at room temperature.
- The electrolyte was not stirred.

Unfortunately, the electropolishing of the Ti plates did not result in a smooth and specular surface, like the one achieved in [Buh09]. On the contrary, as can be seen from the picture of a half-electropolished, half-handpolished Ti test part in figure 4.4b, electropolishing led to a rather poor surface quality, considerably worse than it was after the handpolishing. The Ti test part shown in figure 4.4b was first completely handpolished and afterwards everything but the bottom right corner was electropolished. As can be seen, the only handpolished part has a mirror finish, whereas the electropolished part is matt and rough with small shiny spots around the holes and partly a yellow coating. The shiny spots are probably due to gas bubbles that clung to the holes during the

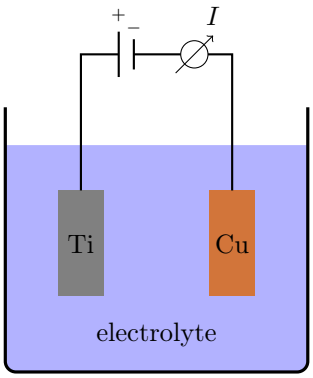

(a) Schematic of the electropolishing setup with the Ti part to be polished as the anode and a copper sheet as the cathode in an electrolytic cell. A mixture of 20 % per weight amidosulfonic acid in formamide was used as electrolyte (see [Buh09]). The current I was measured to set the current density to roughly 1 A/dm^2 (current I per surface area A of the Ti part). The electrolysis was stopped after 10 min. The electrolyte was at room temperature and it was not stirred.

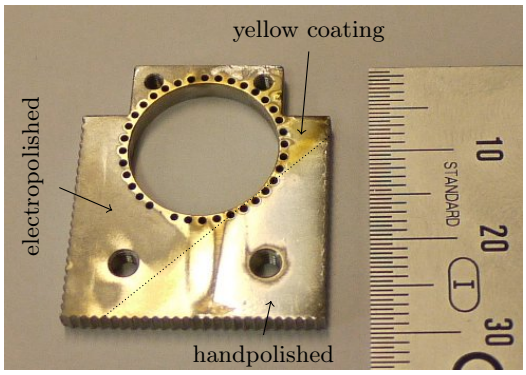

(b) A Ti test part that was only handpolished in the bottom right corner (shiny area) whereas the rest was handpolished and thereafter electropolished using the process parameters mentioned in the text. It exemplifies the poor surface quality caused by electropolishing: a matt and rough, partially yellow coated surface was produced.

Figure 4.4: The setup used for electropolishing the Ti parts is shown in (a). The poor surface quality of the electropolished Ti parts is exemplified in (b).

electrolysis, thus preventing the dissolution of Ti from the surface. The yellow coating may contain sulfur, concluding from its yellow color and the fact that amidosulfonic acid H_3NSO_3, one of the two components of the electrolyte, contains sulfur. Neither putting the electropolished parts in an ultrasonic bath with degreaser solution nor with acetone removed this yellow coating.

To summarize, electropolishing did not help preventing current breakthroughs by reducing the surface roughness as electropolishing produced a matt and rough surface with a partial yellow coating. Therefore, after electropolishing the first five Ti parts of the experiment cage, it was stopped. However, it may still be possible to reproduce the smooth and shiny electropolished Ti surface that was reported in [Buh09] by investing more time in optimizing the composition of the electrolyte and the process parameters, which are current density, duration, temperature and stirring.

4.2.2. Vacuum test for the electropolished Ti parts

The materials used for the experiment cage have to be compatible with ultrahigh vacuum (UHV, pressure between 10^{-7} and 10^{-14} mbar). As mentioned in section 4.1, Ti fulfills this requirement. However, it was unclear if the electropolished Ti parts of the experiment cage would still fulfill this demand, since they showed a yellow coating (see section 4.2.1),

for which the composition as well as the outgassing rate was unknown.

Therefore, an UHV test was done to test if the electropolished parts were still compatible with UHV. For this purpose, the electropolished parts were first cleaned following the steps described in appendix A. Afterwards the parts were put into a steel vacuum chamber. This vacuum chamber was then pumped by a two-part pumping station, consisting of a diaphragm backing pump and a turbopump. In addition, the vacuum chamber was baked up to a temperature of about 150 °C to increase the outgassing rate of potential contaminations inside the vacuum chamber, thereby making the pumping time shorter.

The first result of this UHV test was that the ultimate pressure of the used pumping station was reached, a pressure of 1×10^{-8} mbar [Pfe11]. Unfortunately, answering the question, if the pressure $p = 2 \times 10^{-11}$ mbar inside the glass cell could be reached with the electropolished parts, was not possible with the pumping station used.

The second result of the UHV test was that the mass spectrum, taken from the residual gas inside the vacuum chamber, looked liked a typical mass spectrum of a clean vacuum chamber. The electropolished Ti parts did not outgas an unusual substance. Figure 4.5a displays a typical residual gas mass spectrum of a baked-out, clean, not-leaking vacuum chamber, pumped by a turbopump, according to [Ber10]. Figure 4.5b depicts the mass spectrum taken from the residual gas in the baked-out test vacuum chamber with the electropolished Ti parts inside. The two mass spectra share the following peaks: single charged hydrogen molecule H_2^+ at the mass-to-charge ration $m/z = 2$, single charged carbon C^+ at $m/z = 12$, single charged oxygen O^+ at $m/z = 16$, OH^+ at $m/z = 17$, single charged water H_2O^+ at $m/z = 18$, single charged nitrogen molecule N_2^+ and carbon monoxide CO^+ at $m/z = 28$.

The measured mass spectrum (see figure 4.5b) has a few additional peaks. The peak at $m/z = 1$ probably belongs to single charged hydrogen H^+, appearing due to fragmentation of water molecules or hydrocarbons. The peak at $m/z = 8$ presumably belongs to doubly ionized oxygen O^{2+}. The peak at $m/z = 13$ may belong the the single charged carbon isotope $^{13}C^+$, although it is a little bit too high for the ^{13}C abundance of only 1.1 % [Gro11]. The peak at $m/z = 14$ can be assigned to single charged nitrogen N^+, doubly charged N_2^{2+} or CO^{2+}, or to acetone [Lid10], stemming from the cleaning of the electropolished Ti parts (see appendix A). Acetone is presumably also responsible for the peak at $m/z = 15$ and $m/z = 26$. Additionally, it contributes to the peaks at $m/z = 27$ and 28. The small peak at $m/z = 19$ is probably due to isopropanol [Lid10], another cleaning substance. Isopropanol also contributes to the peak at $m/z = 27$. The degreaser solution used for cleaning contains 2-Butoxyethanol [Bra13]. This substance possibly contributes to the peaks at $m/z = 27$ and 28 [Lid10].

The peak at $m/z = 44$ of single charged carbon dioxide CO_2^+ is missing in the measured mass spectrum displayed in figure 4.5b. This is probably due to the long pumping and baking of the test vacuum chamber of roughly three weeks. The pumping efficiency of a turbopump increases exponentially with $\sqrt{m}$, the square root of the mass [Ber10]. Therefore, when the turbopump was started, first the peaks at high m/z disappeared, followed by the disappearance of peaks at smaller and smaller mass-to-charge ratios the longer the turbopump was running, until eventually carbon dioxide was pumped away

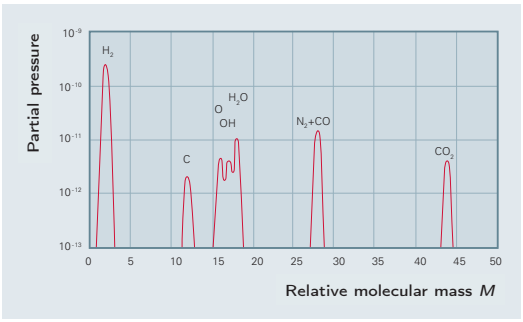

(a) Typical mass spectrum of the residual gas in a baked-out, clean, not-leaking vacuum chamber, pumped by a turbopump; taken from [Ber10].

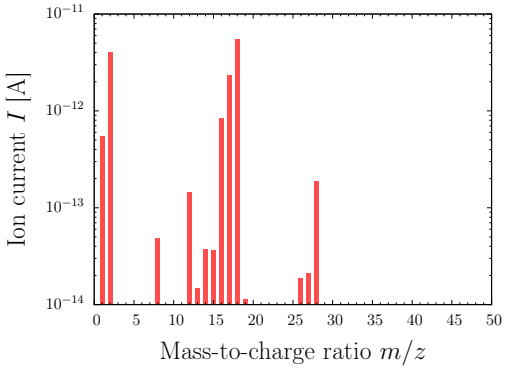

(b) Measured mass spectrum of the residual gas in the pumped and baked-out test vacuum chamber with the electropolished Ti parts inside. It is described in the text which substance is probably responsible for which peak. Important is that there are no sulfur peaks, i. e. no peaks at $m/z = 32$ and 34. Thus, if the yellow coating on the electropolished Ti parts (see figure 4.4b) contains sulfur, then at least it did not outgas.

Figure 4.5: Comparison between a typical mass spectrum of the residual gas in an UHV vacuum chamber (a) and the measured mass spectrum of the residual gas in the vacuum chamber with the electropolished Ti parts inside (b).

and the peak at $m/z = 44$ disappeared.

Especially important is that there are no peaks at $m/z = 32$ and 34 in the measured mass spectrum, i. e. the measured mass spectrum does not show an isotopic pattern of sulfur, as the two most abundant isotopes of sulfur are ^{32}S and ^{34}S [Gro11]. This was reassuring since there was the fear that the yellow coating on the electropolished Ti parts (see figure 4.4b) may contain sulfur and that this sulfur may outgas, making the usage of the electropolished Ti parts in UHV impossible.

To summarize, the vacuum test showed that the electropolished Ti parts were still compatible with UHV since the ultimate pressure of the used pumping station was reached and the mass spectrum clarified that the electropolished Ti parts did not outgas any large hydrocarbons or sulfur.

4.2.3. High voltage test for the experiment cage

As mentioned in section 4.2, it was unclear if current breakthroughs could occur between adjacent Ti plates in the experiment cage already at a voltage difference of a few kV due to the surface roughness of the Ti plates. Therefore, a high voltage test was done.

For this purpose, the assembled Ti cage was put in a test vacuum chamber. Opposing sides of the Ti cage were connected together and the three pairs of sides were then

connected to different feedthrough pins. Afterwards, the vacuum chamber was pumped to a pressure of 2.2×10^{-7} mbar. Finally, a high voltage $U = 2.5\,\mathrm{kV}$ was applied between two feedthroughs at a time, and this was done for all three possible combinations of two pins out of three. While the high voltage was applied, the current I between the two pins was measured. In addition, the high voltage was measured with a high voltage probe (1000:1 voltage divider) and monitored on an oscilloscope.

Fortunately no current breakthroughs occurred at this high voltage test. For all three contacting possibilities the measured current I was less than $0.00\,\mu\mathrm{A}$ and no breakdown of the high voltage U was observed on the oscilloscope. As mentioned, this test was done at a pressure of 2.2×10^{-7} mbar. For the lower pressure of 2×10^{-11} mbar inside the glass cell, the breakthrough voltage U_b is even higher (see figure 4.3).

To conclude, the high voltage test showed that there will be no current breakthroughs between adjacent Ti sides in the experiment cage up to a few kV, which is the maximum voltage which will be applied.

4.3. Assembly of the experiment cage

In the following the assembly of the experiment cage is described. First, the Ti and macor parts of the experiment cage were cleaned according to appendix A. Subsequently, 50 µm thin Ti wires were spanned over the apertures of the six Ti plates. Afterwards, the Ti cage was assembled, i. e. the six Ti plates and the four macor spacers were screwed together with Ti screws. Following this, the small rf coil was wound and slid onto the channeltron. Then, the channeltron[5] was mounted to the experiment cage. Subsequently, the MCP detector[6] was assembled. It consists of two microchannel plates, the front- and backplate, a contact ring for each of the two plates, and an anode at the rear end. Since the pin of the original contact ring of the backplate would have touched the glass cell, it was cut off and an additional contact ring was mounted, now with the pin pointing to the opposite side. The microchannels in the plates are biased at a small angle of 12° [Ham08] to the plate surface. The frontplate and the backplate have to be mounted 180° twisted against each other. Thereby, the microchannels of the two plates form a zigzag line when viewed from the side, thus ensuring that the ion to be detected hits one of the microchannels (see figure 5.9). After the assembly of the MCP detector, it was added to the experiment cage. Afterwards, wires were connected to the Ti plates, ion detectors and the rf coil, using inline barrel connectors. Except for the anode of the ion detectors and the rf coil, Kapton insulated copper wires were used with a diameter of 0.6 mm. The maximum voltage in vacuum for these wires is 2 kV [Kur09]. To avoid electromagnetic interference, coaxial cables were used to transmit the high frequency signals from the ion detector's anode and to transmit the rf alternating current of the rf coil. Finally, the two aspheric lenses were mounted, one to the bottom Ti side of the experiment cage, the other one to the top Ti side.

[5] PHOTONIS MAGNUM™ 5901 electron multiplier
[6] Hamamatsu F4655-13

4.4. Insertion of the experiment cage into the glass cell

After the assembly of the experiment cage was done (see section 4.3) the vacuum chamber was opened at the feedthrough octagon (see figure 3.1). Then the experiment cage was slid into the glass cell on a ramp of glass plates which were put into the glass tube that connects the feedthrough octagon with the glass cell. Once in the glass cell, the experiment cage was accurately positioned. Along the x-axis (see figure 4.6a), the experiment cage was pushed and pulled with the rigid coaxial cable from the anode of the MCP detector until the center of the experiment cage was aligned with the center of the quadrupole trap. Then this coaxial cable was fixed by a cable clamp inside the feedthrough octagon. Next, the positioning in the y-axis was done. For this the coaxial cable from the anode of the channeltron was guided in such a way that it presses the experiment cage to the wall of the glass cell (see figure 4.6a). The positioning in the z-axis was easy, as the experiment cage just stands on the bottom of the glass cell (see figure 4.6b). Following the positioning, the Kapton insulated copper wires and the coaxial cables from the experiment cage were connected to the feedthrough pins of the feedthrough octagon. The pin assignment can be found in appendix B. Finally, the vacuum chamber was closed again, pumped and baked out. Fortunately, also with the experiment cage inside the glass cell, a pressure of approximately 2×10^{-11} mbar was reached, i. e. the same pressure as before the insertion of the experiment cage.

To summarize, the experiment cage, which is an indispensable part of the setup for doing Rydberg experiments, was assembled, it was tested that it is compatible with UHV, it was also tested that there are no current breakthroughs between adjacent electrodes of the experiment cage, and finally the experiment cage was inserted into the glass cell.

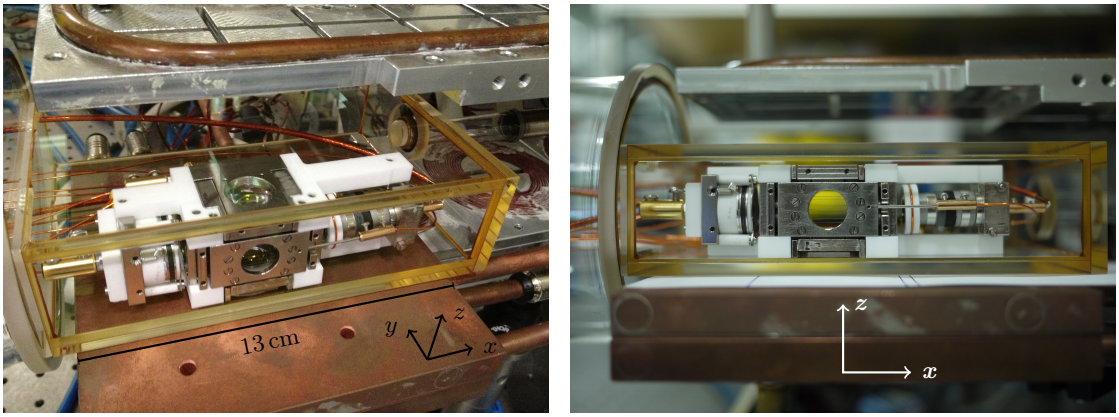

(a) Oblique view. (b) Side view.

Figure 4.6: Oblique (a) and side view (b) of the experiment cage after it was inserted into the glass cell.

5. Rydberg spectroscopy

In this chapter, the recording of a spectrum of a ^{87}Rb Rydberg S-state with the setup described in chapter 3 and 4 is discussed. First, the photoexcitation of the ^{87}Rb atoms to the Rydberg state is described in section 5.1. In section 5.2, the detection of Rydberg atoms via electric field ionization is reported. Subsequently in section 5.3, the recorded Rydberg spectrum of the ^{87}Rb 40S-state is presented. Finally, the effect of a DC electric field on the Rydberg atoms is discussed and a Stark map of the ^{87}Rb 40S-Rydberg-state is presented in section 5.4.

5.1. Two-photon excitation of Rydberg atoms

There are several possibilities to excite atoms to a Rydberg state, namely by charge exchange, via electron impact, with the use of photons or by a combination of collisional and optical excitation [Gal94]. In this work photoexcitation was used to excite Rydberg atoms since it allows to excite a specific Rydberg state, provided that the excitation lasers have narrow linewidths (see section 5.1.4).

Due to the selection rules of electric dipole transitions $l_f = l_i \pm 1$ [Sch07] where $l_{i,f}$ is the orbital angular momentum of the initial and final state respectively, using only one photon to excite ^{87}Rb atoms from their S-ground-state [Ste10] to a Rydberg state would have the major drawback that only the excitation of P-Rydberg-states would be possible. Therefore in this work, the photoexcitation of the ^{87}Rb atoms to a Rydberg state was done using two photons, i. e. via an intermediate P-state, thus we are able to excite S- and D-Rydberg-states. Also, for single-photon excitation of Rb Rydberg states, one would need light at a very short wavelength $\lambda \approx 298\,\mathrm{nm}$ (see below) which is difficult to produce.

The energy E_{nlj} of an alkali atom Rydberg electron in the state $|nlj\rangle$ (n: principal, j: total angular momentum quantum number) can be calculated using quantum defect theory [Gal94]. It accounts for the fact that the Rydberg electron of an alkali atom A can polarize and penetrate the A^+ core which changes the energy of an alkali atom Rydberg state from its hydrogenic counterpart [Gal94]. The energy E_{nlj} above the ground state is given by

$$E_{nlj} = E_\mathrm{i} - \frac{\mathcal{R}^*}{(n-\delta_{nlj})^2}, \tag{5.1}$$

where E_i is the ionization energy of the ground state [Mac11]. $\mathcal{R}^*$ is the Rydberg constant corrected for the reduced electron mass in the alkali atom A

$$\mathcal{R}^* = \frac{1}{1+\frac{m_\mathrm{e}}{m_\mathrm{A}}}\mathcal{R}_\infty, \tag{5.2}$$

with m_e and m_A the mass of the electron and alkali atom, respectively, and $\mathcal{R}_\infty$ the Rydberg constant with the infinite mass approximation for the atomic core. The quantum defect δ_{nlj} is calculated using the Rydberg-Ritz formula [Mac11]

$$\delta_{nlj} \approx \delta_0 + \frac{\delta_2}{(n-\delta_0)^2}, \tag{5.3}$$

quantity		value for ^{87}Rb
E_i		$h \cdot 1010.029\,164\,6\,\mathrm{THz}$
$\mathcal{R}^*$		$h \cdot 3289.821\,194\,66\,\mathrm{THz}$
$n\mathrm{S}_{1/2}$	δ_0	3.131 180 7
	δ_2	0.1787

Table 5.1: The values of the quantities which are needed for the calculation of the energy E_{nlj} of a ^{87}Rb $n\mathrm{S}_{1/2}$ Rydberg state with equation 5.1. E_i is the ionization energy for the ^{87}Rb $5\mathrm{S}_{1/2}$ $F = 1$ ground state, h is the Planck constant. The values are taken from [Mac11].

where the constants δ_0 and δ_2 are specific for each alkali atom isotope and they depend on l and j. The principal quantum number n corrected for the quantum defect δ_{nlj} is denoted effective principal quantum number

$$n^* \equiv n - \delta_{nlj}. \tag{5.4}$$

The values of the quantities which are needed for the calculation of the energy E_{nlj} for ^{87}Rb S-Rydberg states are given in table 5.1.

The calculation of the wavelength $\lambda = \frac{hc}{E_{nlj}}$ (h: Planck constant, c: speed of light) needed for single-photon excitation of the ^{87}Rb $40\mathrm{S}_{1/2}$ Rydberg state yields approximately 298 nm. There are no standard diode laser system at this wavelength as one needs frequency quadrupling to produce such a short wavelength with diode lasers [TOP12].

As mentioned above, two-photon excitation is used in this thesis to excite ^{87}Rb Rydberg atoms. Figure 5.1 illustrates the applied excitation scheme. One laser, a frequency doubled diode laser[7], operates at a wavelength $\lambda = 420.3\,\mathrm{nm}$ close to the lower transition from the ^{87}Rb $5\mathrm{S}_{1/2}$ ground state to the intermediate $6\mathrm{P}_{3/2}$ state. This laser is referred to as the 420 nm laser. Concurrently, an infrared diode laser[8] with wavelength in the range from $\lambda = 1000\,\mathrm{nm}$ to 1025 nm is used for the upper transition from the intermediate state either to an S- or a D-Rydberg state. By fine tuning of the infrared laser wavelength, one chooses the principal quantum number n and the orbital angular quantum number $l = \mathrm{S}$ or $l = \mathrm{D}$ of the excited Rydberg state. The experiments in this thesis were carried out using the $40\mathrm{S}_{1/2}$ Rydberg state. To excite to this Rydberg state the wavelength of the infrared laser has to be roughly 1020 nm (see section 5.3). Therefore, this laser is referred to as the 1020 nm laser. The utilized excitation scheme is referred to as the "inverted scheme" since the usually employed excitation scheme, referred to as the "normal scheme", uses the $5\mathrm{P}_{3/2}$ state as the intermediate state, resulting in the transition wavelengths 780 nm and 480 nm for the lower and upper transition, respectively. In the inverted scheme, the upper transition has a longer wavelength than the lower transition as opposed to the normal scheme. The inverted scheme was used because the available lasers at $\lambda = 1020\,\mathrm{nm}$ have a higher output power $P_{1020\,\mathrm{nm}} \approx 1\,\mathrm{W}$ [TOP12] than the

[7] Toptica TA-SHG pro series
[8] Toptica TA pro series

available laser at $\lambda = 480\,\mathrm{nm}$ with $P_{480\,\mathrm{nm}} \approx 300\,\mathrm{mW}$ [TOP12], resulting in a higher Rabi frequency for the inverted scheme compared to the normal scheme (see section 5.1.2).

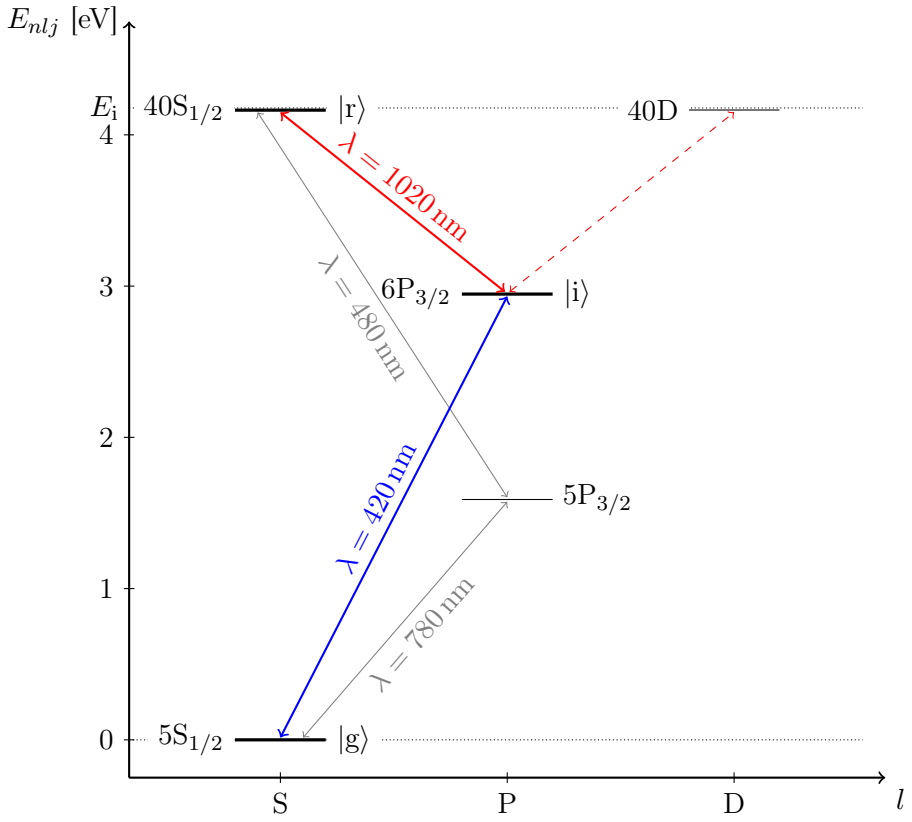

Figure 5.1: Simplified level scheme of ^{87}Rb to illustrate the inverted scheme used in this thesis for the two-photon excitation of $40S_{1/2}$ Rydberg atoms. One laser with wavelength $\lambda \approx 420\,\mathrm{nm}$ operates close to the lower transition from the $5S_{1/2}$ ground state $|\mathrm{g}\rangle$ to the $6P_{3/2}$ intermediate state $|\mathrm{i}\rangle$. For the upper transition from $|\mathrm{i}\rangle$ to either an S- or a D-Rydberg state $|\mathrm{r}\rangle$ an infrared laser with $\lambda \approx 1020\,\mathrm{nm}$ is used. The usually employed excitation scheme with $|\mathrm{i}\rangle = 5P_{3/2}$ is also plotted (gray arrows). The energy $E_{5P_{3/2}}$ is taken from [Ste10], $E_{6P_{3/2}}$ from [San06]. The energies for the Rydberg states $40S_{1/2}$, $40D_{3/2}$ and $40D_{5/2}$ were calculated with equation 5.1 and the required constants were taken from [Mac11]. Neither the small energy difference between the $40D_{3/2}$ and the $40D_{5/2}$ state is resolved in this plot, nor the approximately 1 meV higher energy of the 40D states compared to the $40S_{1/2}$ state. The ionization level E_i is plotted as a dotted line and E_i is taken from [Mac11].

5.1.1. The two-photon Rabi frequency

As discussed above, two-photon excitation is used in this thesis to excite ^{87}Rb atoms from the ground state via an intermediate state to a Rydberg state. Thus, the system under consideration is a three-level atom interacting with two light fields. The two light fields mediate a coupling of the ground state to the Rydberg state. The aim of this section is to introduce a measure for the strength of this coupling. As will be shown below, this measure is called the effective two-photon Rabi frequency Ω_{eff}.

A simplified level diagram, displaying the important quantities of the system is shown in figure 5.2. The three-level atom consists of the three states $|\text{g}\rangle$, $|\text{i}\rangle$ and $|\text{r}\rangle$ in a ladder configuration (see figure 5.1). The atomic resonance frequencies are ω_l and ω_u for the lower and upper transition, respectively. The two modes of the light field have the frequency $\omega_{\text{L,l}}$ and $\omega_{\text{L,u}}$, respectively. The detuning Δ_i to the intermediate state is defined as $\Delta_\text{i} \equiv \omega_{\text{L,l}} - \omega_\text{l}$. The two-photon detuning $\Delta_{2\gamma}$ is given by $\Delta_{2\gamma} \equiv (\omega_{\text{L,l}} + \omega_{\text{L,u}}) - (\omega_\text{l} + \omega_\text{u})$. Ω_l and Ω_u denote the single-photon Rabi frequencies of the lower and upper transition, respectively.

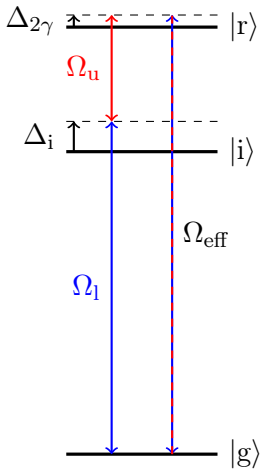

Figure 5.2: A three-level atom $\{|\text{g}\rangle, |\text{i}\rangle, |\text{r}\rangle\}$ interacting with two light modes can be reduced to an effective two-level atom $\{|\text{g}\rangle, |\text{r}\rangle\}$ interacting with a single light mode using the adiabatic elimination of the intermediate state. The adiabatic elimination is valid if the intermediate state is far-off-resonant to the lower light mode and therefore only weakly coupled ($|\Delta_\text{i}| \gg \Omega_\text{l}, \Omega_\text{u}$). Additionally the spontaneous decay of the Rydberg state $|\text{r}\rangle$ into the intermediate state has to be small. The effective two-photon Rabi frequency Ω_{eff} is a measure for the coupling strength between the two states $|\text{g}\rangle$ and $|\text{r}\rangle$. The other depicted quantities are introduced in the text.

If the detuning Δ_i to the intermediate state is large, i. e. $|\Delta_\text{i}| \gg \Omega_\text{l}, \Omega_\text{u}$, then the intermediate state $|\text{i}\rangle$ is only weakly coherently coupled. If additionally the spontaneous decay rate from the Rydberg to the intermediate state is small, then the intermediate state will not be significantly populated. Therefore, this state can be eliminated. Usually,

adiabatic elimination is used for this purpose which assumes that the temporal change of the population in the intermediate state is approximately zero [BPM07; Rui12]. The two mentioned conditions for elimination of the intermediate state are fulfilled for the experiments done in this thesis (see section 5.1.2). The elimination of the intermediate state results in a reduction of the three-level atom interacting with two light modes to an effective two-level atom $\{|\mathrm{g}\rangle, |\mathrm{r}\rangle\}$ interacting with a single light mode with the two-photon frequency $\omega_{\mathrm{L},2\gamma} = \omega_{\mathrm{L,l}} + \omega_{\mathrm{L,u}}$. The effective Hamiltonian of the reduced system is given by

$$\mathcal{H}_{\mathrm{eff}} = \frac{\hbar}{2} \begin{pmatrix} -\Delta_{2\gamma} & \Omega_{\mathrm{eff}} \\ \Omega_{\mathrm{eff}} & \Delta_{2\gamma} \end{pmatrix}, \tag{5.5}$$

in the interaction picture and under application of the rotating wave approximation [Hei08]. Hence, the coupling of the ground state to the Rydberg state is given by the effective off-resonant two-photon Rabi frequency Ω_{eff}, which is calculated with

$$\Omega_{\mathrm{eff}} = \sqrt{\Omega_{\mathrm{eff},0}^2 + \Delta_{2\gamma}^2}, \tag{5.6}$$

where $\Omega_{\mathrm{eff},0}$ is the effective resonant two-photon Rabi frequency [Hei08]. The experiments in this thesis were carried out with zero two-photon detuning, $\Delta_{2\gamma} = 0$. Hence, only $\Omega_{\mathrm{eff},0}$ is important in the context of this work and in the following it will be referred to as the two-photon Rabi frequency $\Omega_{2\gamma}$. According to [BPM07], it can be calculated with

$$\Omega_{2\gamma} \equiv \Omega_{\mathrm{eff},0} = \frac{\Omega_{\mathrm{l}}\Omega_{\mathrm{u}}}{2\Delta_{\mathrm{i}}}. \tag{5.7}$$

To obtain coherent coupling between the ground and Rydberg state, i. e. to be able to drive Rabi oscillations, the two-photon Rabi frequency $\Omega_{2\gamma}$ has to be much larger than the linewidth Γ_{r} of the Rydberg state and the linewidths $\Delta\nu_{\mathrm{l}}$ and $\Delta\nu_{\mathrm{u}}$ of the driving lasers [Low12].

5.1.2. Dipole matrix elements and Rabi frequencies for the lower and upper transition

The Rabi frequency Ω for a two-level atom with ground state $|\mathrm{g}\rangle$ and excited state $|\mathrm{e}\rangle$ interacting with a light field is given by

$$\Omega = \frac{\mathcal{E}\langle \mathrm{g}|er|\mathrm{e}\rangle}{\hbar} = \frac{\mathcal{E}\mu_{\mathrm{ge}}}{\hbar}, \tag{5.8}$$

where $\mathcal{E}$ is the electric field amplitude of the light field and $\langle \mathrm{g}|er|\mathrm{e}\rangle = \mu_{\mathrm{ge}}$ is the transition dipole matrix element [SZ08].

The amplitude $\mathcal{E}$ of the electric field of a laser beam is related to the light intensity I via:

$$\mathcal{E} = \sqrt{\frac{2I}{c\epsilon_0}}, \tag{5.9}$$

where c is the speed of light and ϵ_0 is the vacuum permittivity [Hec02]. In turn, the intensity at a position (x, y, z) in the beam can be calculated from the overall power P in the beam, if the beam shape is known. In particular, for Gaussian beams, the peak intensity I_0 on the optical axis is given by

$$I_0 = \frac{2P}{\pi w^2}, \tag{5.10}$$

where w is the $1/e^2$-width of the Gaussian beam [ST07]. The $1/e^2$-width is the radial distance from the optical axis where the intensity I drops to $1/e^2$ of its peak value I_0 on the optical axis.

To calculate the dipole matrix elements for the lower and upper transition, the involved states need to be specified more precisely than it is done in figure 5.1. Therefore, figure 5.3 displays the three states $|\mathrm{g}\rangle = 5\mathrm{S}_{1/2}$, $|\mathrm{i}\rangle = 6\mathrm{P}_{3/2}$ and $|\mathrm{r}\rangle = 40\mathrm{S}_{1/2}$ of ^{87}Rb with their respective hyperfine structure and with their Zeeman sublevels at zero magnetic field. The case of non-zero magnetic field is discussed below. The hyperfine structure results from the coupling of the nuclear spin $\mathbf{I}$ to the internally generated magnetic field due to the total electronic angular momentum $\mathbf{J}$ [Sch07]. The higher the principal quantum number n, the larger the orbital radius of the electron is ($\langle r\rangle \propto n^2$ [Gal94]), thus the smaller the magnetic field at the atomic core with which the nuclear spin interacts is. Therefore, the hyperfine splitting decreases for increasing n. For the $5\mathrm{S}_{1/2}$ ground state it is in the GHz regime. The exact value of 6835 GHz, taken from [Ste10], is depicted in figure 5.3. For the $6\mathrm{P}_{3/2}$ intermediate state the hyperfine splitting is a few tens of MHz and the values given in figure 5.3 come from [Var08].

For the $40\mathrm{S}_{1/2}$ Rydberg state, the hyperfine splitting is only 670 kHz [Mac11]. The hyperfine splittings of ^{87}Rb nS Rydberg states with $n \in [28, 33]$ were measured in [Li03]. Based on these measured values, an extrapolation formula $\Delta_{\mathrm{hfs},n\mathrm{S}} = 33.5\,\mathrm{GHz} \times (n^*)^{-3}$ is given in [Mac11] for the hyperfine interval between the $F = 1$ and $F = 2$ level of a ^{87}Rb nS Rydberg state. The extrapolated value for $n = 11$ deviates by 10 % from the measured value for this principal quantum number [Mac11]. The cited value of 670 kHz

for the hyperfine splitting of the $40S_{1/2}$ Rydberg state was calculated using the mentioned extrapolation formula. Although this hyperfine splitting of 670 kHz is small, it still can be resolved since it is much larger than the linewidths of the driving lasers which are in the range of a few kHz (see section 5.1.4). The hyperfine splitting is also larger than the Doppler width $\Delta\nu_{\mathrm{D}}$ which is approximately 70 kHz at a temperature $T = 5\,\mu\mathrm{K}$ of the atom cloud and with counter-propagating Rydberg excitation beams (see section 5.1.3).

The total angular momentum $\mathbf{F} = \mathbf{J} + \mathbf{I}$ takes the values $F = |J - I|, \ldots, J + 1$ and the magnetic quantum number m_F runs from $-F$ to $+F$ in steps of 1 [Sch07]. The isotope ^{87}Rb has a nuclear spin $I = 3/2$ [Ste10]. Therefore, the ^{87}Rb ground state $5S_{1/2}$ has for example two hyperfine levels $F = |\frac{1}{2} - \frac{3}{2}|, \ldots, \frac{1}{2} + \frac{3}{2} = 1, 2$ and the hyperfine level with $F = 2$ has five Zeeman sublevels with $m_F = -2, \ldots, 2$ as is depicted in figure 5.3.

The atom cloud in the QUIC trap is prepared in the $5S_{1/2}$ $F = 2$, $m_F = 2$ state via optical pumping (see section 3.1). The blue 420 nm laser has σ^+ polarization and therefore drives the transition to the the $6P_{3/2}$ $F = 3$, $m_F = 3$ state. It is approximately $2\pi \times 80\,\mathrm{MHz}$ blue detuned with respect to this level. Hence, the detuning Δ_{i} is approximately 56 times the natural linewidth $\Gamma = 2\pi \times 1.42\,\mathrm{MHz}$ of the $6P_{3/2}$ state [SWC04]. The infrared 1020 nm laser has σ^- polarization and thus drives the transition to the $40S_{1/2}$ $F = 2$, $m_F = 2$ Rydberg state.

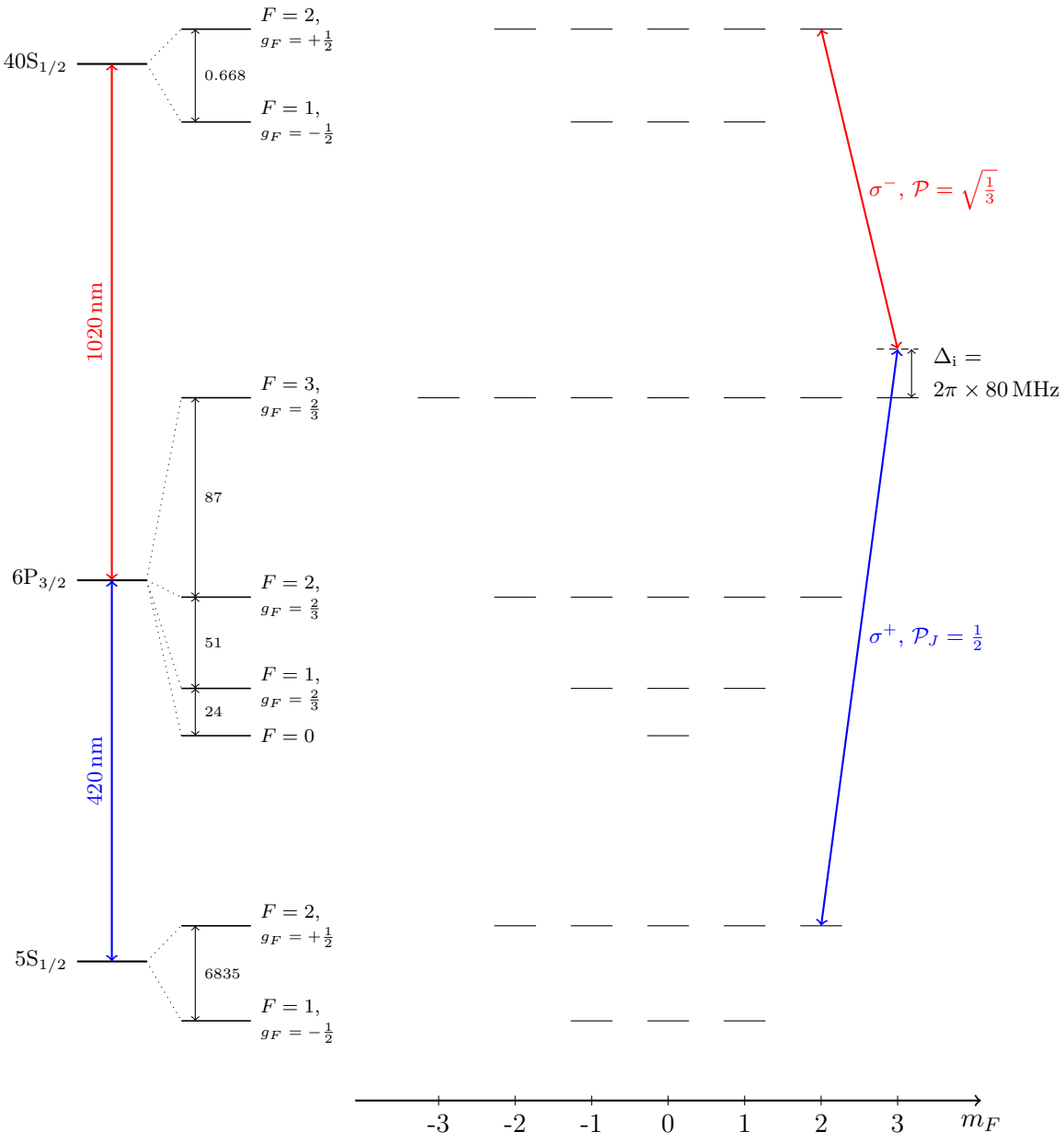

Figure 5.3: Detailed level scheme of the three ^{87}Rb states which are involved in the Rydberg excitation (compare figure 5.1). The hyperfine structure and the Zeeman sublevels at zero magnetic field are plotted for these three states. Additionally, the excitation path is displayed with the respective polarization of the driving lasers and the prefactors required for the calculation of the transition dipole matrix elements (see equations 5.11). The Landé g-factors for the respective hyperfine states are also given. The splitting in MHz between adjacent hyperfine states is specified, too. Note that different energy scales are used for the hyperfine structure of ground, intermediate and Rydberg state. The energy position of the intermediate state as well as the detuning Δ_i is not displayed to scale.

Consequently, the two dipole matrix elements

$$\mu_{\mathrm{gi}} = \langle n{=}5, L{=}0, S{=}\tfrac{1}{2}, J{=}\tfrac{1}{2}, I{=}\tfrac{3}{2}, F{=}2, m_F{=}2 \\ |er_{q=1}|n'{=}6, L'{=}1, S{=}\tfrac{1}{2}, J'{=}\tfrac{3}{2}, I{=}\tfrac{3}{2}, F'{=}3, m_{F'}{=}3\rangle$$

and

$$\mu_{\mathrm{ir}} = \langle n{=}6, L{=}1, S{=}\tfrac{1}{2}, J{=}\tfrac{3}{2}, I{=}\tfrac{3}{2}, F{=}3, m_F{=}3 \\ |er_{q=-1}|n'{=}40, L'{=}0, S{=}\tfrac{1}{2}, J'{=}\tfrac{1}{2}, I{=}\tfrac{3}{2}, F'{=}2, m_{F'}{=}2\rangle$$

need to be calculated, where the parameter $q = \{-1, 0, +1\}$ corresponds to $\{\sigma^+, \pi, \sigma^-\}$ transitions [Pri11]. The angular dependance of the dipole matrix element $\langle n, L, S, J, I, F, m_F|er_q|n', L', S, J', I, F', m_{F'}\rangle$ can be factored out as follows [BS68]

$$\begin{aligned}
&\langle n, L, S, J, I, F, m_F|er_q|n', L', S, J', I, F', m_{F'}\rangle \\
&\quad = (-1)^{F-m_F} \begin{pmatrix} F & 1 & F' \\ -m_F & q & m_{F'} \end{pmatrix} (L, S, J, I, F||er||L', S, J', I, F') && \text{(5.11a)} \\
&\quad = (-1)^{F-m_F+J+I+F'+1} \sqrt{(2F+1)(2F'+1)} \begin{pmatrix} F & 1 & F' \\ -m_F & q & m_{F'} \end{pmatrix} \begin{Bmatrix} J & F & I \\ F' & J' & 1 \end{Bmatrix} \\
&\qquad \times (L, S, J||er||L', S, J') \equiv \mathcal{P}_J \times (L, S, J||er||L', S, J') && \text{(5.11b)} \\
&\quad = (-1)^{F-m_F+J+I+F'+1+L+S+J'+1} \sqrt{(2F+1)(2F'+1)(2J+1)(2J'+1)} \\
&\qquad \times \begin{pmatrix} F & 1 & F' \\ -m_F & q & m_{F'} \end{pmatrix} \begin{Bmatrix} J & F & I \\ F' & J' & 1 \end{Bmatrix} \begin{Bmatrix} L & J & S \\ J' & L' & 1 \end{Bmatrix} \times (L||er||L') && \text{(5.11c)} \\
&\quad = (-1)^{F-m_F+J+I+F'+1+L+S+J'+1+L} \\
&\qquad \times \sqrt{(2F+1)(2F'+1)(2J+1)(2J'+1)(2L+1)(2L'+1)} \\
&\qquad \times \begin{pmatrix} F & 1 & F' \\ -m_F & q & m_{F'} \end{pmatrix} \begin{Bmatrix} J & F & I \\ F' & J' & 1 \end{Bmatrix} \begin{Bmatrix} L & J & S \\ J' & L' & 1 \end{Bmatrix} \begin{pmatrix} L & 1 & L' \\ 0 & 0 & 0 \end{pmatrix} \\
&\qquad \times \langle n, L, J|er|n', L', J'\rangle \equiv \mathcal{P} \times \langle n, L, J|er|n', L', J'\rangle, && \text{(5.11d)}
\end{aligned}$$

where the parentheses denote the Wigner-3j symbol and the curly braces the Wigner-6j symbol. The terms $(\dots||er||\dots)$ are referred to as the reduced matrix elements. The radial matrix element $\langle n, L, J|er|n', L', J'\rangle$ is defined as [BS68]

$$\langle n, L, J|er|n', L', J'\rangle = \int R^*_{n,L,J}(r) er R_{n',L',J'}(r) r^2 \mathrm{d}r, \tag{5.12}$$

where $R_{n,L,J}(r)$ and $R_{n',L',J'}(r)$ is the radial part of the electron's wavefunction for the ground state and the excited state, respectively. It is assumed that the radial wavefunction $R(r)$ depends on the principal, the orbital angular momentum and the total angular momentum quantum number, i. e. the effect of the spin-orbit coupling on the radial wavefunction is taken into account. The prefactor $\mathcal{P}_J$ in front of the reduced J-matrix element is introduced in equation 5.11b, whereas $\mathcal{P}$ denotes the prefactor in front of the radial matrix element, as defined in equation 5.11d. Since only the absolute value of the

Rabi frequency is of interest in the frame of this work, the sign of the two prefactors $\mathcal{P}_J$ and $\mathcal{P}$ will be neglected.

The reduced J-matrix element for the lower transition is given in [SWC04] as

$$(L{=}0, S{=}\tfrac{1}{2}, J{=}\tfrac{1}{2}||er||L'{=}1, S{=}\tfrac{1}{2}, J'{=}\tfrac{3}{2}) = 0.541 \cdot ea_0, \tag{5.13}$$

where atomic units ea_0 are used (a_0: Bohr radius). The prefactor $\mathcal{P}_J = 1/2$ for the lower transition. The reduced J-matrix element for the $5S_{1/2} \rightarrow 5P_{3/2}$ transition is also given in the reference [SWC04] as $5.956 \cdot ea_0$. Thus, it deviates only by 0.4 % from the value $5.979 \cdot ea_0$ which is given for this transition in [Ste10]. To compare the same quantities, the value $4.228 \cdot ea_0$ actually given in [Ste10] needs to be multiplied by a factor of $\sqrt{2J+1} = \sqrt{2}$, since the bracket convention $\langle \dots || er || \dots \rangle$ is used for the reduced matrix elements in reference [Ste10], which is related to the convention used here by $(L, S, J||er||L', S, J') = \sqrt{2J+1}\langle L, S, J||er||L', S, J'\rangle$ [Ste10].

For the radial matrix element of the upper transition into a Rydberg state with effective principal quantum number n^*, a $(n^*)^{-1.5}$ dependance is assumed, since the Rydberg state lifetime $\tau \propto (n^*)^3$ [Low12] and the radial matrix element squared is proportional to $1/\tau$ [Gal94]. The remaining proportionality constant μ_S for excitation of Rydberg S-states is determined using the value of $\langle n{=}6, L{=}1, J{=}\frac{3}{2}|er|n'{=}52, L'{=}0, J'{=}\frac{1}{2}\rangle = 2.47 \times 10^{-2} \cdot ea_0$ given in [Vit11]. This results in

$$\langle n{=}6, L{=}1, J{=}\tfrac{3}{2}|er|n', L'{=}0, J'{=}\tfrac{1}{2}\rangle = \mu_S \left([n']^*\right)^{-1.5} = 8.438 \cdot ea_0 \left([n']^*\right)^{-1.5}. \tag{5.14}$$

The prefactor $\mathcal{P}$ for the upper transition equals $\sqrt{\frac{1}{3}}$. The value of μ_S determined using the reference [Vit11] deviates only by 0.7 % from the value $\mu_S = 8.493 \cdot ea_0$ which we calculated. For this calculation, a model potential $V(r)$ for the valence electron of ^{87}Rb, taken from [MSD94], was put into the Hamiltonian $\mathcal{H} = \frac{p^2}{2m} + V(r) + \mathcal{H}_{fs} + \mathcal{H}_{hfs}$, where the Hamiltonian for the fine structure $\mathcal{H}_{fs}$ and the Hamiltonian for the hyperfine structure $\mathcal{H}_{hfs}$ can for example be found in [Sch07]. The radial part $R_{n,L,J}(r)$ of the electron's wavefunction was then numerically calculated by solving the Schrödinger equation, where the effect of $\mathcal{H}_{hfs}$ on the radial part was neglected. Subsequently, the radial matrix element $\langle n{=}6, L{=}1, J{=}\frac{3}{2}|er|n', L'{=}0, J'{=}\frac{1}{2}\rangle$ was calculated for $n' \in [20, 200]$. The fit of these radial matrix elements using a $([n']^*)^{-1.5}$ dependance yielded the μ_S-value cited above.

So far the Zeeman shift of the magnetic sublevels was not taken into consideration. The Zeeman energy shift $\Delta E_{|F,m_F\rangle}$ of a magnetic sublevel $|F, m_F\rangle$ exposed to a magnetic field B is given by $\Delta E_{|F,m_F\rangle} = \mu_B g_F m_F B$, where $\mu_B = 1.40\,\mathrm{MHz/G}$ is the Bohr magneton and $g_F(F, J, I, L, S)$ is the Landé g-factor [Ste10]. The g-factors for the respective hyperfine states of the ^{87}Rb ground state, intermediate state and Rydberg state are plotted in figure 5.3. They are calculated with the formula given in [Ste10]. The atoms held in the QUIC-trap are exposed to a magnetic field B of approximately 1 G. Therefore, the Zeeman sublevels are shifted approximately by 1 MHz compared to the case of zero magnetic field. For example, for the $40S_{1/2}$ $F = 2$, $m_F = 2$ state the Zeeman

energy shift amounts to +1.4 MHz. Considering the ground and intermediate state, the Zeeman shift is small compared to the hyperfine splitting and therefore the hyperfine F, m_F basis is still adequate to describe the system. However, for the Rydberg state the Zeeman and hyperfine splitting are of the same order. Thus, new eigenstates and eigenenergies need to be calculated for the Hamiltonian which contains both the Zeeman and hyperfine interactions. For a state with $J = 1/2$, the new eigenenergies are given by the Breit-Rabi formula [Woo83]. However, the dipole matrix element μ_{ir} for the upper transition used in this thesis is the same irrespective of the applied magnetic field. The reason for this is that the $40\mathrm{S}_{1/2}$ $F = 2$, $m_F = 2$ Rydberg state is a stretched state, i. e. it is a singular basis state in both the F, m_F and the new basis. This is due to the fact that for stretched states there is only one non-zero Clebsch-Gordon coefficient, and this coefficient is equal to 1 [Nol06].

Finally, the Rabi frequency Ω_{l} and Ω_{u} for the lower and upper transition used in this thesis can be calculated:

$$\begin{aligned}\Omega_{\mathrm{l}} &= \frac{\mathcal{E}_{0,\mathrm{l}} \cdot \mu_{\mathrm{gi}}}{\hbar} = \frac{\mathcal{E}_{0,\mathrm{l}}}{\hbar} \cdot \frac{1}{2} \cdot (L{=}0, S{=}\tfrac{1}{2}, J{=}\tfrac{1}{2} || er || L'{=}1, S{=}\tfrac{1}{2}, J'{=}\tfrac{3}{2}) \\ &= \frac{\mathcal{E}_{0,\mathrm{l}}}{\hbar} \cdot \frac{1}{2} \cdot 0.541 \cdot e a_0, \qquad (5.15a) \\ \Omega_{\mathrm{u}} &= \frac{\mathcal{E}_{0,\mathrm{u}} \cdot \mu_{\mathrm{ir}}}{\hbar} = \frac{\mathcal{E}_{0,\mathrm{u}}}{\hbar} \cdot \sqrt{\frac{1}{3}} \cdot \langle n{=}6, L{=}1, J{=}\tfrac{3}{2} | er | n', L'{=}0, J'{=}\tfrac{1}{2} \rangle \\ &= \frac{\mathcal{E}_{0,\mathrm{u}}}{\hbar} \cdot \sqrt{\frac{1}{3}} \cdot 8.438 \cdot e a_0 \left(n^*[40]\right)^{-1.5}. \qquad (5.15b)\end{aligned}$$

For the two Rydberg excitation lasers, the following parameters were typically used in this thesis:

- $P_{\mathrm{l}} = 100\,\mu\mathrm{W}$, $w_{\mathrm{l}} = 2\,\mathrm{mm}$,
- $P_{\mathrm{u}} = 190\,\mathrm{mW}$, $w_{\mathrm{u}} = 200\,\mu\mathrm{m}$,

where $P_{\mathrm{l,u}}$ is the power and $w_{\mathrm{l,u}}$ the width of the laser beam driving the lower and upper transition, respectively. Inserting these values into equation 5.15a and 5.15b, respectively, yields

- $\Omega_{\mathrm{l}} = 2\pi \times 380\,\mathrm{kHz}$,
- $\Omega_{\mathrm{u}} = 2\pi \times 13.279\,\mathrm{MHz}$,
- $\Omega_{2\gamma} = 2\pi \times 32\,\mathrm{kHz}$,

where the two-photon Rabi frequency was calculated with equation 5.7 for a detuning of $\Delta_{\mathrm{i}} = 2\pi \times 80\,\mathrm{MHz}$.

The detuning $\Delta_{\mathrm{i}} = 2\pi \times 80\,\mathrm{MHz}$ is much larger than the two Rabi frequencies Ω_{l} and Ω_{u}. Therefore, the first condition for the elimination of the intermediate state holds (see section 5.1.1).

Also the second condition for the elimination of the intermediate state is fulfilled. This is due to the fact that Rydberg states have very narrow linewidths as the lifetime τ of Rydberg states scales with the principal quantum number cubed, $\tau \propto n^3$ [Gal94]. For example, the calculation of the lifetime [Bet09] and natural linewidth of the ^{87}Rb $40S_{1/2}$ Rydberg state used in this thesis yields

$$\tau(40S_{1/2}, T = 300\,\mathrm{K}) = 36.254\,\mu\mathrm{s}, \tag{5.16a}$$

$$\Gamma(40S_{1/2}, T = 300\,\mathrm{K}) = \frac{1}{\tau} = 2\pi \times 4.39\,\mathrm{kHz}, \tag{5.16b}$$

where a temperature $T = 300\,\mathrm{K}$ of the environment was used. The black body radiation due to the surroundings induces dipole transitions from the Rydberg state to energetically nearby states, thus reducing the lifetime of the Rydberg state [Gal94]. With a linewidth of only $2\pi \times 4.39\,\mathrm{kHz}$, the spontaneous decay rate from the Rydberg to the intermediate state is very small.

Additionally, the two-photon Rabi frequency $\Omega_{2\gamma} = 2\pi \times 32\,\mathrm{kHz}$ is much larger than the natural linewidth $\Gamma = 2\pi \times 4.39\,\mathrm{kHz}$ of the $40S_{1/2}$ Rydberg state. Hence, the first condition for coherent coupling between ground and Rydberg state is fulfilled (see section 5.1.1).

5.1.3. Doppler broadening for co- and counter-propagating beams

Let us consider the following situation: an atom, with an atomic resonance frequency ω_0 at rest, moves with velocity $\mathbf{v}$ and gets excited by two co- or counter-propagating light beams along the z-axis. The light beams have the wavevectors $\mathbf{k}_1 = k_{1,z}\hat{\mathbf{e}}_z$ and $\mathbf{k}_2 = \pm k_{2,z}\hat{\mathbf{e}}_z$ and the frequencies ω_i, $i = 1, 2$, in the laboratory system, respectively. The sum wavevector $\mathbf{k} = (k_{1,z} \pm k_{2,z})\hat{\mathbf{e}}_z \equiv k_z\hat{\mathbf{e}}_z$ and the sum frequency ω in the laboratory system equals $\omega_1 + \omega_2$. Due to the Doppler effect [Dop42], the sum frequency ω in the laboratory system translates to $\tilde{\omega} = \omega - \mathbf{k} \cdot \mathbf{v}$ in the reference frame of the atom. The moving atom absorbs the light if $\tilde{\omega} = \omega_0$. Therefore, light with laboratory frequency $\omega = \omega_0 + k_z v_z$ is absorbed by the atom, where v_z is the z-component of the atom's velocity.

In a gas being in thermal equilibrium, the atoms have a Maxwell velocity distribution with the most probable velocity $v_\mathrm{p} = \sqrt{\frac{2k_\mathrm{B}T}{m}}$ [Dem93], where k_B is the Boltzmann constant, T the temperature of the gas, and m the mass of the atoms. The number $n(v_z)$ of atoms per volume with a velocity component $v_z \in [v_z, v_z + \mathrm{d}v_z]$ is thus given by

$$n(v_z)\mathrm{d}v_z = \frac{N}{v_\mathrm{p}\sqrt{\pi}} \exp\left\{-\left(\frac{v_z}{v_\mathrm{p}}\right)^2\right\} \mathrm{d}v_z, \tag{5.17}$$

where N is the overall atom density. Inserting $v_z = \frac{\omega - \omega_0}{k_z}$ and $\mathrm{d}v_z = \frac{\mathrm{d}\omega}{k_z}$ yields the number $n(\omega)$ of atoms per volume which absorb light with a frequency $\omega \in [\omega, \omega + \mathrm{d}\omega]$:

$$n(\omega)\mathrm{d}\omega = \frac{N}{v_\mathrm{p}k_z\sqrt{\pi}} \exp\left\{-\left(\frac{\omega - \omega_0}{v_\mathrm{p}k_z}\right)^2\right\} \mathrm{d}\omega. \tag{5.18}$$

The absorbed intensity $I(\omega)$ is proportional to $n(\omega)$:

$$I(\omega) = I(\omega_0) \exp\left\{ -\left(\frac{\omega - \omega_0}{v_\mathrm{p} k_z} \right)^2 \right\}. \tag{5.19}$$

Therefore, the absorption line of a gas of atoms with temperature T is broadened due to the Doppler effect. The full width at half maximum (FWHM) of the Gaussian profile of the absorbed intensity $I(\omega)$ is referred to as the Doppler width $\Delta\omega_\mathrm{D} = 2\sqrt{\ln 2} v_\mathrm{p} k_z$ (angular frequency). Using $k_z = \frac{2\pi}{c}(\nu_1 \pm \nu_2)$ with the frequencies $\nu_i = \omega_i / 2\pi$, $i = 1, 2$, of the co- or counter-propagating beams, yields the frequency Doppler width

$$\Delta\nu_\mathrm{D} = \sqrt{\frac{8 \ln 2 \, k_\mathrm{B} T}{mc^2}} (\nu_1 \pm \nu_2). \tag{5.20}$$

In the scope of this work, m is the mass of ^{87}Rb, ν_1 is the frequency ν_l of the lower transition and ν_2 is the frequency ν_u of the upper transition (see figure 5.1). For co-propagating excitation beams (+), the Doppler width is larger than for counter-propagating (−) beams. This can also be seen in figure 5.4, where the Doppler width $\Delta\nu_\mathrm{D}$ is plotted as a function of the temperature T for ^{87}Rb and the excitation frequencies of the inverted scheme used in this thesis for both co- and counter-propagating beams.

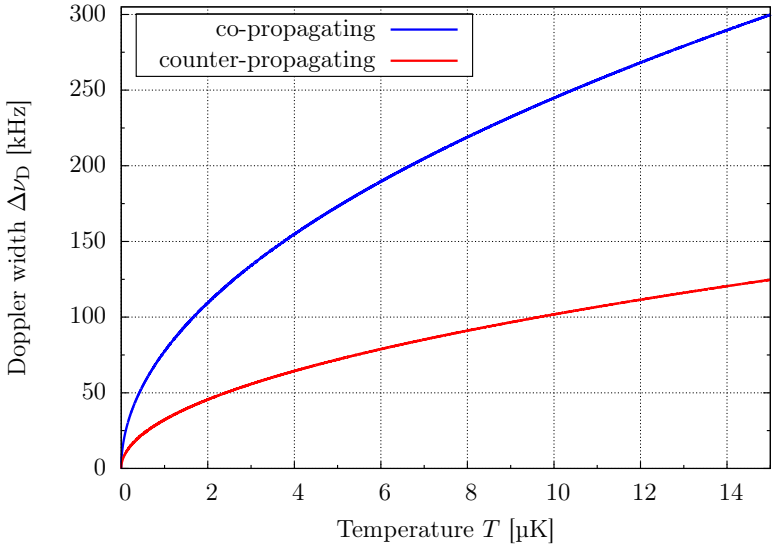

Figure 5.4: Doppler width as a function of the temperature of the atom cloud for co- and counter-propagating excitation beams. The shown curves are calculated with equation 5.20 for the mass of ^{87}Rb and the inverted excitation scheme (see figure 5.1).

5.1.4. Linewidth of the Rydberg excitation lasers

To be able to do high-resolution spectroscopy of Rydberg states, the linewidth $\Delta\nu_\mathrm{L}$ of the Rydberg excitation lasers has to be narrower than or at least as narrow as the linewidth Γ_r of the Rydberg state [Dem93], which is in the range of a few kHz (compare equation 5.16b).

The theoretical limit of the laser linewidth $\Delta\nu_\mathrm{L}$ is given by the Schawlow-Townes formula [Dem93]

$$\Delta\nu_\mathrm{L} \geq \frac{\pi h\nu_\mathrm{L}\Delta\nu_\mathrm{C}^2}{P_\mathrm{L}} \sim \frac{\Delta\nu_\mathrm{C}}{\Gamma_\mathrm{ph}}\Delta\nu_\mathrm{C}, \tag{5.21}$$

where ν_L is the laser frequency, $P_\mathrm{L} = h\nu_\mathrm{L}\Gamma_\mathrm{ph}$ the laser power, Γ_ph the laser photon rate, and $\Delta\nu_\mathrm{C}$ the full width at half maximum (FWHM) of a resonance of the laser-resonator. Inserting the respective laser frequencies and typical powers (see section 5.1.2) for the 420 nm and the 1020 nm laser yields theoretical linewidth limits $\Delta\nu_\mathrm{L}$ in the mHz and µHz regime, respectively, where $\Delta\nu_\mathrm{C} = 1\,\mathrm{MHz}$ was assumed for the Toptica external-cavity diode lasers used in this thesis.

However, the theoretical linewidth is by far not achieved in practice. For example, the linewidth for the two Rydberg excitation lasers used in this thesis is specified to lie in between 100 kHz and 1 MHz [TOP12] if the frequency is not stabilized. There are various reasons for the technical linewidth being much larger than the theoretical limit, for example noise of the laser diode current, vibrations of the laser-resonator, as well as temperature and air pressure fluctuations inside the laser-resonator [Dem93; TOP12]. These fluctuations influence either the length L of the laser-resonator or the refractive index n_ref inside it and thereby the frequency $\nu = m\frac{c}{2n_\mathrm{ref}L},\ m \in \mathbb{N}$, of the laser-resonator modes [Dem93].

To make the linewidth of the Rydberg lasers at least as narrow as the linewidth of the excited Rydberg state, their frequencies have to be stabilized (commonly referred to as "locked"). Locking the frequency of a laser requires a frequency standard to which the laser frequency is compared and a feedback loop that adjusts the laser frequency if it deviates from the frequency standard [Dem93]. In this thesis, a temperature stabilized ultra-low expansion (ULE) Fabry-Pérot cavity[9] with a free spectral range $\nu_\mathrm{FSR} = 1.5\,\mathrm{GHz}$ serves as the frequency standard. The Pound-Drever-Hall (PDH) technique [Dre83; Bla01] is used to get a dispersive signal, i. e. an error signal, from the ULE-cavity. This error signal is then fed back to the laser to adjust its frequency, either by adapting the tilt of the Littrow grating [Dem93; TOP12] or by tuning the diode current. Due to the ultra-low expansion and the stabilized temperature of the cavity, the reference frequency is very stable over time. The relative frequency variation $\Delta\nu/\nu$ of the ULE-cavity is approximately given by $10^{-9}(T-T_\mathrm{c})^2$ [Aln08], where T is the temperature of the cavity and T_c the critical temperature where the coefficient of linear thermal expansion of the ULE glass has a zero crossing. The temperature controller[10] used to set the cavity

[9] Stable Laser Systems
[10] Wavelength Electronics LFI-3751

temperature T to T_c is specified to have a long term stability (24 hours) of $< 0.005\,°C$. Using this value yields a frequency variation of only 10 Hz over 24 hours, calculated for 780 nm light. Therefore, the frequency drift of the laser locked to this cavity will also be very small. Additionally, the high finesse $\mathcal{F} \approx 15\,000$ of the cavity results in the error signal having a very steep slope which allows for a very narrow linewidth of the locked laser [Bla01].

In the scope of this work, both Rydberg excitation lasers, the 420 nm and the 1020 nm laser, were locked to the ULE-cavity using the PDH technique. Besides, the frequency of an additional 780 nm diode laser[11] was stabilized with the help of the ULE-cavity. This laser is referred to as the master laser since the imaging laser and the MOT lasers (see chapter 3) are locked relative to this laser. A detailed description of the optical and electronic setup used for the laser locking can be found in [Tre12].

The linewidth of the locked Rydberg lasers was measured with a delayed self-heterodyne interferometer (DSHI). For this purpose, the beam of the laser for which one wants to measure the linewidth, is split up in two beams. One beam is coupled into a 10 km long fiber, the other beam is passed through an AOM to shift its frequency by 80 MHz. Afterwards, the two beams are overlapped again and the beatnote signal between the two beams is detected with a fast photodiode and recorded with a spectrum analyzer. A schematic illustration of the DSHI setup used can be found in [Bal09]. The measured beatnote signals for the locked 420 nm and the 1020 nm laser are depicted in figure 5.5a and 5.5b, respectively. They show a central peak at approximately 80 MHz which is the frequency the second beam is shifted by the AOM with respect to the first. In the wings the recorded beatnote signals display oscillations with a frequency of roughly $20\,\text{kHz} = \frac{1}{\tau_d}$, where $\tau_d = 52\,\mu\text{s}$ [Bal09] is the delay time imposed on the first beam by passing through the 10 km long fiber. These oscillations emerge if the linewidth of the measured laser is considerably less than the resolution limit of 20 kHz of the used DSHI setup [Bal09]. Therefore the conclusion to be drawn from the DSHI linewidth measurements is that the linewidths $\Delta\nu_l$ and $\Delta\nu_u$ of the 420 nm and the 1020 nm laser, respectively, are clearly less than 20 kHz. Thereby, they are in the range of the linewidth Γ_r of the Rydberg states. Additionally, the linewidths $\Delta\nu_l$ and $\Delta\nu_u$ are smaller than the two-photon Rabi frequency $\Omega_{2\gamma}$ (see section 5.1.2), which facilitates coherent coupling between ground and Rydberg state (see section 5.1.1). The small additional peak on the right side of the central peak in figure 5.5a is probably due to pick up of rf-signals by the long wires from the laser to the DSHI setup or by the cable from the photodiode to the spectrum analyzer [Tre12].

The linewidth of the locked 780 nm master laser was determined by a heterodyne measurement with a second Toptica DL pro 780 nm laser locked to a comparable ULE-cavity. The beams of the two lasers were overlapped and the resulting beatnote signal was detected with a fast photodiode and recorded with a spectrum analyzer. Figure 5.5c displays this beatnote signal. A Gauss-fit to the central peak yields a width $\Delta\nu_{beat} = 5.2\,\text{kHz}$. As is shown in [Bal09], the width $\Delta\nu_{beat}$ of the beatnote signal sets an upper

[11] Toptica DL pro series

limit for each of the two widths of the involved lasers, i. e. the linewidth $\Delta\nu_{\text{master}}$ of the master laser is smaller than or equal to $\Delta\nu_{\text{beat}}$. However, for $\Delta\nu_{\text{master}}$ to be equal to $\Delta\nu_{\text{beat}}$, the linewidth of the second laser had to be zero which is not the case (see the Schawlow-Townes formula 5.21). Therefore, one can conclude that $\Delta\nu_{\text{master}} < 5.2\,\text{kHz}$. Assuming that both beat 780 nm lasers have a Gaussian shaped spectrum with the same linewidth, then the linewidth of the locked master laser is given by $\Delta\nu_{\text{master}} = \frac{\Delta\nu_{\text{beat}}}{\sqrt{2}} = 3.7\,\text{kHz}$ [Bal09].

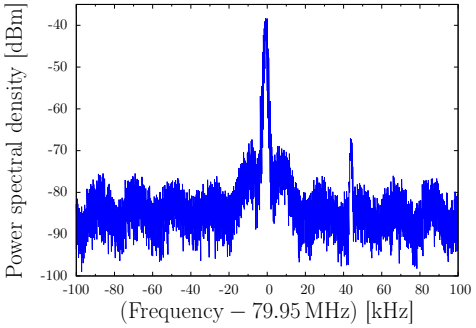

(a) Beatnote signal of the DSHI measurement for the 420 nm laser.

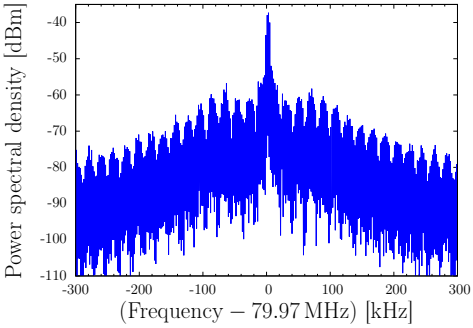

(b) Beatnote signal of the DSHI measurement for the 1020 nm laser.

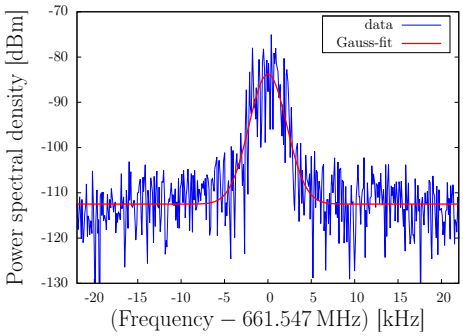

(c) Beatnote signal of the heterodyne measurement for the 780 nm master laser.

Figure 5.5: Measurements to determine the linewidth of the locked Rydberg lasers, the 420 nm laser (a) and the 1020 nm laser (b), as well as the linewidth of the locked 780 nm master laser (c). For the two Rydberg lasers, a delayed self-heterodyne interferometer (DSHI) measurement was done, yielding that the laser linewidths are considerably smaller than 20 kHz. A heterodyne measurement with a second locked 780 nm laser was performed for the master laser with which the linewidth of the master laser could be determined to be smaller than 5.2 kHz. The measured beatnote signals are displayed in such a way that the central peak is located at zero frequency. The frequency, by which the respective beatnote signal was shifted to achieve this, is given in the respective label of the frequency axis.

5.1.5. Spectroscopy of the $5S_{1/2}$ to $6P_{3/2}$ transition

As mentioned in section 5.1.2 and depicted in figure 5.3 the 420 nm laser is $\Delta_i = 2\pi \times 80\,\text{MHz}$ blue detuned to the intermediate state ^{87}Rb $6P_{3/2}$, $F = 3$, $m_F = 3$. In order to set the frequency of the 420 nm laser to such a value that this detuning of $2\pi \times 80\,\text{MHz}$ is obtained, a spectrum of the $5S_{1/2} \rightarrow 6P_{3/2}$ transition was recorded.

The spectroscopy was done in a hot Rb vapor cell and the saturation spectroscopy method was used to circumvent Doppler broadening of the transitions [Dem93]. Also in this reference [Dem93], a schematic illustration of the experimental setup for saturation spectroscopy can be found.

Figure 5.6a displays an overview spectrum (blue line) of the $5S_{1/2} \rightarrow 6P_{3/2}$ transition. It shows the normalized transmission of the weak probe beam (see [Dem93]), which goes through the Rb vapor cell, as a function of the frequency. In the experiment the laser frequency is swept and the transmission is recorded as a function of time. The time scale is converted to a frequency scale with the help of the cavity signal which is displayed as the red line in figure 5.6a. In order to lock the frequency of the 420 nm laser, the 840 nm non-frequency-doubled light of this laser is coupled into an ULE-cavity (see section 5.1.4). The red line in figure 5.6a is the transmission signal of this ULE-cavity for the 840 nm light. It shows four main peaks, referred to as the carrier peaks. They belong to the TEM_{00} mode of the cavity [Dem93; EE10]. The distance between two adjacent carrier transmission peaks is the free spectral range ν_{FSR} of the cavity [Dem93]. For the ULE-cavity we used the free spectral range ν_{FSR} equals 1.5 GHz, as mentioned in section 5.1.4. On the right side of each carrier peak the cavity transmission signal of this specific measurement has two additional small peaks. They belong to higher transversal modes of the cavity [EE10; Tre12]. By improving the coupling of the 840 nm light into the ULE-cavity the height of these peaks can reduced such that they can not be distinguished from the noise of the cavity baseline anymore. A different frequency scale is used in figure 5.6a for the atomic spectrum, which is recorded with 420 nm light, compared to the cavity signal, which belongs to the 840 nm light, since the frequency of the 420 nm light changes twice the frequency of the 840 nm light changes in a given sweep time.

The transmission in figure 5.6a features three clearly visible dips. The largest dip, centered at approximately 1 GHz, belongs to the ^{85}Rb isotope and it relates to the transition from the $F = 3$ hyperfine level of the ground state into the excited $6P_{3/2}$ state. The dip centered at roughly 4 GHz also belongs to ^{85}Rb, however to the transition from the $F = 2$ hyperfine level of the ground state into the excited state. The dip centered at approximately 7 GHz relates to the transition from the $F = 1$ hyperfine level of the ^{87}Rb ground state into the $6P_{3/2}$ excited state. The dip which belongs to the transition from the $F = 2$ hyperfine level of the ^{87}Rb ground state into the excited state is not very pronounced as it lies on the left flank of the ^{85}Rb $F = 3$ dip. The measured frequency splittings between the ground state hyperfine levels of both Rb isotopes are also plotted in figure 5.6a and they are listed in table 5.2. There, these measured frequency splittings are compared to literature values taken from [Var08]. Figure 5.7a is taken from this reference, too. It displays the level scheme of the $5S_{1/2} \rightarrow 6P_{3/2}$ transition for both Rb

isotopes with the hyperfine splitting of the ground state as well as the excited state. The deviation between the measured values and the literature values is probably due to the fact that the scan velocity of the used laser is not perfectly constant as a function of time. This manifests itself in different time spacings for different pairs of adjacent carrier peaks where this time spacing should be the same irrespective of which pair of adjacent carrier peaks is looked at. Thus, the conversion of the time scale to a frequency scale is fraught with errors.

As can be seen in figure 5.6a there is no carrier cavity transmission peak close to the ^{87}Rb $F = 2$ peak. Therefore, sideband frequencies are modulated onto the 420 nm laser beam by an electro-optic modulator (EOM) [Aln08; Tre12]. Figure 5.6b displays a detailed view of the spectrum around the sideband the 420 nm laser is locked onto. It shows two small peaks in the ^{87}Rb $F = 2$ dip. The right peak is most probably related to the transition into the $6P_{3/2}$ $F' = 3$ hyperfine level. As the detuning Δ_i is measured relative to this level this peak is chosen for the origin of the frequency scale. The left peak probably belongs to the crossover resonance co(2,3) [Dem93] between the hyperfine levels $F' = 2$ and $F' = 3$ of the excited state. This assignment of the peaks is based on the fact that in the ^{85}Rb $F = 3$ dip the corresponding peaks of the crossover resonance co(3,4) and the $F' = 4$ hyperfine level are the strongest two peaks (see figure 5.7b). Besides, the measured frequency distance between the co(2,3) peak and the $F' = 3$ peak fits its literature value (see table 5.2). Unlike for the ^{85}Rb $F = 3$ dip, there are no additional peaks of other excited state hyperfine levels visible for the ^{87}Rb $F = 2$ dip. This is due to the fact that the ^{87}Rb $F = 2$ dip lies on the flank of the ^{85}Rb $F = 3$ dip, as already mentioned. Having identified the peak in the spectrum which belongs to the intermediate state, one sideband is then put 280 MHz blue detuned to this $F' = 3$ peak by using an EOM frequency of 541 MHz as can be seen in figure 5.6b. In order to be able to switch the 420 nm light on and off, it passes an acusto-optic modulator (AOM) before it excites the Rb atoms. The AOM causes a frequency shift of the light passing through it [ST07]. In the scope of this thesis, the 420 nm light in the -1st diffraction order of a 200 MHz AOM was used to excite the Rb atoms. This light has a frequency 200 MHz smaller than the light entering the AOM. Therefore, by locking the 420 nm laser onto the sideband shown in figure 5.6b the desired detuning $\Delta_i = 2\pi \times 80$ MHz is obtained.

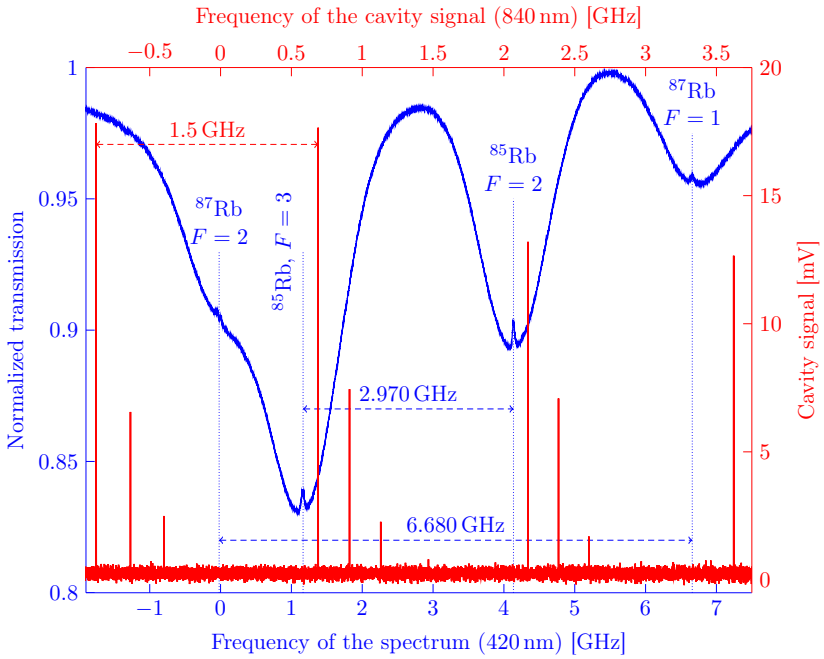

(a) Overview spectrum of the $5S_{1/2} \rightarrow 6P_{3/2}$ transition.

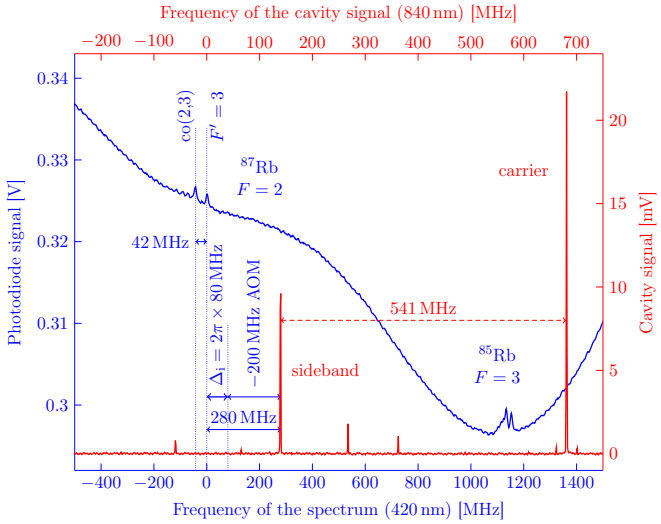

(b) Detailed view of the spectrum.

Figure 5.6: Spectroscopy of the Rb $5S_{1/2} \rightarrow 6P_{3/2}$ transition with the 420 nm laser. An overview spectrum (blue line) is shown in (a). The red line is the cavity transmission signal for the 840 nm light. It features carrier transmission peaks at a frequency spacing of 1.5 GHz. Sidebands are modulated onto the laser beam by an EOM to be able to lock the 420 nm light to the desired frequency corresponding to a detuning $\Delta_i = 2\pi \times 80$ MHz to the intermediate state ^{87}Rb $6P_{3/2}$, $F' = 3$. The sideband the 420 nm is locked to is shown in (b).

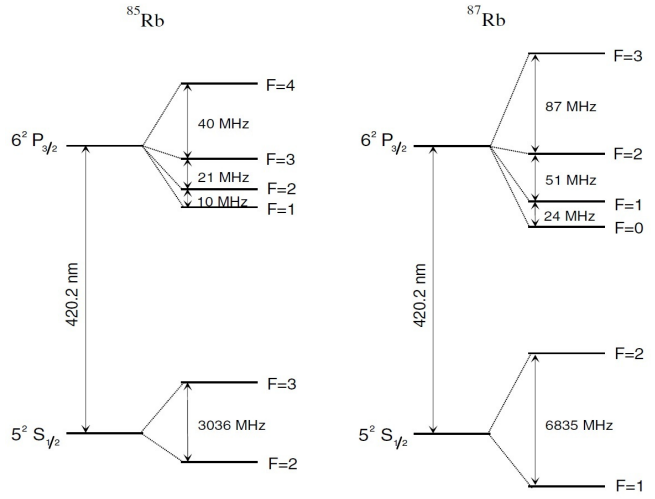

(a) Level scheme of the $5S_{1/2} \rightarrow 6P_{3/2}$ transition for both Rb isotopes with hyperfine structure, taken from [Var08].

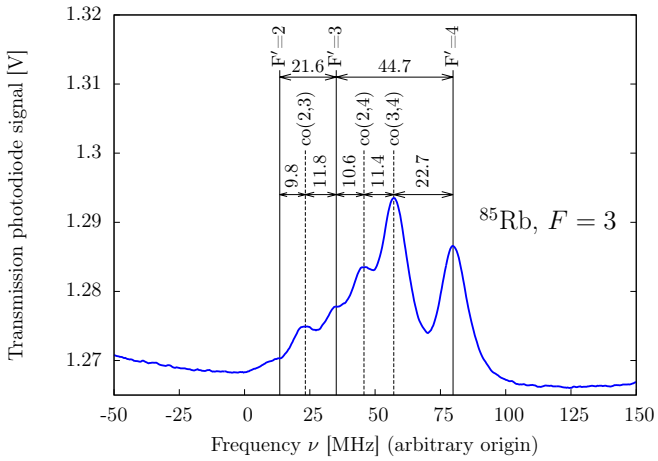

(b) Detailed view of the spectral dip corresponding to the ^{85}Rb $5S_{1/2}$, $F = 3 \rightarrow 6P_{3/2}$ transition.

Figure 5.7: The level scheme of the $5S_{1/2} \rightarrow 6P_{3/2}$ transition for the ^{85}Rb and the ^{87}Rb isotope is depicted in (a). It shows the hyperfine structure of the ground state and the excited state with the frequency difference between adjacent hyperfine levels. These frequency differences were measured in reference [Var08]. A detailed view of ^{85}Rb $F = 3$ dip (see figure 5.6a), measured in the scope of this work, is displayed in (b). Using saturation spectroscopy it was possible to resolve the hyperfine structure of the excited state. It is labeled with which peak corresponds to which hyperfine level of the excited state. The frequency differences between adjacent peaks are also plotted. In table 5.2 they are compared to the values given in subfigure (a).

hfs frequency splitting	measured [MHz]	literature [MHz]	deviation [%]
$\Delta\nu^{^{87}\mathrm{Rb}}_{F=1\leftrightarrow F=2}$	6680	6835	−2.3
$\Delta\nu^{^{85}\mathrm{Rb}}_{F=2\leftrightarrow F=3}$	2970	3036	−2.2
$\Delta\nu^{^{87}\mathrm{Rb}}_{F'=2\leftrightarrow F'=3}$	84	87	−3.4
$\Delta\nu^{^{85}\mathrm{Rb}}_{F'=2\leftrightarrow F'=3}$	22	21	+4.8
$\Delta\nu^{^{85}\mathrm{Rb}}_{F'=3\leftrightarrow F'=4}$	45	40	+12.5

Table 5.2: Comparison between the measured hyperfine structure (hfs) frequency splittings $\Delta\nu$ (see figure 5.6 and figure 5.7b) and the ones taken from reference [Var08]. The unprimed F's refer to the hyperfine levels of the $5S_{1/2}$ ground state and the primed ones refer to the excited state $6P_{3/2}$.

5.2. Ionization and detection of Rydberg atoms

After the photoexcitation of Rydberg atoms was described in the previous section 5.1, this section discusses the electric field ionization and the detection of Rydberg atoms.

As is shown in reference [Gal94], the classical electric field $\mathcal{E}_{\text{ion}}$ required to ionize a Rydberg state with effective principal quantum number n^* is given by

$$\mathcal{E}_{\text{ion}} = \frac{\pi\epsilon_0}{e^3}\frac{(\mathcal{R}^*)^2}{(n^*)^4}, \tag{5.22}$$

where ϵ_0 is the vacuum permittivity, e the elementary charge and $\mathcal{R}^*$ the corrected Rydberg constant (see section 5.1). Tunneling processes of the Rydberg electron and the Stark shift of the energy levels in an electric field (see section 5.4) are not taken into account for the derivation of equation 5.22. However, in practice these effects are negligible for the calculation of $\mathcal{E}_{\text{ion}}$ [Gal94].

As described in section 4.1 the required ionization field is produced by applying a high voltage to one of the electrodes of the experiment cage. Depending on whether the MCP detector or the channeltron (see section 4.1 and below) is used for the detection of the Rydberg ions, a high positive voltage is either applied to the electric field plate in front of the channeltron or to that in front of the MCP detector. The required voltage U_{ion} to produce the ionization electric field $\mathcal{E}_{\text{ion}}$ at the center of the experiment cage is calculated in [Tre12]. For the ^{87}Rb $40S_{1/2}$ Rydberg state the applied voltage U_{ion} has to be at minimum 400 V according to these calculations. For the experiments done in the scope of this thesis, normally an ionization voltage of roughly 1 kV was used.

In order to avoid that the Rydberg energy level is Stark shifted during the photoexcitation, the ionization field is switched on only after the Rydberg excitation (see figure 5.11). The electric field is then on for approximately 50 µs. Subsequently, it is switched off again before the next excitation pulse of the 420 nm laser happens at the next frequency step (see figure 5.11). For the switching of the electric field, a fast high voltage switch[12] with a switching time of approximately 10 ns and a maximum voltage of 6 kV was used.

After the ionization of the Rydberg atoms, the Rydberg ions are either detected with an MCP detector or a channeltron, as already mentioned in section 4.1. The basic component of these two ion detectors is the electron multiplier tube. The principle of electron multiplication in this tube is illustrated in figure 5.8a. The tube is made out of glass, resulting in a very high resistance in the range of GΩ between the electrode on the input side and the output side [Wiz79; Ham13]. Between these two electrodes, a high dynode voltage V_{D} of a few kV is applied. If a single ion, or a single electron, or a photon, hits the wall inside of the channel, usually a few secondary electrons are produced. These secondary electrons are then accelerated until they hit the channel wall, where each of these electrons produces again several secondary electrons. The repetition of this process results in an electron avalanche leaving the channel, caused by only one input ion, electron or photon. The gain of an electron multiplier tube is typically in the range of 10^4 to 10^7 [Wiz79; Ham13].

[12] BEHLKE HTS 61-03-GSM

As mentioned in section 4.1 the channeltron used in this thesis comprises only six of these electron multiplier tubes. It is therefore well suited for the detection of a single ion or a few ions. The six tubes have a diameter of a few mm and are twisted around a solid center (see figure 5.8c) to reduce the ion feedback [PHO09]. Conversely, in the microchannel plates of our MCP detector 8×10^6 microchannel electron multipliers with a diameter of 4 µm are arranged parallel to each other [Ham13], which allows for the detection of many ions that hit the detector at the same time. Figure 5.8b schematically shows the structure of such a microchannel plate. As mentioned in section 4.3 the MCP detector used in this thesis comprises two stacked microchannel plates to prevent ions passing through the detector without hitting a microchannel wall (see also figure 5.9). The gain for our channeltron is specified to be 5×10^7 [PHO09], and 1×10^6 [Ham08] for our MCP detector.

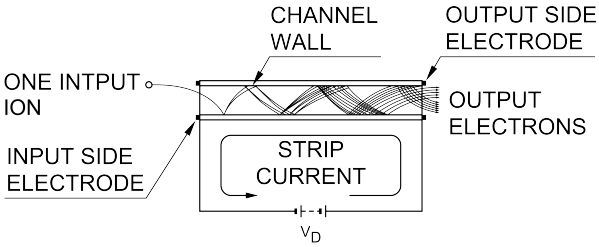

(a) Illustration of the working principle of an electron multiplier tube, taken from [Ham13], slightly modified.

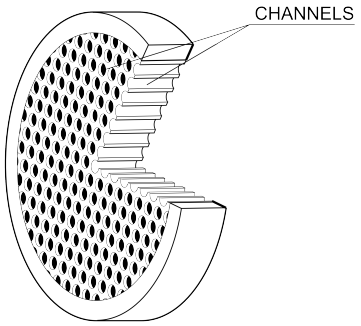

(b) Schematic structure of a microchannel plate, taken from [Ham13].

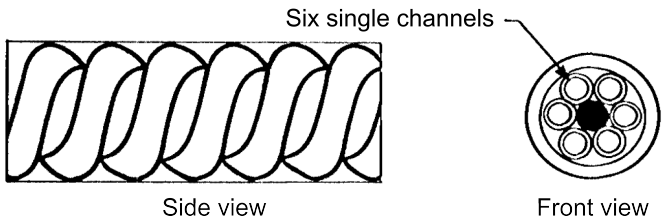

(c) Schematic structure of the channeltron with the six spiral electron multiplier channels, taken from [PHO09].

Figure 5.8: The basic component of the two ion detectors used in this thesis is an electron multiplier tube. Its working principle of creating a detectable signal from a single input ion is illustrated in (a). In our MCP detector 8×10^6 of these tubes with a diameter of 4 µm are arranged closely packed and parallel to one another in a plate, as is schematically illustrated in (b). The channeltron used in this thesis comprises six spiral electron multiplier channels with a diameter of a few mm, as is schematically shown in (c).

Figure 5.9 depicts the wiring circuit of the MCP detector. The frontplate is held at ground, the backplate at +2 kV and the anode at +2.5 kV. Therefore, the electron

avalanche leaving the backplate after an ion has hit the frontplate is guided to the anode. In order to limit the current flowing from the anode back to the microchannel plates a 1 MΩ resistance is used. The electrode labeled substrate in figure 5.9 is referred to as MCP detector baseplate in table B.1. The anode is AC-coupled to an amplifier with gain 11. Finally, the amplified signal is detected with a fast oscilloscope[13] which has a bandwidth of 1 GHz and a maximum sample rate of 10 GS/s. This bandwidth is required since the signal pulses of the MCP detector can have FWHM pulse widths of down to 500 ps [Ham08]. In order to reduce the ringing after the signal pulse to a minimum, the impedance of the transmission line from the anode to the input of the oscilloscope has to be matched to the impedance of the oscilloscope to avoid signal reflections. The wiring circuit of the channeltron is analogous to that of the MCP detector.

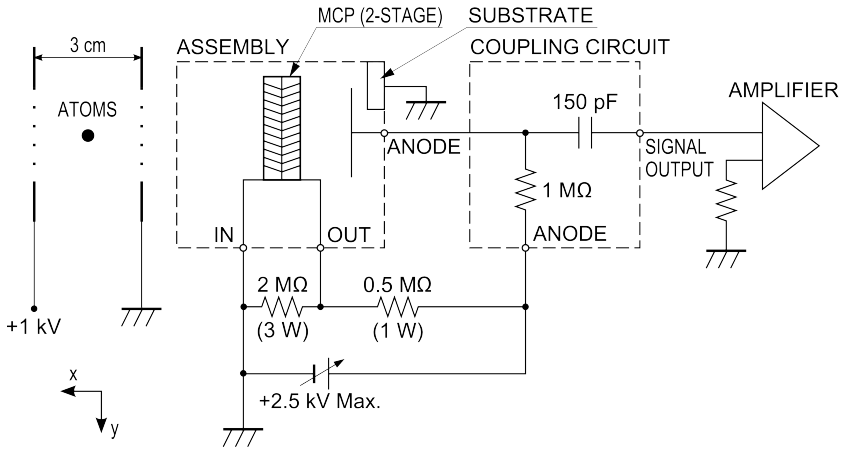

Figure 5.9: Wiring circuit of the 2-stage MCP detector used in this thesis, taken from [Ham13], slightly modified. The individual elements of the circuit diagram are described in the text. On the left side the atomic cloud and two electric field plates of the experiment cage (see chapter 4) are schematically drawn. When using the MCP detector to detect the Rydberg ions a high positive ionization voltage U_{ion} is applied to the electric field plate in front of the channeltron (the left plate) and the electric field plate in front of the MCP detector is held at ground. For the experiments done in the scope of this thesis normally an ionization voltage $U_{\text{ion}} \approx 1\,\text{kV}$ was used. The channeltron is wired in the same way as the MCP detector, only U_{ion} has to be applied to the electric field plate in front of the MCP detector.

Figure 5.10 displays typical Rydberg ion signals. They were taken from a Rb atom cloud of a few µK (see chapter 3), the atoms of which were photoexcited into the $40S_{1/2}$ Rydberg state (see section 5.1) and subsequently ionized. A signal trace recorded with the MCP detector using an ionization voltage of 1 kV is shown in figure 5.10a. Figure 5.10b depicts an ion signal of the channeltron, also recorded with $U_{\text{ion}} = 1\,\text{kV}$, and plotted with the same time scale as the MCP detector signal in figure 5.10a. A detailed view of

[13] LeCroy WaveRunner 610 Zi

the MCP detector ion signal shown in figure 5.10a is displayed in figure 5.10c. Finally, a saturated ion signal of the MCP detector, which was recorded with an ionization voltage of 3 kV, is shown in figure 5.10d, plotted with the same time scale as the ion signals in figure 5.10a and 5.10b, respectively. The channeltron ion signal in figure 5.10b nicely exemplifies the capability of the channeltron to resolve single ions. Comparison of the MCP detector ion signal in figure 5.10a to the channeltron ion signal in figure 5.10b shows that the MCP detector ion peaks are a little bit narrower than those of the channeltron. Fitting a Gauss function to the individual ion peaks yields pulse widths between 2 ns and 5 ns. For the channeltron there is practically no ringing after an ion event. The MCP detector signal shows a few oscillations after high ion pulses, but this ringing is damped very quickly (see figure 5.10c). The Rydberg ions hit the detectors in a time span of roughly 1 µs. The time spacing between the individual ion pulses varies from ionization pulse to ionization pulse. For example, in figure 5.10a three pulses lie close to each other, whereas in figure 5.10b the signal spikes are clearly separated from each other. Also the pulse height varies from pulse to pulse as can be seen in the signal traces displayed in figure 5.10. As mentioned above, it was calculated in [Tre12] that an ionization voltage of 400 V should be sufficient to ionize Rb Rydberg atoms in the $40S_{1/2}$ state. Therefore, it is surprising that increasing U_{ion} from 1 kV (figure 5.10b) to 3 kV (figure 5.10d) still increases the amplitude of the ion signal since already at $U_{\text{ion}} = 1\,\text{kV}$ all Rydberg ions should be ionized. The reason for this is subject of further investigations.

The dark count rate of the ion detectors has to be so small that the probability of a dark count happening during the detection time of Rydberg ions, which is roughly 1 µs (see figure 5.10), is negligible. A rough measurement yielded dark count rates of around $1\,\text{s}^{-1}$ for both ion detectors which is in accordance with the specified values [Ham08; PHO09]. Therefore, only every 10^6th signal pulse is a dark count and not due to a Rydberg ion.

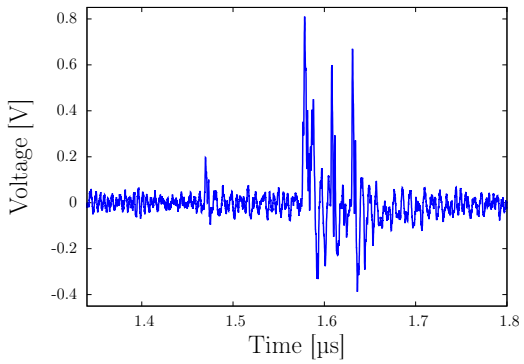

(a) Rydberg ion signal of the MCP detector recorded with an ionization voltage U_{ion} of 1 kV.

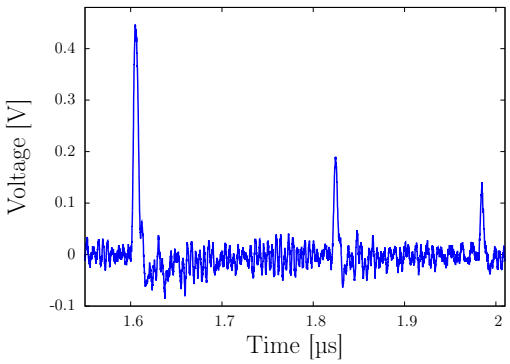

(b) Channeltron signal of single Rydberg ions recorded with $U_{\mathrm{ion}} = 1\,\mathrm{kV}$.

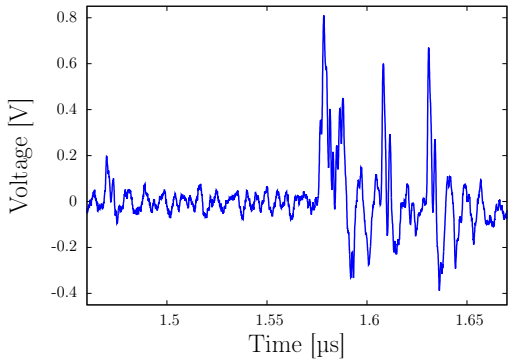

(c) Detailed view of the MCP detector ion signal shown in (a).

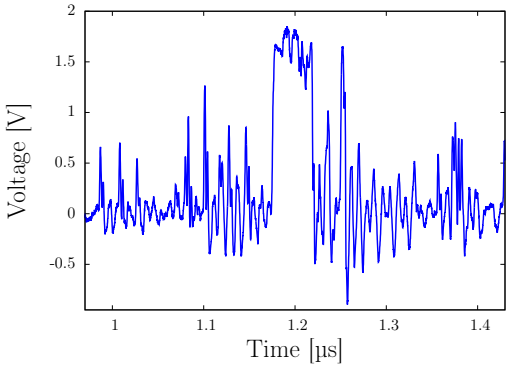

(d) Saturated Rydberg ion signal of the MCP detector with $U_{\mathrm{ion}} = 3\,\mathrm{kV}$.

Figure 5.10: Typical ion signals of the MCP detector in (a), (c) and (d) and of the channeltron in (b), taken from a Rb cloud within which Rydberg atoms were photoexcited. Each spike in the signal trace is caused by a Rydberg ion hitting the detector. Thereby, the number of photoexcited Rydberg atoms can be determined, provided that all Rydberg atoms are ionized by the electric field ionization pulse and hit the detector.

5.3. Rydberg spectrum of the ^{87}Rb 40S state

After the photoexcitation of Rydberg atoms was discussed in section 5.1 and the detection of Rydberg atoms was described in section 5.2, the recording of a spectrum of the ^{87}Rb $40S_{1/2}$ Rydberg state is reported in this section and an analysis of the spectrum is presented.

The typical experimental sequence used to measure a Rydberg spectrum is schematically illustrated in figure 5.11. The whole spectrum can be recorded using only one cold atom cloud as the sum of the 15 s evaporative cooling time and the 2 s recording time is still smaller than the 25 s lifetime of the atom cloud in the QUIC-trap (see section 3.3). Let us assume that for the recording of the first data point of the Rydberg spectrum the frequencies of the two excitation lasers are set to such a value that the two-photon detuning $\Delta_{2\gamma}$ is slightly negative, i. e. the sum of both laser frequencies f_1 is slightly less than the atomic resonance frequency between the ground state and the Rydberg state. The 1020 nm laser is constantly on since it does not couple the ground state Rb atoms to any other state. Conversely, the 420 nm is only switched on for typically $t_e = 10\,\mu s$. As soon as the 420 nm laser is switched on Rb atoms are excited from the ground state to the Rydberg state. Subsequently, the Rydberg atoms are ionized by a $t_{ion} = 50\,\mu s$ long electric field pulse (see section 5.2). For the recording of a Rydberg spectrum the waiting time t_w after the excitation pulse is set to zero, whereas for measurements of the Rydberg state lifetime, t_w is varied. The Rydberg ions arrive at the ion detector, either the MCP detector or the channeltron, distributed over a time span t_d of approximately 1 µs. They start to arrive roughly 1.5 µs after the ionization field was switched on as can be seen in figure 5.10 where the origin of the time axis coincides with the time the electric field is switched on. The pulse symbolizing the ion detection in figure 5.11 is plotted after the ionization pulse only for the sake of clarity. After the 420 nm excitation pulse the frequency of the 1020 nm laser is changed by the amount Δf with the help of an EOM (see reference [Tre12]). The second 420 nm excitation pulse starts 2 ms after the first one started. The Rydberg signal for the second frequency value $f_2 = f_1 + \Delta f$ is then measured in exactly the same way as the Rydberg signal for f_1. A whole Rydberg spectrum comprises 50 frequency points and it takes 100 ms to record the Rydberg signal for these 50 frequency values. To estimate the precision of the measured Rydberg signal, altogether 20 Rydberg spectra are recorded in one cloud where the frequency is ramped up for the first spectrum S_1, ramped down for the second spectrum S_2 etc. in order to avoid large frequency leaps of the 1020 nm laser.

Figure 5.12 displays two spectra of the ^{87}Rb $40S_{1/2}$ Rydberg state. Both spectra rely on the same measured values, only two different evaluation methods were applied to obtain the Rydberg signal out of the measured ion signal. In figure 5.12a the mean value of ion counts is plotted as function of the frequency. For each of the 50 frequency points f_i there are twenty signal traces of the ion detector. In each signal trace the number of spikes $N_{f_i,j}$, $i = 1, \ldots, N_f = 50$, $j = 1, \ldots, N_S = 20$, was counted as the number of excited Rydberg atoms (compare figure 5.10). Subsequently, the mean value $\overline{N}_{f_i} = \frac{1}{N_S} \sum_j N_{f_i,j}$ was calculated and plotted at the frequency value f_i. Besides, the error on the mean

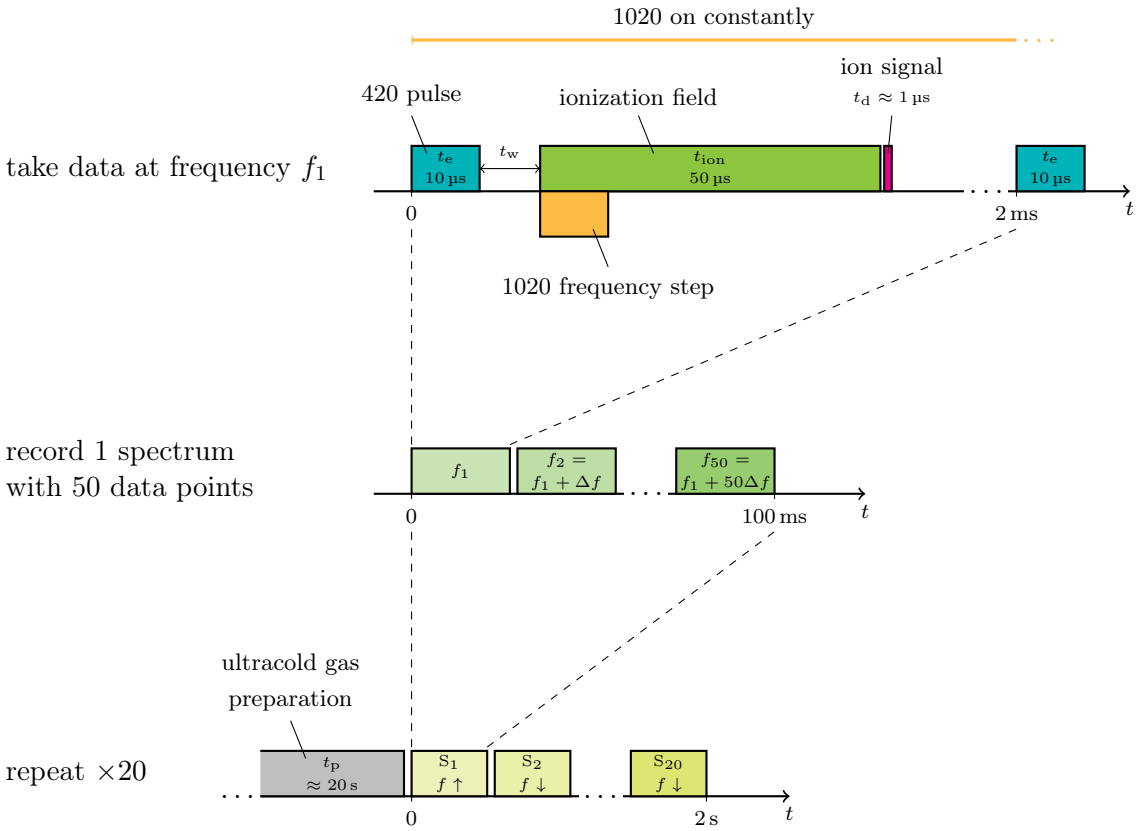

Figure 5.11: Schematic illustration of the experimental sequence which was used in this thesis to record a Rydberg spectrum. The excitation time is denoted t_e, t_w is an optional waiting time for lifetime measurements of the Rydberg state, t_{ion} is the length of the electric field ionization pulse and t_d is roughly the length of the ion pulse on the ion detector. The frequency f is ramped up for the first spectrum S_1, then ramped down for the second spectrum etc., where the frequency step size is denoted Δf. The sequence used to prepare the ultracold cloud (preparation time t_p) is depicted in figure 3.4.

$\alpha_{f_i} = \sqrt{\frac{1}{N_\mathrm{S}(N_\mathrm{S}-1)} \sum_{j=1}^{N_\mathrm{S}} (N_{f_i,j} - \overline{N}_{f_i})^2}$ [HH10] was determined and it is also displayed in figure 5.12a. In figure 5.12b the summed ion signal is shown as a function of the frequency. The summed ion signal for a given frequency value f_i was obtained by first taking the absolute value of each of the twenty signal traces, then calculating the area underneath the now only positive signal trace, and finally summing all these twenty areas up and dividing them by the number $N_\mathrm{S} = 20$ of signal traces.

For the Rydberg spectra shown in figure 5.12 the following measurement parameters were used. The temperature of the cold atom cloud was 15 µK. The frequency of the 420 nm laser was set to such a value that the intermediate state detuning Δ_i was $2\pi \times 80\,\mathrm{MHz}$ (see section 5.1.5). Calculation of the transition wavelength $\lambda_{6\mathrm{P}_{3/2}\to 40\mathrm{S}_{1/2}}$ from the $6\mathrm{P}_{3/2}$ intermediate state to the $40\mathrm{S}_{1/2}$ Rydberg state (hyperfine splitting is not included) with the energies of the involved levels taken from [San06] and [Mac11] respectively, yields a value of 1018.576 nm. The infrared laser driving this transition was set to this wavelength by measuring the wavelength of the laser with a wavemeter. Subsequently, the frequency of this laser was scanned in small steps around this wavelength $\lambda_{6\mathrm{P}_{3/2}\to 40\mathrm{S}_{1/2}}$ until the Rydberg state was found. The Rydberg spectra in figure 5.12 were recorded with a frequency scan range of 1.5 MHz and frequency steps $\Delta f = 30\,\mathrm{kHz}$. With the help of a $\lambda/4$-waveplate [Hec02] the polarization of the 420 nm laser was set to σ^+ and that of the 1020 nm laser to σ^- (see figure 5.3). The laser powers used for this specific measurement were $P_\mathrm{l} = 2\,\mathrm{mW}$ and $P_\mathrm{u} = 165\,\mathrm{mW}$. This yields the Rabi frequencies $\Omega_\mathrm{l} = 2\pi \times 1.700\,\mathrm{MHz}$, $\Omega_\mathrm{u} = 2\pi \times 12.375\,\mathrm{MHz}$ and $\Omega_{2\gamma} = 2\pi \times 131\,\mathrm{kHz}$, with the respective waists given in section 5.1.2. An ionization voltage U_ion of 1 kV was applied and the MCP detector was used to detect the Rydberg ions.

The number of ion counts in the spectrum displayed in figure 5.12a is unexpectedly low. The number N_r of Rydberg atoms in the cold cloud can be estimated using the Rydberg blockade volume $V_\mathrm{b} = \frac{4}{3}\pi r_\mathrm{b}^3$ with the blockade radius r_b [Hei08]. Only one Rydberg atom can be excited in the blockade volume V_b and the blockade radius is defined via $\frac{|C_6|}{r_\mathrm{b}^6} = \hbar\Omega_{2\gamma}$, where C_6 is the van der Waals coefficient [Hei08]. The calculation of this C_6 coefficient for the Rb $40\mathrm{S}_{1/2}$ state with a formula given in [Low12] yields $C_6 = -6.945 \times 10^{18}\,\mathrm{au} = -h \times 1001\,\mathrm{MHz\,\mu m^6}$. Using the two-photon Rabi frequency calculated above results in a blockade radius $r_\mathrm{b} = 4.4\,\mu\mathrm{m}$ and a blockade volume $V_\mathrm{b} = 367\,\mu\mathrm{m}^3$ for the $40\mathrm{S}_{1/2}$ Rydberg state. The volume V_c of the cigar-shaped atom cloud can be estimated by $V_\mathrm{c} = \frac{4}{3}\pi R_x R_y R_z$, where R_i, $i = x, y, z$, are the $1/e$-widths of the thermal atom cloud in the QUIC-trap, approximated as an harmonic trap with the trap frequencies ω_i (see section 3.3). With the trap frequencies of the QUIC-trap given in section 3.3, the temperature $T = 15\,\mu\mathrm{K}$ of the atom cloud mentioned above and the mass $m = 1.44 \times 10^{-25}\,\mathrm{kg}$ of ^{87}Rb [Ste10], the widths R_i can be calculated using $R_i = \frac{1}{\omega_i}\sqrt{\frac{2k_BT}{m}}$ [PS08], where k_B is the Boltzmann constant. Inserting the respective values yields $R_x = R_z = 40\,\mu\mathrm{m}$ and $R_y = 568\,\mu\mathrm{m}$, which results in a thermal cloud volume $V_\mathrm{c} = 3.8 \times 10^6\,\mu\mathrm{m}^3$. The number of excited Rydberg atoms in the cold cloud can therefore be estimated by $N_\mathrm{r} = \frac{V_\mathrm{c}}{V_\mathrm{b}} \approx 10^4$. Thus, the maximum number of approximately 4 ion counts in the Rydberg spectrum shown in figure 5.12a is surprisingly low. Simulations of the trajectories of the Rydberg ions after the ionization were carried out

in reference [Tre12] with the result that essentially all ions should hit the ion detector. These simulations were done under the assumption that the atom cloud sits at the center of the experiment cage. Since this does not necessarily have to be the case in the experiment, it was investigated if an additional electric field in the inside of the cage could guide the ions from their possibly off-center position to the ion detector. However, despite applying electric fields in all three spatial directions and scanning the electric field amplitude over a wide range for each direction, the number of ion counts could not be increased. Another reason for the small number of detected Rydberg ions may be the wire mesh over the aperture in the electric field plate in front of the MCP detector (see section 4.1). Possibly only a few Rydberg ions pass through this mesh.

The spectra in figure 5.12 were fitted with a pseudo-Voigt profile [Wer74]

$$V_{\mathrm{p}}(\nu) = a \cdot \left\{ \eta \cdot \frac{1}{1 + \left(\frac{\nu-\nu_0}{\frac{1}{2}\Delta\nu_{\mathrm{S}}}\right)^2} + (1-\eta) \cdot \exp\left[-\ln(2) \left(\frac{\nu-\nu_0}{\frac{1}{2}\Delta\nu_{\mathrm{S}}}\right)^2 \right] \right\} + o, \tag{5.23}$$

where $\Delta\nu_{\mathrm{S}}$ is the FWHM of the spectrum, ν_0 is the center frequency, a is the amplitude of the spectrum and o an offset. The pseudo-Voigt profile is an approximation of the Voigt profile which is a convolution of a Lorentz profile and a Gauss profile [Dem93]. The weighting factor $\eta \in [0, 1]$ provides information on the contribution of the Lorentz profile and the Gauss profile, respectively, to the pseudo-Voigt profile. The pseudo-Voigt profile is used to account for both homogeneous and inhomogeneous line broadening effects [Dem93]. The fit results are listed in table 5.3.

fit parameters	ion count spectrum	sum spectrum
FWHM $\Delta\nu_{\mathrm{S}}$ [kHz]	345 ± 46	259 ± 26
center frequency ν_0 [MHz]	176.133 ± 0.011	176.135 ± 0.007
weighting η	1.00	$0.90\,^{+0.10}_{-0.34}$
amplitude a [counts], [V µs]	2.91 ± 0.19	1.59 ± 0.11
offset o [counts], [V µs]	$0.05\,^{+0.12}_{-0.05}$	1.52 ± 0.05

Table 5.3: The results of the fitting parameters for the fit of the ion count spectrum (figure 5.12a) and the sum spectrum (figure 5.12b). A pseudo-Voigt profile (equation 5.23) was used as the fit function.

The fit result of the center frequency ν_0 was used as the origin of the frequency axis in the plots of figure 5.12. For the ion count spectrum the fit failed to deliver confidence bounds for the weighting factor η. For the sum spectrum the uncertainty of η is large. Besides, setting η to a fixed value between 0 and 1 different from the fit result, did not change the results of the other fit parameters considerably. Therefore, the fit results of the weighting factor η are not very indicative for the determination of the Lorentzian and Gaussian content of the spectral line.

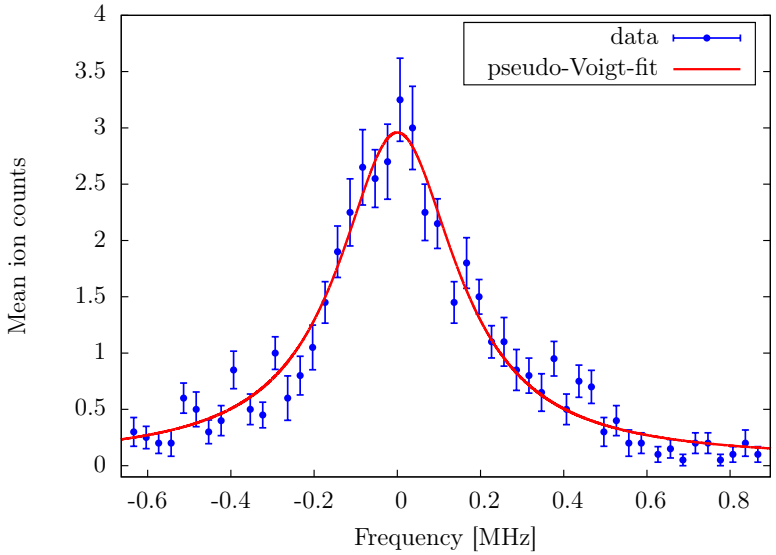

(a) Rydberg ion count spectrum of the $40S_{1/2}$ state.

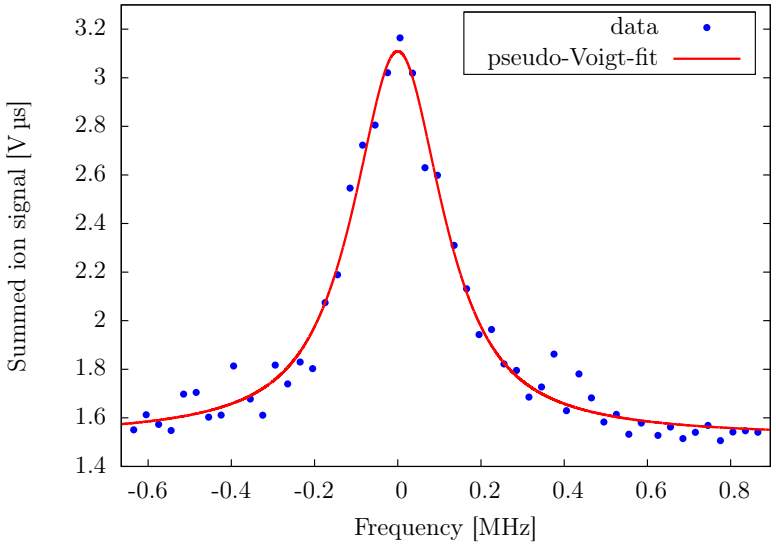

(b) Rydberg sum spectrum of the $40S_{1/2}$ state.

Figure 5.12: An ion count spectrum (a) and a sum spectrum (b) of the ^{87}Rb $40S_{1/2}$ Rydberg state. The evaluation methods applied to obtain the ion count and the sum Rydberg signal, respectively, out of the measured values are described in the text. The spectra were fitted with a pseudo-Voigt profile, given in equation 5.23. The results of the fit parameters are listed in table 5.3.

The fit result of the linewidth $\Delta\nu_S$ for the ion count spectrum is roughly 33 % larger than that for the sum spectrum. This is probably due to the fact that, if many ions hit the detector at almost the same time, the individual peaks in the signal trace are no longer resolvable (see figure 5.10d) and therefore the number of counted peaks is smaller than the number of ions actually arriving at the detector. Thus, the ion count signal saturates on resonance which results in a broader line of the ion count spectrum compared to the sum spectrum.

Several effects contribute to the observed linewidth $\Delta\nu_S \approx 260\,\text{kHz}$ of the sum spectrum. First, the line is homogeneously broadened due to the finite lifetime τ of Rydberg state [Dem93]. The natural linewidth $\Gamma = 2\pi \times 4.39\,\text{kHz}$ of the $40S_{1/2}$ Rydberg state (see section 5.1.2) accounts for this effect. Furthermore, the Doppler effect leads to an inhomogeneous broadening of the spectral line [Dem93]. The calculation of the Doppler width $\Delta\nu_D$ with equation 5.20 for a temperature $T = 15\,\mu\text{K}$ and counter-propagating excitation beams yields 121 kHz. In addition, power broadening, an homogeneous broadening effect, has to be taken into account [MS99]. The power broadened linewidth $\Gamma_p = \Gamma\sqrt{1+S_0}$, where Γ is the natural linewidth and $S_0 = 2\frac{\Omega_{2\gamma}^2}{\Gamma^2}$ is the resonant saturation parameter [MS99] with the two-photon Rabi frequency $\Omega_{2\gamma}$. Inserting the respective values yields a linewidth Γ_p of $2\pi \times 34\,\text{kHz}$ due to power broadening. Moreover, the finite interaction time between the Rydberg atoms and the pulsed 420 nm excitation laser also broadens the line due to the time-energy uncertainty [Sch07]. Using the time-bandwidth product $\Delta\nu_t \cdot t_e \approx 0.89$ for a rectangular pulse [Sch00] and inserting the length of the 420 nm laser excitation pulse $t_e = 10\,\mu\text{s}$ yields a linewidth $\Delta\nu_t$ of 89 kHz due to this effect. Finally, maybe the pickup of AC electric fields from the environment over the not properly shielded feedthrough pins of the feedthrough octagon (see figure B.2) caused an additional line broadening due to the AC Stark effect. The measured linewidth $\Delta\nu_S$ is a convolution of all these mentioned contributions.

The convolved linewidth $\Delta\nu_V$ taking into account the power broadened linewidth $\Delta\nu_p$ ($\Gamma_p = 2\pi \times \Delta\nu_p$), the Doppler width $\Delta\nu_D$, and the finite interaction time linewidth $\Delta\nu_t$ can be approximately calculated (the natural linewidth Γ is already taken into account by the power broadened linewidth $\Gamma_p = \Gamma\sqrt{1+S_0}$). Since power broadening is an homogeneous broadening effect the corresponding power spectral density $S_{L_p}(\nu)$ is a Lorentzian curve, whereas the power spectral density $S_{G_D}(\nu)$ for the Doppler broadened spectrum is a Gaussian curve as Doppler broadening is an inhomogeneous broadening effect [Dem93]. The spectrum broadened due to the finite interaction time between the Rydberg atoms and the rectangular 420 nm excitation pulse with length t_e has the following lineshape [Sch00]:

$$S_t(\nu) \propto \frac{\sin^2(\pi t_e \nu)}{(\pi\nu)^2}. \tag{5.24}$$

Since the convolution only reproduces Gaussian and Lorentzian curves whereas other lineshapes get distorted [Naz89], the power spectral density $S_t(\nu)$ has to be approximated with either a Gaussian curve $S_{G_t}(\nu)$ or a Lorentzian curve $S_{L_t}(\nu)$. As is shown in figure 5.13 $S_{G_t}(\nu)$ approximates $S_t(\nu)$ better than $S_{L_t}(\nu)$. Therefore the power spectral density $S_V(\nu)$ which takes into account the three mentioned contributions is approxi-

mately given by the following convolution:

$$\begin{aligned} S_{\mathrm{V}}(\nu) &= \left(S_{\mathrm{L_p}} * S_{\mathrm{G_D}} * S_{\mathrm{G_t}}\right)(\nu) \\ &= \left(S_{\mathrm{L_p}} * \left(S_{\mathrm{G_D}} * S_{\mathrm{G_t}}\right)\right)(\nu) \\ &= \left(S_{\mathrm{L_p}} * S_{\mathrm{G}}\right)(\nu), \end{aligned} \tag{5.25}$$

where the associativity of the convolution was used [MV99] and $S_{\mathrm{G}}(\nu) \equiv \left(S_{\mathrm{G_D}} * S_{\mathrm{G_t}}\right)(\nu)$ was introduced. The convolution $S_{\mathrm{G}}(\nu)$ of the two Gaussian curves $S_{\mathrm{G_D}}(\nu)$ and $S_{\mathrm{G_t}}(\nu)$ is again a Gaussian curve and has the linewidth [Bal09]

$$\Delta\nu_{\mathrm{G}} = \sqrt{\Delta\nu_{\mathrm{D}}^2 + \Delta\nu_{\mathrm{t}}^2}. \tag{5.26}$$

The convolution of a Lorentzian curve and a Gaussian curve is a Voigt profile for which the linewidth $\Delta\nu_{\mathrm{V}}$ is given by the modified Whiting approximation with a precision of 0.02 % [OL77]

$$\Delta\nu_{\mathrm{V}} = 0.5346\Delta\nu_{\mathrm{L}} + \sqrt{0.216\,597\,5\Delta\nu_{\mathrm{L}}^2 + \Delta\nu_{\mathrm{G}}^2}, \tag{5.27}$$

where $\Delta\nu_{\mathrm{L}}$ is the linewidth of the Lorentzian curve. Inserting $\Delta\nu_{\mathrm{D}} = 121\,\mathrm{kHz}$ and $\Delta\nu_{\mathrm{t}} = 89\,\mathrm{kHz}$ into equation 5.26 yields $\Delta\nu_{\mathrm{G}} = 150\,\mathrm{kHz}$. Inserting this value and $\Delta\nu_{\mathrm{L}} = \Delta\nu_{\mathrm{p}} = 34\,\mathrm{kHz}$ into equation 5.27 yields $\Delta\nu_{\mathrm{V}} = 169\,\mathrm{kHz}$. Thus, power broadening, Doppler broadening, and finite interaction time broadening contribute to 65 % to the observed linewidth $\Delta\nu_{\mathrm{S}} = 260\,\mathrm{kHz}$. The deviation may be explained by the mentioned additional line broadening due to the AC Stark effect.

Figure 5.14 displays a lifetime measurement for the ^{87}Rb $40\mathrm{S}_{1/2}$ Rydberg state. For this measurement, the waiting time t_{w} after the excitation pulse of the 420 nm pulse (see figure 5.11) was increased from 0 µs to 290 µs in steps of 10 µs. For each value of t_{w} the Rydberg sum spectrum was fitted as described above to get the amplitude $a_{\mathrm{sum}}(t_{\mathrm{w}})$ of the Rydberg signal on resonance as a function of the waiting time t_{w}. This amplitude decays exponentially with the $1/e$-lifetime τ_{exp}: $a_{\mathrm{sum}}(t_{\mathrm{w}}) = a_{\mathrm{sum},0} \cdot \mathrm{e}^{-\frac{t_{\mathrm{w}}}{\tau_{\mathrm{exp}}}}$. Therefore, $\ln(a_{\mathrm{sum}})$ is plotted in figure 5.14 as a function of t_{w} and a linear function is fitted to the measured values. The fit yields a lifetime $\tau_{\mathrm{exp}} = 67\,\mu\mathrm{s}$. This is almost twice the theoretical value $\tau \approx 36\,\mu\mathrm{s}$ (see section 5.1.2). The discrepancy is probably due to fact that no state-selective ionization was used. During the waiting time some Rydberg states nearby the target Rydberg state $40\mathrm{S}_{1/2}$ get populated because of black body radiation [Low12]. All these Rydberg states get ionized by the electric field pulse and therefore the detected ion signal is larger than it would be if only the target $40\mathrm{S}_{1/2}$ Rydberg state had been ionized. Thus, the extracted lifetime τ_{exp} is longer than the theoretically calculated value. An experimental confirmation of the calculated lifetime for our specific state via state-selective ionization has been reported in [Bra10].

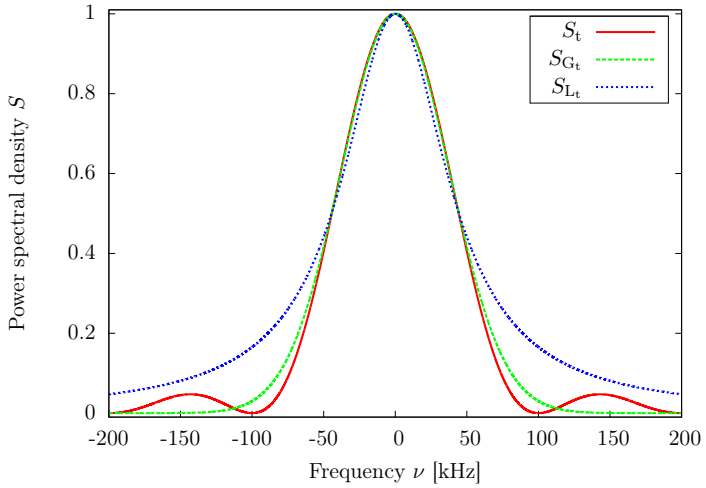

Figure 5.13: The power spectral density $S_t(\nu) = \frac{1}{t_e^2}\frac{\sin^2(\pi t_e \nu)}{(\pi\nu)^2}$ (compare equation 5.24) for the case of a finite interaction time between the Rydberg atoms and the $t_e = 10\,\mu s$ long rectangular excitation pulse. With the proportionality constant $\frac{1}{t_e^2}$, $S_t(\nu = 0) = 1$ (l'Hôpital's rule). $S_t(\nu)$ is compared to a Gaussian curve $S_{G_t}(\nu) = \exp\left\{-\ln 2\left(\frac{\nu}{\frac{1}{2}\Delta\nu_t}\right)^2\right\}$ and a Lorentzian curve $S_{L_t}(\nu) = \left\{1 + \left(\frac{\nu}{\frac{1}{2}\Delta\nu_t}\right)^2\right\}^{-1}$, where $\Delta\nu_t = \frac{0.89}{t_e} = 89\,kHz$ is the linewidth (FWHM) of the spectrum due to the finite interaction time.

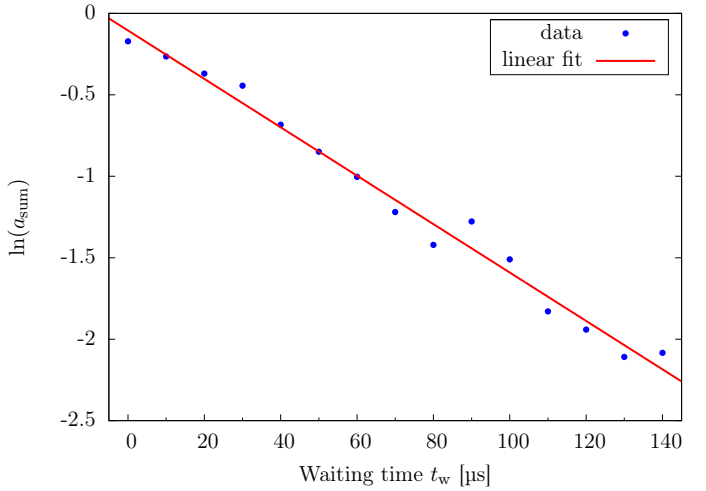

Figure 5.14: Lifetime measurement for the ^{87}Rb $40S_{1/2}$ Rydberg state. The natural logarithm $\ln(a_{sum})$ of the amplitude a_{sum} of the Rydberg sum spectrum is plotted as a function of the waiting time t_w after the excitation pulse of the 420 nm laser (see figure 5.11). A linear fit yields the $1/e$-lifetime $\tau_{exp} = 67\,\mu s$. The discrepancy to the theoretical value $\tau = 36\,\mu s$ is explained in the text.

5.4. Stark map of the ^{87}Rb 40S state

In this section the DC Stark effect, i. e. the effect of a DC external electric field $\mathcal{E}$ on the ^{87}Rb $40S_{1/2}$ Rydberg state is discussed. For small electric fields $\mathcal{E}$ this effect can be treated in a perturbation approach. The unperturbed atom is described by the stationary Schrödinger equation $\mathcal{H}^{(0)}|v^{(0)}\rangle = E_v^{(0)}|v^{(0)}\rangle$, where $\mathcal{H}^{(0)}$ is the Hamiltonian of the atom, and $|v^{(0)}\rangle$ an unperturbed eigenstate with eigenenergy $E_v^{(0)}$. Let us assume that a small constant electric field $\mathcal{E}$ is applied along the z-axis. This gives rise to a perturbation potential $\mathcal{V} = ez\mathcal{E}$ which has to be added to the unperturbed Hamiltonian $\mathcal{H}^{(0)}$. As the $40S_{1/2}$ state is a non-degenerate state, non-degenerate stationary perturbation theory [Sch07] can be applied to calculate the perturbed eigenenergy E_v

$$E_v = E_v^{(0)} + \langle v^{(0)}|\mathcal{V}|v^{(0)}\rangle + \sum_{w,w\neq v} \frac{|\langle w^{(0)}|\mathcal{V}|v^{(0)}\rangle|^2}{E_v^{(0)} - E_w^{(0)}} + \mathcal{O}(\mathcal{V}^3). \tag{5.28}$$

Since the $40S_{1/2}$ state is non-degenerate it has a distinct parity and therefore the first order energy correction $E^{(1)}_{|40S_{1/2}\rangle} = \langle 40S_{1/2}|\mathcal{V}|40S_{1/2}\rangle \propto \mathcal{E}$ vanishes. Thus, one expects a quadratic Stark effect

$$E_v = -\frac{1}{2}\alpha_{0,v} \cdot \mathcal{E}^2 \tag{5.29}$$

for the $|v\rangle = |40S_{1/2}\rangle$ state, where $\alpha_{0,v}$ is the scalar polarizability of the state $|v\rangle$ [OS85]. For Rb $|nS\rangle$ states, the scalar polarizability $\alpha_{0,|nS\rangle}$ was measured in reference [OS85] for $n = 15, 20, 25, \ldots, 80$, where the measured value for the $40S_{1/2}$ state was $\alpha_{0,|40S_{1/2}\rangle} = 10.57\,\mathrm{MHz/(V/cm)^2}$. A fit to all measured values yielded a dependance of the form $\alpha_{0,|nS\rangle} = 2.202 \times 10^{-9} \cdot (n^*)^6 + 5.53 \times 10^{-11} \cdot (n^*)^7$, $\alpha_{0,|nS\rangle}$ measured in $\mathrm{MHz/(V/cm)^2}$, where n^* is the effective principal quantum number (see equation 5.4) [OS85]. As the scalar polarizability of Rydberg atoms scales with $(n^*)^6$ and $(n^*)^7$, respectively, it is huge compared to the ground state scalar polarizability of $79.4\,\mathrm{mHz/(V/cm)^2}$ [Ste10] of ^{87}Rb. Due to their large polarizability Rydberg atoms are very susceptible to electric fields.

Figure 5.15a displays a measured Stark map of the ^{87}Rb $40S_{1/2}$ Rydberg state. The voltage U_{tb}, which was applied during the 420 nm excitation pulse between the top electric field plate and the bottom electric field plate of the experiment cage (see figure 4.1), is plotted on the horizontal axis. U_{tb} was varied from $-1\,\mathrm{V}$ to $+1\,\mathrm{V}$ in steps of $0.1\,\mathrm{V}$. For each value of U_{tb} a Rydberg sum spectrum was recorded (see section 5.3 and figure 5.12b). These spectra are plotted vertically at the respective U_{tb} values. The measured summed ion signal is illustrated by a color. The center frequency of the Rydberg spectrum at $U_{\mathrm{tb}} = 0\,\mathrm{V}$ is made the origin of the vertical frequency axis.

As expected, the Stark map in figure 5.15a shows a quadratic Stark shift of the $40S_{1/2}$ Rydberg level. In accordance with the positive value of $\alpha_{0,|40S_{1/2}\rangle}$ (see above) and the minus in equation 5.29, the Rydberg level is shifted to lower energies for an applied electric field. The electric field $\mathcal{E}$ in the inside of the experiment cage can be determined from the applied voltage U_{tb} by using the value of $\alpha_{0,|40S_{1/2}\rangle}$ cited above. For this purpose,

the fitted center frequencies from the Stark map in figure 5.15a are plotted as a function of U_{tb} in figure 5.15b. A quadratic function

$$E_{|40\mathrm{S}_{1/2}\rangle}(U_{\mathrm{tb}}) = -\frac{1}{2}\alpha_{0,|40\mathrm{S}_{1/2}\rangle} \cdot (a \cdot U_{\mathrm{tb}} + \mathcal{E}_{\mathrm{stray}})^2 \tag{5.30}$$

is fitted to this data where a is the factor to convert the voltage U_{tb} into an electric field, and $\mathcal{E}_{\mathrm{stray}}$ is a stray electric field inside the experiment cage, which is possibly present even if no voltage is applied to the electrodes. The fit results are listed in table 5.4. An applied voltage U_{tb} of 1 V between the top electric field plate and the bottom electric field plate of the experiment cage produces almost exactly an electric field $\mathcal{E}$ of 1 V/cm inside the experiment cage. Besides, there seems to be a small electric stray field inside the experiment cage. To record Rydberg spectra with zero electric field, a compensation voltage $U = -\frac{\mathcal{E}_{\mathrm{stray}}}{a}$ has to be applied. The value $a_{\mathrm{exp}} = 1.003\,\mathrm{cm}^{-1}$ for the conversion factor extracted from the measured Stark map displayed in figure 5.15a deviates by only 1.2 % from the value $a_{\mathrm{sim}} = 0.991\,\mathrm{cm}^{-1}$ extracted from simulations which were carried out in [Tre12].

fit parameters	fit results
conversion factor a [1/cm]	1.003 ± 0.002
electric stray field $\mathcal{E}_{\mathrm{stray}}$ [V/cm]	-0.013 ± 0.001
frequency offset ν_{o} [MHz]	177.359 ± 0.010

Table 5.4: The results of the quadratic fit of the Stark map shown in figure 5.15b, using the fit function given in equation 5.30. By means of the conversion factor a, the electric field $\mathcal{E}$ inside the experiment cage, which is produced by the voltage U_{tb} applied between the top and the bottom electric field plate of the cage, can be calculated. Besides the electric field produced by applying a voltage to the cage electrodes, there is also a small electric stray field $\mathcal{E}_{\mathrm{stray}}$ inside the experiment cage.

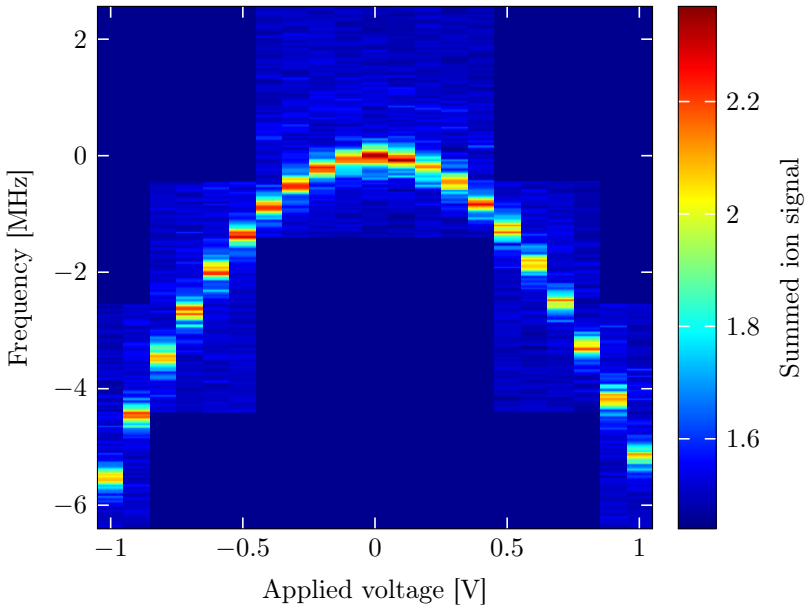

(a) Color plot of the Stark map. The frequency ranges for which no Rydberg ion signal was recorded are displayed in dark blue.

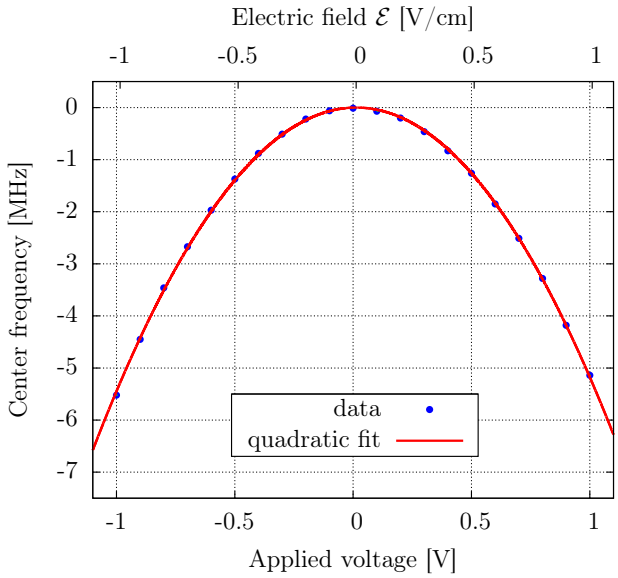

(b) The Stark map with an applied voltage axis and an electric field axis.

Figure 5.15: A measured Stark map of the ^{87}Rb $40S_{1/2}$ Rydberg state is shown in (a). It displays Rydberg sum spectra for different voltages applied between the top and bottom electric field plate of the experiment cage. In (b), only the center frequencies of these spectra are plotted as a function of the applied voltage. As is described in the text, the applied voltage can be converted to the electric field $\mathcal{E}$ inside the experiment cage.

6. Rydberg electron wavefunction imaging

6.1. Introduction

Based on L. de Broglie's concept of matter waves, E. Schrödinger introduced the theory of wave mechanics to describe the microscopic properties of matter [Sch26]. Within the framework of this theory the complex wavefunction ψ of a particle completely describes its state, and the spatial and temporal dependance of the wavefunction $\psi(\mathbf{r}, t)$ is governed by what we now call the Schrödinger equation. The square of the wavefunction $|\psi|^2$ is interpreted as the probability density distribution [Sch07], i. e. $|\psi(\mathbf{r}, t)|^2 \mathrm{d}V$ is the probability to measure the particle in the volume $\mathrm{d}V$ around the position $\mathbf{r}$ at the time t.

As the wavefunction of a particle contains all the information on the quantum mechanical state the particle is in, it is desirable to measure it, for example, by means of imaging it. In recent years, the stationary electronic wavefunction of various systems has been imaged. For bound electrons, the wavefunction of a certain state is commonly referred to as the electronic orbital of this state. A few electronic orbitals of several different molecules have been been imaged so far, using either scanning tunneling microscopy [Lem01; Rep05], high harmonic emission spectroscopy [Ita04] or photo-electron emission spectroscopy [Pus09; Hol10]. Usually the highest occupied molecular orbital (HOMO) was imaged and except from [Ita04] not the spatial structure of the actual wavefunction $\psi(\mathbf{r})$ was measured but the probability density distribution $|\psi(\mathbf{r})|^2$ (or its Fourier transform in momentum space [Pus09; Hol10]). Besides imaging molecular orbitals, the electron wavefunction in a quantum dot, an "artificial atom", has also been imaged by magneto-tunneling spectroscopy—the momentum space analog of the scanning tunneling microscopy [Vdo00]. Most recently, the wavefunction of Stark states in hydrogen Rydberg atoms was imaged using photoionization and an electrostatic magnifying lens [Sto13]. The listed experiments did not allow for the single shot imaging of the electronic orbital since they either used a tomographic imaging technique [Lem01; Rep05; Ita04; Pus09; Vdo00] or they needed a large number of photo-electrons for the formation of the electronic orbital image [Hol10; Sto13].

In reference [Bal13] there is a proposal to image the wavefunction of a Rydberg electron based on the coupling of the Rydberg electron to a Bose-Einstein condensate (BEC). As is shown in this reference, the sequential excitation of approximately 500 Rydberg atoms with a high principal quantum number ($n \in [110, 202]$) in a Bose-Einstein condensate resulted in a considerable loss of ground state condensate atoms after the BEC was allowed to expand freely for 50 ms. This loss was attributed to phonon and free particle excitations in the condensate, which would leave the condensate after some time of flight. The phonon and free particle excitations were explained by the interaction of the Rydberg electron with the up to 30 000 ground state condensate atoms located inside the orbit of the Rydberg electron due to its large radius $r \sim n^2 a_0$ [Gal94] of up to 4 µm, where a_0 denotes the Bohr radius. Since the interaction potential is proportional to the square $|\psi(\mathbf{r})|^2$ of the Rydberg electron wavefunction [Bal13], the coupling of the Rydberg

electron to the BEC provides the possibility to imprint the structure of $|\psi(\mathbf{r})|^2$ onto the density distribution $n(\mathbf{r})$ of the BEC. Therefore, by measuring the density distribution of the BEC, one could determine the probability density distribution of the Rydberg electron orbital. From here on determining the probability density distribution of the Rydberg electron orbital will be referred to as imaging the Rydberg electron orbital.

In order to illustrate the effect of the Rydberg excitations inside the BEC on the in-trap density distribution $n(\mathbf{r})$ of the condensate, simulations were carried out by Prof. Kazimierz Rzążewski and Prof. Mirosław Brewczyk from the Center for Theoretical Physics of the Polish Academy of Sciences, using the experimental parameters of [Bal13]. In figure 6.1a, the initial density distribution of the ^{87}Rb BEC is displayed before the first Rydberg excitation occurs (Ry = 0). The plots on the left side depict the z-integrated column density n^z_{col}, as a function of x and y in the form of a 2d density plot at the bottom, and as a function of either x (blue line) or y (green line) at the top. The y-integrated column density n^y_{col} is illustrated on the right side of figure 6.1a in analogous form. The spatial dimensions x, y and z are given in oscillator units $\overline{a} = \sqrt{\frac{\hbar}{m\overline{\omega}}}$, where m is the mass of the trapped atoms and $\overline{\omega} \equiv (\omega_x\omega_y\omega_z)^{1/3}$ the geometric mean of the trap frequencies for the three directions (see section 3.3).

Figure 6.1b shows the simulation results for 55 consecutive Rydberg excitations around the center of the BEC where the ^{87}Rb 110S Rydberg state was excited. For the simulations the time between two consecutive Rydberg excitations was set to 16 µs since this is the time used between two excitation pulses in the mentioned experiment [Bal13]. The black dot in the density plots marks the exact position where the Rydberg excitation occurred. For the simulations a small fluctuation of this position from shot to shot around the center of the BEC was taken into account. It is clear from the plots on the right side of figure 6.1b that the structure of the spherically symmetric [CB66] Rydberg S-state electron orbital is imprinted onto the column density n^y_{col}. In a disk around the center of the BEC with dimensions corresponding to the size of the Rydberg electron orbital the column density is reduced by roughly 35 % due to the interaction of the Rydberg electron with the ground state condensate atoms.

Further evidence that the proposed technique to image the Rydberg electron orbital via the electron's interaction with the BEC should work, is given by the simulation results displayed in figure 6.1c. The results for 55 consecutive Rydberg excitations into the $|160\text{D}, m_L = 0\rangle$ state are shown. As opposed to S-states, D-states, i. e. states with an orbital angular momentum $L = 2$, are not spherically symmetric but have two nodal planes [CB66]. As can be clearly seen from the density plot at the bottom right of figure 6.1c, the structure imprinted on n^y_{col} by the 160D, $m_L = 0$ Rydberg electrons is not spherically symmetric. Therefore, by imaging the density distribution of the BEC one could easily decide whether S- or D-Rydberg states have been excited in the BEC.

For the simulations neither the hyperfine structure basis $\{|F, m_F\rangle\}$, nor the fine structure basis $\{|J, m_J\rangle\}$, but the $\{|L, m_L, S, m_S\rangle\}$ basis was used to the describe the Rydberg state. This is due to the fact that in the mentioned experiment a high magnetic offset field $B_0 \approx 14\,\text{G}$ was used [Bal13]. Therefore, the energy splitting of the magnetic sublevels

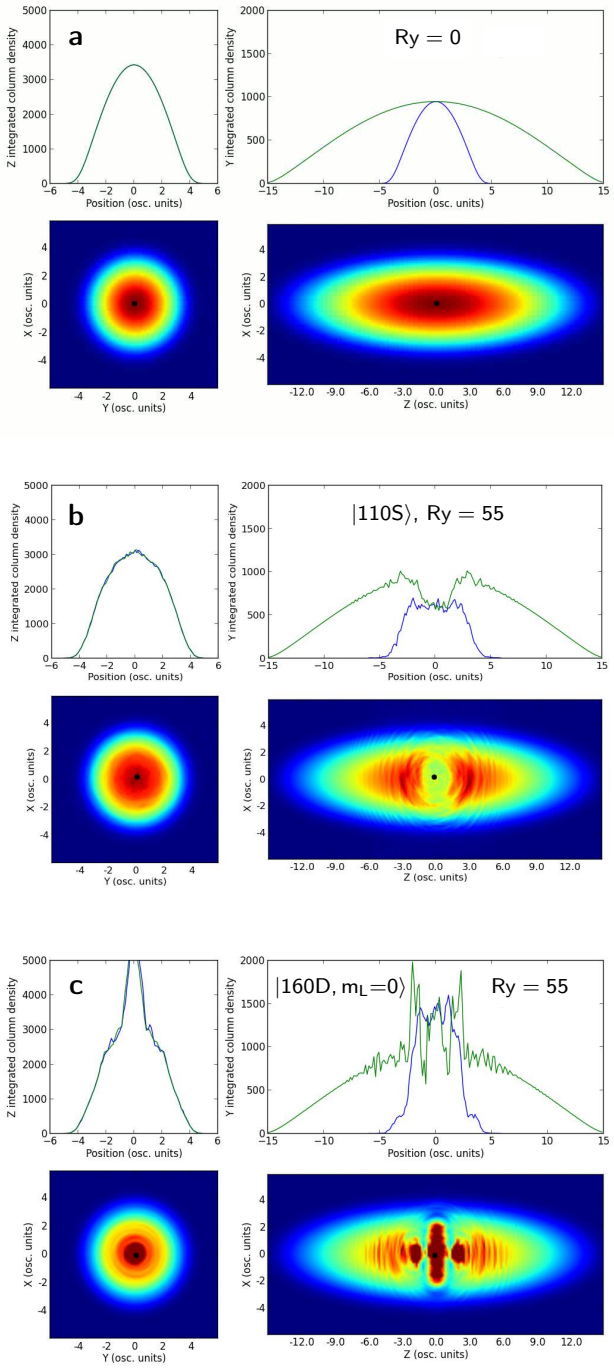

Figure 6.1: Simulations done by Prof. K. Rzążewski and Prof. M. Brewczyk which illustrate the imprint of the Rydberg electron orbital onto the density distribution of the BEC after several Rydberg excitations within the BEC. (a) depicts the initial density distribution of the BEC. In (b) the simulation results for the consecutive excitation of 55 Rydberg atoms in the 110S-state (spherically symmetric) are shown. (c) displays the results for the excitation of the $|160\mathrm{D}, m_L = 0\rangle$ Rydberg state (two nodal planes).

due to the magnetic field is much larger than the hyperfine structure splitting, and the fine structure splitting for the Rydberg state (compare section 5.1.2). Thus, the orbital angular momentum L and the spin S couple separately to the magnetic field (Paschen-Back effect [Sch07]), whereby $\{|L, m_L, S, m_S\rangle\}$ is the appropriate basis to describe the Rydberg state. In the experiment, the magnetic sublevel with $m_L = 0$ is excited by using σ^- light for the upper transition from the stretched intermediate state $5P_{3/2}$, $F = 3$, $m_F = 3$ ($m_L = 1$) [Bal13] to the Rydberg state.

The reason for displaying simulation results for the $n = 160$ D-state and not for the $n = 110$ D-state are the mentioned small excitation position fluctuations, which wash out the imprinted structure more, the larger the ratio of these fluctuations compared to the size of the Rydberg atom is. As the size of the Rydberg atoms increases quadratically with n but the size of the excitation position fluctuations stays constant, the imprinted structure is visible and pronounced better the larger the principal quantum number is.

Concerning the number of consecutive Rydberg excitations the simulations showed that it takes at least around Ry = 30 for the $|110S\rangle$ state and approximately Ry = 15 for the $|160D, m_L = 0\rangle$ state to clearly imprint the Rydberg electron orbital onto the density distribution of the BEC. After only Ry = 1 Rydberg excitation the change of the in trap BEC density distribution $n(\mathbf{r})$ is negligibly small for both considered Rydberg states. For 50 to 60 consecutive Rydberg excitations the imprint of the Rydberg electron orbital is the most pronounced and the sharpest. For much larger numbers of Rydberg excitations, Ry ≥ 100, the imprint of the Rydberg electron orbital gets blurred and washed out.

6.2. The phase contrast imaging technique

As is pointed out in section 6.1 imaging the Rydberg electron wavefunction can be transferred to imaging the in-trap column density of the BEC after several consecutive Rydberg excitations within the BEC. As will be shown below, absorption imaging, the usual technique for imaging BECs after some time of flight (compare figure 3.7a), is not applicable for in-trap imaging of BECs, however, a technique referred to as phase contrast imaging (PCI) can be employed for the measurement of in-trap density distributions of BECs. An expression for the phase contrast imaging intensity I_{PCI} which is the experimentally measured quantity will be deduced in this section.

A schematic illustration of the phase contrast imaging setup is shown in figure 6.2a. The ultracold atomic cloud, for which one wants to measure the density distribution $n(\mathbf{r})$, is illuminated by an imaging beam with a large diameter compared to the size of the cloud. The interaction between the imaging light and the atoms is described via the complex refractive index $n_{\mathrm{ref}}(\mathbf{r})$ of the atomic cloud. Treating the atoms in the cloud as an ensemble of two-level systems, and in the limit of a weak imaging beam (imaging beam intensity I_0 is low compared to the saturation intensity I_{sat} of the atomic transition), and within the rotating wave approximation, the complex refractive index reads [SZ08; KDS99]

$$n_{\mathrm{ref}}(\mathbf{r}) = 1 + n(\mathbf{r})\frac{\lambda\sigma_0}{4\pi}\left(\frac{i}{1+\left(2\frac{\Delta}{\Gamma}\right)^2} - \frac{2\frac{\Delta}{\Gamma}}{1+\left(2\frac{\Delta}{\Gamma}\right)^2}\right), \tag{6.1}$$

where λ denotes the wavelength of the imaging light, $\sigma_0 = \frac{3\lambda^2}{2\pi}$ the resonant scattering cross section, $\Delta \equiv \omega_\mathrm{L} - \omega_0$ the detuning between the laser frequency ω_L and the atomic resonance frequency ω_0, and Γ the natural linewidth of the atomic transition. If the incoming imaging light E_0 (electric field) is described as a plane wave propagating along the z-axis ($E_0 \propto \mathrm{e}^{ikz}$ with wavevector $k = \frac{\lambda}{2\pi}$), and if the thin lens approximation is applied to the atom cloud [KDS99], then the electric field E of the imaging light after passing the atomic cloud is given by

$$E = \exp\left(ik \int [n_\mathrm{ref}(\mathbf{r}) - 1]\mathrm{d}z\right) E_0 = t(x,y)\mathrm{e}^{i\phi(x,y)}E_0, \tag{6.2}$$

where the spatially dependent transmission coefficient $t(x,y)$ and the phase shift $\phi(x,y)$, that the imaging light gathers by propagating through the cloud, are introduced. Inserting the complex refractive index $n_\mathrm{ref}(\mathbf{r})$ from equation 6.1 into equation 6.2 yields the following expressions for the transmission coefficient and the phase shift:

$$t(x,y) = \mathrm{e}^{-D(x,y)/2}, \tag{6.3a}$$

$$\phi(x,y) = -\frac{\Delta}{\Gamma} D(x,y), \tag{6.3b}$$

using the spatially dependent optical density $D(x,y)$ of the cloud which is given by

$$D(x,y) = \frac{\sigma_0}{1 + \left(2\frac{\Delta}{\Gamma}\right)^2} \cdot n_\mathrm{col}(x,y), \tag{6.4}$$

where the column density of the atom cloud is defined as

$$n_\mathrm{col}(x,y) = \int n(\mathbf{r})\mathrm{d}z. \tag{6.5}$$

By means of absorption imaging, the optical density $D(x,y)$ is measured [KDS99], whereas phase contrast imaging makes use of the phase shift $\phi(x,y)$ introduced onto that part of the imaging light which propagates through the atom cloud (see below).

Absorption imaging of the in-trap density distribution of BECs with a high spatial resolution is problematic. For resonant imaging light the maximum resonant optical density $D_0 \equiv D(0,0)\big|_{\Delta=0} = \sigma_0 n_\mathrm{col}(0,0)$ (see equation 6.4) of the in-trap BEC is typically very high, for our experimental parameters $D_0 \approx 200$ (see section 6.3). However, the dynamic range of the CCD cameras normally used to record the absorption images typically corresponds to an optical density $D \leq 4$ [Wil11].

Thus, the in-trap BEC needs to be imaged with detuned imaging light. The highest contrast for absorption imaging is obtained with a detuning $\Delta = \frac{\Gamma}{2}\sqrt{D_0}$ [KDS99] for which the optical density D (see equation 6.4) is approximately 1 since $D_0 \approx 200 \gg 1$. For this detuning the phase shift $|\phi| \approx \frac{\sqrt{D_0}}{2}$ (see equation 6.3b), thus $|\phi| \approx 7 \gg \frac{\pi}{2}$ for $D_0 \approx 200$. Due to the non-zero detuning Δ the real component of the atomic susceptibility is finite (see equation 6.1), therefore the BEC atoms refract the imaging

light like a lens [KDS99]. The refraction angle β_{ref} for a phase shift $|\phi|$ can be estimated by $\beta_{\text{ref}} = \frac{|\phi|}{\frac{\pi}{2}}\beta_{\text{dif}}$, where $\beta_{\text{dif}} = \frac{\lambda}{d}$ is the diffraction angle of an object with diameter d imaged with light of a wavelength λ [KDS99]. For a diffraction limited imaging system the diffracted light from the smallest resolvable object just takes up the solid angle spanned by the imaging lens. For our experimental setup the smallest resolvable object at the center of the experiment cage has a diameter $d_{\text{min}} = 0.7\,\mu\text{m}$ for an imaging beam with $\lambda = 780\,\text{nm}$ (see section 4.1). Thus, for $|\phi| \approx 7$, hence $\beta_{\text{ref}} \approx 4.5\beta_{\text{dif}}$, the spatial resolution is reduced to $d \approx 4.5 d_{\text{min}} \approx 3.2\,\mu\text{m}$ since a portion of the refracted imaging light is not collected by the imaging lens. Therefore, the spatial resolution is not sufficient to image the 110S-Rydberg electron orbital with a diameter of $1.8\,\mu\text{m}$ (see section 6.3).

For a larger detuning $\Delta = \frac{\Gamma}{2}\frac{D_0}{\pi}$ with $|\phi| \approx \frac{\pi}{2}$ (see equation 6.3b) and thus $\beta_{\text{ref}} \approx \beta_{\text{dif}}$ the optical density drops to $D \approx \frac{\pi^2}{D_0}$ (see equation 6.4), hence $D \approx 0.05$ for $D_0 \approx 200$. Therefore, the absorption signal is far too small to be detected (compare figure 3.7a). However, a phase $|\phi|$ of $\frac{\pi}{2}$ still gives a considerable phase contrast signal (see figure 6.2b). From the dependencies $D \propto \frac{1}{\Delta^2}$ (see equation 6.4) and $\phi \propto \frac{1}{\Delta}$ (see equation 6.3b) it is also clear that for large detunings Δ still a detectable phase contrast signal is obtained whereas the absorption signal is to small to be measured.

To summarize, measuring the in-trap density distribution of BECs with a high spatial resolution is possible by using the phase contrast imaging technique with imaging light having a large detuning.

As is illustrated in figure 6.2a the electric field E of the imaging light after the atom cloud (see equation 6.2) can be decomposed into a scattered part E_{sc} and an unscattered part E_{usc}:

$$E = t\mathrm{e}^{i\phi}E_0 = E_{\text{sc}} + E_{\text{usc}}. \tag{6.6}$$

Solving equation 6.6 for E_{sc}, using that the unscattered light is equal to the incoming light ($E_{\text{usc}} = E_0$), yields

$$E_{\text{sc}} = (t\mathrm{e}^{i\phi} - 1)E_0. \tag{6.7}$$

As is depicted in figure 6.2a the scattered light gets collimated by the first lens whereas the unscattered light is focused. In the focal plane of the first lens a glass plate with a small dimple or a bump at the center, referred to as the phase plate, introduces a phase shift α on the focused unscattered light, i. e. $E_{\text{usc}} = E_0$ is transferred to $\mathrm{e}^{i\alpha}E_0$. To obtain a certain phase shift α the depth of the dimple or the height of the bump, respectively, has to be $s = \frac{\alpha}{2\pi}\frac{\lambda}{n_{\text{ref}}^{\text{pp}}-1}$, where $n_{\text{ref}}^{\text{pp}}$ is the refractive index of the phase plate.

A second lens collimates the unscattered light, after it was phase-shifted by α, and focuses the scattered light (see figure 6.2a). In the imaging plane the interference between the scattered light and unscattered light transforms the phase shift ϕ imprinted on the scattered light by the atom cloud into a detectable intensity signal I_{PCI}. The electric field in the imaging plane is given by $(t\mathrm{e}^{i\phi} - 1)E_0 + \mathrm{e}^{i\alpha}E_0$, and with the intensity being proportional to the squared modulus of the electric field [Hec02], the phase contrast imaging intensity signal I_{PCI} reads

$$I_{\text{PCI}} = I_0|t\mathrm{e}^{i\phi} - 1 + \mathrm{e}^{i\alpha}|^2, \tag{6.8}$$

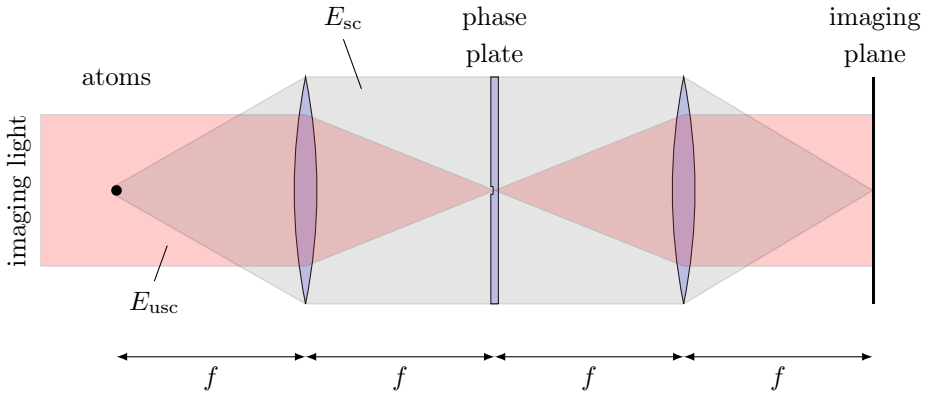

(a) Schematic illustration of the phase contrast imaging setup.

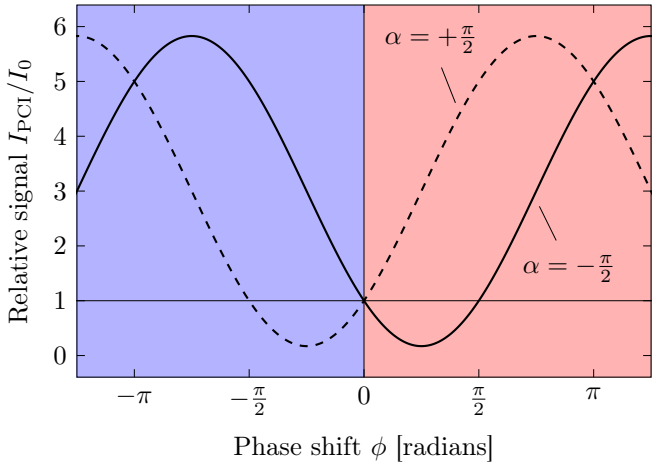

(b) Relative phase contrast imaging signal I_{PCI}/I_0 as a function of the phase shift ϕ.

Figure 6.2: The setup for phase contrast imaging is schematically illustrated in (a). After passing the atom cloud, the imaging light can be decomposed in a scattered part (gray) and an unscattered part (red), where the atom cloud imprinted a phase shift ϕ onto the scattered light. A phase plate in the focal plane of the first lens introduces a phase shift α on the unscattered light. By interference of the scattered and unscattered light the phase shift ϕ is converted into a detectable intensity signal I_{PCI} in the imaging plane. In subfigure (b), the relative signal I_{PCI}/I_0 is plotted as a function of ϕ for $\alpha = \pm\frac{\pi}{2}$ and $t = 1$ (see equation 6.9). The graph illustrates that $\frac{I_{\mathrm{PCI}}}{I_0}(\phi)$ is a periodic function with a dynamic range of approximately 6. The phase shift ϕ (see equation 6.3b) is negative for a blue detuned imaging beam ($\Delta > 0$, blue shaded area) and positive for red detuning ($\Delta < 0$, red shaded area).

where $I_0 \propto |E_0|^2$ denotes the intensity of the incoming imaging beam.

For $\alpha = \pm\frac{\pi}{2}$ ("+" for a bump, "−" for a dimple), equation 6.8 transforms to

$$I_{\mathrm{PCI}} = I_0 \left(t^2 + 2 - 2\sqrt{2} \cdot t \cos\left\{ \phi \pm \frac{\pi}{4} \right\} \right). \tag{6.9}$$

Choosing $\alpha = \pm\frac{\pi}{2}$ is favorable since in these cases the dependance between I_{PCI} and the phase shift ϕ is linear for small ϕ (see below). The phase contrast imaging signal is a periodic function of the phase shift ϕ, as is illustrated in figure 6.2b. The dynamic range of the phase contrast imaging signal calculates to $4\sqrt{2} \approx 6$ for $t = 1$.

For large detunings Δ, the optical density D is small (equation 6.4), thus the phase shift is also small (equation 6.3b) and the transmission coefficient t is approximately 1 (equation 6.3a), reducing the phase contrast imaging signal of equation 6.9 to

$$I_{\mathrm{PCI}} \approx I_0(1 \pm 2\phi). \tag{6.10}$$

Therefore, for large detunings, I_{PCI} is proportional to the phase shift ϕ and thereby proportional to the column density n_{col} of the atom cloud which is the quantity one wants to determine via the phase contrast imaging.

6.3. Simulation of the phase contrast imaging signal

In order to find out if the Rydberg electron orbital can be imaged via phase contrast imaging for our experimental parameters simulations of the phase contrast imaging signal were carried out.

First, the in-trap density distribution $n(\mathbf{r})$ of a BEC which we typically produce with our setup (see section 3.3) was calculated using the Thomas-Fermi approximation [PS08]

$$n(\mathbf{r}) = \frac{\mu - V(\mathbf{r})}{U_0}, \tag{6.11}$$

where μ is the chemical potential of the BEC given by equation 3.2,

$$V(\mathbf{r}) = \frac{1}{2} m(\omega_x^2 x^2 + \omega_y^2 y^2 + \omega_z^2 z^2) \tag{6.12}$$

is the harmonic trapping potential with the mass m of the trapped atoms and the trap frequencies ω_i $(i = x, y, z)$, and

$$U_0 = \frac{4\pi\hbar^2 a}{m} \tag{6.13}$$

denotes the effective interaction strength (unit $\mathrm{J/m^3}$) between two particles with a being the scattering length [PS08]. Inserting the values for the ^{87}Rb mass m [Ste10], our trap frequencies $\omega_x = \omega_z = 2\pi \times 214\,\mathrm{Hz}$ and $\omega_y = 2\pi \times 15\,\mathrm{Hz}$, and our typical condensate atom number $N = 10^5$, as well as the scattering length $a = 5.45\,\mathrm{nm}$ (see section 3.3) yields a very elongated cigar-shaped density distribution $n(\mathbf{r})$ of the BEC (see figure 6.4a). The Thomas-Fermi radii are $R_x^{\mathrm{TF}} = R_z^{\mathrm{TF}} = 2.8\,\mu\mathrm{m}$ and $R_y^{\mathrm{TF}} = 40\,\mu\mathrm{m}$ (see section 3.3), thus the BEC has a large aspect ratio of approximately 14. The peak density $n(\mathbf{r} = 0)$ calculates to $1.9 \times 10^{14}\,\mathrm{cm^{-3}}$. The density distribution is normalized with $\int n(\mathbf{r})\mathrm{d}V = N$.

In a second step the z-integrated column density

$$n^z_{\mathrm{col}}(x,y) = \int_{z_-(x,y)}^{z_+(x,y)} n(\mathbf{r})\mathrm{d}z \tag{6.14}$$

was calculated from the density distribution of the BEC (see equation 6.5) with the lower and upper z-bound $z_\pm = \pm\sqrt{\frac{2}{m\omega_z^2}\left[\mu - \frac{1}{2}m(\omega_x^2x^2+\omega_y^2y^2)\right]}$, respectively. Calculation of the peak column density at the origin yields a value $n^z_{\mathrm{col}}(0,0) = 7.2\times10^{10}\,\mathrm{cm}^{-2}$. It should be noted that the z-direction in our setup (see figure 3.1) corresponds to the y-direction in the simulations displayed in figure 6.1.

As is described in section 6.1 and displayed in figure 6.1b, 55 consecutive Rydberg excitations into the 110S-state at the center of the BEC deplete the column density $n^z_{\mathrm{col}}(x,y)$ by approximately 35 % in an disk with radius $r_{|110\mathrm{S}\rangle}$, where $r_{|110\mathrm{S}\rangle}$ denotes the orbital radius of the 110S-state. The orbital radius of a Rydberg state with principal quantum number n is given by

$$r_{nlj} = \frac{1}{2}\left[3(n^*)^2 - l(l+1)\right]a_0, \tag{6.15}$$

where n^* denotes the effective principal quantum number (see equation 5.4), depending on n, the orbital angular momentum l, and the total angular momentum j via the quantum defect δ_{nlj} (see equation 5.3), and a_0 is the Bohr radius [Gal94]. Calculating the orbital radius $r_{|110\mathrm{S}\rangle}$ for the 110S-state, using the quantum defect constants δ_0 and δ_2 for ^{87}Rb Rydberg S-states given in table 5.1, yields a value of roughly 0.91 µm. Therefore, the z-integrated column density $n^z_{\mathrm{col,R}}(x,y)$ after the 55 Rydberg excitations is approximately given by

$$n^z_{\mathrm{col,R}}(x,y) = \begin{cases} 0.65\cdot n^z_{\mathrm{col}}(0,0), & \sqrt{x^2+y^2} \le r_{|110\mathrm{S}\rangle}, \\ n^z_{\mathrm{col}}(x,y), & \text{elsewhere.} \end{cases} \tag{6.16}$$

For the simulations of the phase contrast imaging signal, the ^{87}Rb atoms in the cold cloud were treated as two-level systems with ground state $5\mathrm{S}_{1/2}$, $F=2$, $m_F=2$ and excited state $5\mathrm{P}_{3/2}$, $F'=3$, $m_{F'}=3$, inducing a phase shift on the σ^+-polarized imaging light which is detuned by Δ to the atomic resonance. The resonant scattering cross section σ_0 for the mentioned transition is roughly $2.9\times10^{-13}\,\mathrm{m}^2$ and the natural linewidth Γ amounts to approximately 6.1 MHz [Ste10]. The resonant optical density $D_0 = \sigma_0 n^z_{\mathrm{col}}(0,0)$ of the BEC thus calculates to approximately 208.

The detuning Δ of the imaging beam needs to chosen carefully. If the imaging laser is operated too close to resonance then the phase shift ϕ imprinted on the beam by propagating through the atom cloud is so large that the range where the phase contrast imaging signal depends linearly on ϕ is left (see figure 6.2b). In figure 6.3a the phase shift ϕ^z gathered by an imaging beam propagating along the z-axis is plotted as a function of the detuning Δ. The plotted phase shift $\phi^z(\Delta)\big|_{x=y=0}$ was calculated for our experimental parameters at $x=y=0$, i. e. the cited values of σ_0 and Γ and the calculated column density $n^z_{\mathrm{col}}(0,0)$ from equation 6.14 were inserted into equation 6.4 to determine the

optical density, which was then inserted into equation 6.3b to evaluate the phase shift. For a phase plate with a dimple corresponding to a phase shift $\alpha = -\frac{\pi}{2}$, the phase contrast signal rolls over for a phase shift $\phi < -\frac{3\pi}{4}$, as can be seen from figure 6.2b. Therefore, as is illustrated in figure 6.3a, the imaging laser has to be blue detuned by more than approximately +125 MHz. For the performed simulations a blue detuning $\Delta = +200\,\text{MHz}$ was chosen (indicated by the vertical red line in figure 6.3a) to ensure that the phase contrast signal does not roll over.

For the case of not perfectly σ^+-polarized imaging light, the imaging beam needs to be blue detuned and not red detuned with respect to the $5S_{1/2}$, $F = 2 \rightarrow 5P_{3/2}$, $F' = 3$ transition since the $F' = 2$ and $F' = 1$ levels of the excited $5P_{3/2}$ state are 267 MHz and 424 MHz red detuned from the $F' = 3$ level, respectively (see figure 3.2). If the imaging light was red detuned from the $5S_{1/2}$, $F = 2 \rightarrow 5P_{3/2}$, $F' = 3$ transition, it would be close to resonance with the transitions to the $F' = 2$ and $F' = 1$ levels, thus the phase contrast signal would not depend linearly on ϕ, as discussed above. For our simulations the hyperfine levels $F' = 2$ and $F' = 1$ of the excited state were not taken into consideration, consequently there is no resonance dispersion signal at $\Delta = -267\,\text{MHz}$ in the $\phi^z(\Delta)$-plot in figure 6.3a.

For a blue detuned imaging beam it is favorable to choose a dimple generating a phase shift α of $-\frac{\pi}{2}$ instead of a bump producing a phase shift $\alpha = +\frac{\pi}{2}$, since, as can be seen from figure 6.2b, the phase contrast signal for $\alpha = +\frac{\pi}{2}$ rolls over already for $\phi < -\frac{\pi}{4}$. In contrast, for $\alpha = -\frac{\pi}{2}$ the range where the phase contrast signal depends linearly on ϕ extends to approximately $-\frac{\pi}{2}$ and the phase contrast signal rolls over only for $\phi < -\frac{3\pi}{4}$, as already mentioned.

The effect of the large phase shifts ϕ near resonance on the phase contrast imaging signal is illustrated in figure 6.3b. In this figure the relative z-integrated phase contrast intensity $\frac{I^z_{\text{PCI}}}{I_0}(\Delta)\big|_{x=y=0}$ is plotted as a function of the detuning Δ for $x = y = 0$. $\frac{I^z_{\text{PCI}}}{I_0}(\Delta)\big|_{x=y=0}$ was calculated by inserting our experimental parameters into equation 6.9. It can be seen in figure 6.3b that close to resonance, where the phase shifts ϕ exceed the mentioned linear range of the phase contrast imaging signal, the phase contrast imaging intensity starts to oscillate. For large red detunings the relative phase contrast intensity is smaller than 1 (see figure 6.3b), i. e. the phase contrast image of the atom cloud in the imaging plane is a dark spot compared to the background signal. In contrast, for large blue detunings the relative phase contrast signal is bigger than 1, resulting in the phase contrast image of the cloud being a bright spot compared to background signal.

Figure 6.3c exemplifies the effect of too small a detuning Δ on the phase contrast image of the BEC. Displayed is the relative z-integrated phase contrast imaging intensity $\frac{I^z_{\text{PCI}}}{I_0}(x, y)\big|_{\Delta=80\,\text{MHz}}$ as a function of x and y for a blue detuning Δ of only 80 MHz. As can be seen, the phase contrast imaging intensity at the center of the BEC, where the atom density is the highest, is lower than at the edge of the BEC, an effect referred to as phase wrapping.

Besides resulting in phase wrapping, too small a detuning Δ also leads to an unwanted heating of the condensate due to scattering of the imaging photons. The scattering rate

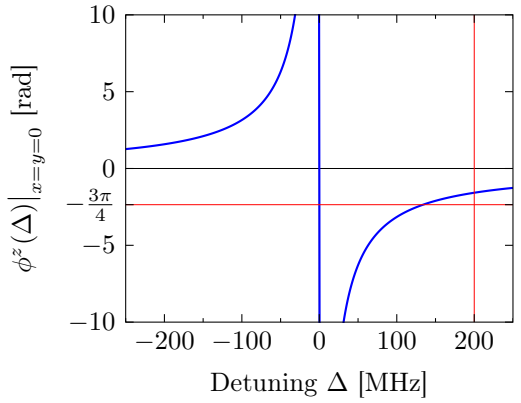

(a) z-integrated phase shift as a function of the detuning Δ for $x = y = 0$.

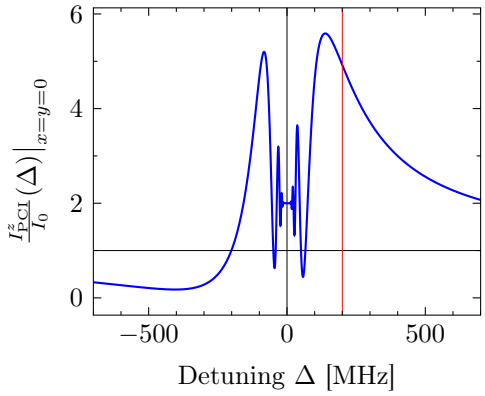

(b) Relative z-integrated phase contrast imaging intensity as a function of the detuning Δ for $x = y = 0$.

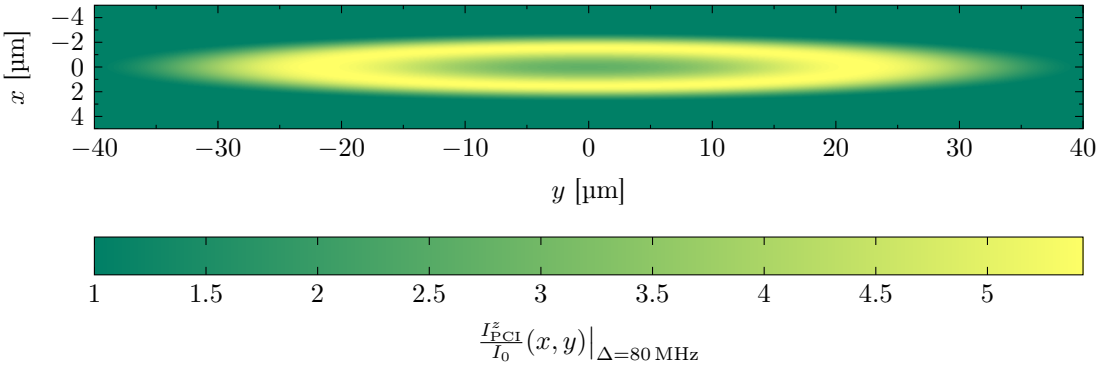

(c) Relative z-integrated phase contrast imaging intensity as a function of x and y for a detuning $\Delta = 80\,\mathrm{MHz}$. The x-axis and the y-axis have the same scale.

Figure 6.3: Graphs which illustrate that it is important to choose an appropriate detuning Δ for the phase contrast imaging light. The detuning must not be to small since for the resulting large phase shifts ϕ (a) the phase contrast imaging signal rolls over (see figure 6.2b). This results in oscillations of the phase contrast imaging intensity for small detunings, as is shown in (b). Besides, for too small a detuning, phase wrapping occurs in the phase contrast image of the condensate, displayed in (c). For our simulations a detuning of $+200\,\mathrm{MHz}$ was chosen.

R_{sc}, for the imaging beam having a detuning Δ and an intensity I_0, is given by

$$R_{\mathrm{sc}} = \left(\frac{\Gamma}{2}\right) \frac{\frac{I_0}{I_{\mathrm{sat}}}}{1 + \left(2\frac{\Delta}{\Gamma}\right)^2 + \frac{I_0}{I_{\mathrm{sat}}}}, \tag{6.17}$$

where Γ is the natural linewidth and I_{sat} the saturation intensity of the atomic transition the imaging photons are scattered from [Ste10]. Since $R_{\mathrm{sc}} \propto \frac{1}{\Delta^2}$, it is beneficial to have a large detuning. The saturation intensity for the ^{87}Rb transition under consideration, the transition from $5S_{1/2}$, $F = 2$, $m_F = 2$ to $5P_{3/2}$, $F' = 3$, $m_{F'} = 3$, is approximately $3.6\,\mathrm{mW/cm^2}$ [Ste10]. Calculating the scattering rate for an intensity ratio $I_0/I_{\mathrm{sat}} = 0.5$ and the detuning $\Delta = 200\,\mathrm{MHz}$ used for our simulations yields roughly 350 Hz. For this calculation I_0 was chosen to be only half the value of I_{sat} since the formula for the refractive index $n_{\mathrm{ref}}(\mathbf{r})$ given in equation 6.1 only holds in the limit of a weak imaging beam. Given an imaging pulse with length $t_{\mathrm{p}} = 50\,\mu\mathrm{s}$, one atom scatters on average $R_{\mathrm{sc}} \cdot t_{\mathrm{p}} = 0.0175$ photons during the imaging process. As each scattered photon transfers a momentum $p = \hbar k = \frac{h}{\lambda}$ to the atom (k is the wavevector, λ the wavelength of the imaging light), the atoms' temperature T increases by approximately $\frac{p^2}{2mk_{\mathrm{B}}} = 0.1\,\mathrm{nK}$ due to the scattering for a 200 MHz blue detuned imaging beam. This heating is small compared to the temperature of approximately 100 nK of the condensate (see section 3.3). Thus, the chosen detuning Δ of 200 MHz is large enough for the scattering induced heating to be negligible.

To summarize, a blue detuning $\Delta = +200\,\mathrm{MHz}$ for the phase contrast imaging light was found to be an appropriate choice in order to avoid phase wrapping and unwanted heating of the atom cloud. Additionally it was found that for blue detuned imaging light a dimple in the phase plate, producing a phase shift $\alpha = -\frac{\pi}{2}$, is preferable over a bump.

After having found appropriate parameters for the phase contrast imaging, the phase contrast imaging intensity of the BEC without Rydberg excitations (with $n^z_{\mathrm{col}}(x, y)$ given in equation 6.14), and the phase contrast imaging intensity of the BEC with the mentioned 55 consecutive Rydberg excitations into the 110S-state (with $n^z_{\mathrm{col,R}}(x, y)$ given in equation 6.16) was simulated using the cited imaging parameters. The simulation results are displayed in figure 6.4a, where the relative z-integrated phase contrast imaging intensity is plotted as a function of x and y for the BEC without Rydberg excitations (top) and with Rydberg excitations at the center of the BEC (bottom). In the lower phase contrast image a disk at the center with reduced phase contrast imaging intensity is clearly visible. As is shown in figure 6.4b, the relative z-integrated phase contrast imaging intensity is considerably reduced by approximately 26 % at the center of the BEC due to the Rydberg excitations. That the phase contrast imaging signal is not reduced by 35 % as is the column density (see section 6.1 and equation 6.16) is due to the fact that phase shifts ϕ in the range $-\frac{3\pi}{4}$ to $-\frac{\pi}{2}$ occurred for which the phase contrast imaging signal does not roll over yet, however, the range where the phase contrast imaging signal depends linearly on ϕ is already left, as can be seen in figure 6.2b.

Since the diameter of the disk with the reduced phase contrast imaging intensity is only approximately 1.8 µm for the 110S-Rydberg state (see equation 6.15), a large magnifica-

tion M has to be chosen for the phase contrast imaging beam. If, for example, the high sensitivity electron multiplying CCD camera "iXon Ultra 897" from Andor Technology with a pixel size of 16 µm [And13] is used to detect the phase contrast image of the BEC in the imaging plane, then a practicable magnification M of 30 would result in the disk being imaged on roughly $3.4 \times 3.4 \approx 12$ pixels, which would still allow for detecting the disk on the recorded image.

The number of arriving photons per pixel of the camera N_{pp} can also be calculated. Assuming an imaging beam with a wavelength $\lambda = 780.246\,\mathrm{nm}$ (see figure 3.2b), an intensity $I_0 = 1.8\,\mathrm{mW/cm^2}$ (see above), and a cross section $A_0 = \pi \cdot w^2 = \pi \cdot 1\,\mathrm{mm}^2$ (w is the waist of the beam), then a pulse of length $t_{\mathrm{p}} = 50\,\mu\mathrm{s}$ contains $N_{\mathrm{ph}} = \frac{I_0 A_0 t_{\mathrm{p}}}{h\frac{c}{\lambda}} \approx 1.1 \times 10^{10}$ photons, where h is the Planck constant and c is the speed of light. Given a magnification $M = 30$, the cross section A_{i} of the imaging beam in the imaging plane is $A_{\mathrm{i}} = \pi \cdot (Mw)^2 = \pi \cdot 30\,\mathrm{mm}^2$. The number of photons per area in the imaging plane is then given by $\frac{N_{\mathrm{ph}}}{A_{\mathrm{i}}}$. Thus, for one pixel of the camera having an area $A_{\mathrm{p}} = (16\,\mu\mathrm{m})^2$ (see above), the number of photons per pixel calculates to $N_{\mathrm{pp}} = N_{\mathrm{ph}} \cdot \frac{A_{\mathrm{p}}}{A_{\mathrm{i}}} \approx 996$. Hence, N_{pp} is much larger than the readout noise of the Andor iXon Ultra 897 camera. Without electron multiplication the readout noise of this camera is specified to be 98 electrons per pixel for a 17 MHz readout rate and the camera cooled to $-75\,^{\circ}\mathrm{C}$ [And13]. Therefore, assuming that each arriving photon produces one electron, the signal-to-noise ratio is approximately 10. Using the electron multiplication of the camera the readout noise is further reduced to less than 1 electron per pixel [And13], which is why single photon detection is feasible with this camera.

To summarize, based on our simulations, we conclude that using phase contrast imaging the structure of the Rydberg electron orbital can be imaged via its imprint onto the density distribution of the BEC after several Rydberg excitations in the BEC. This would introduce a new technique of imaging electronic wavefunctions, in addition to the already established tomographic and photo-electron emission techniques with the advantage that, once the Rydberg electron orbital is imprinted onto the BEC density distribution after several Rydberg excitations, it can be imaged in a single shot.

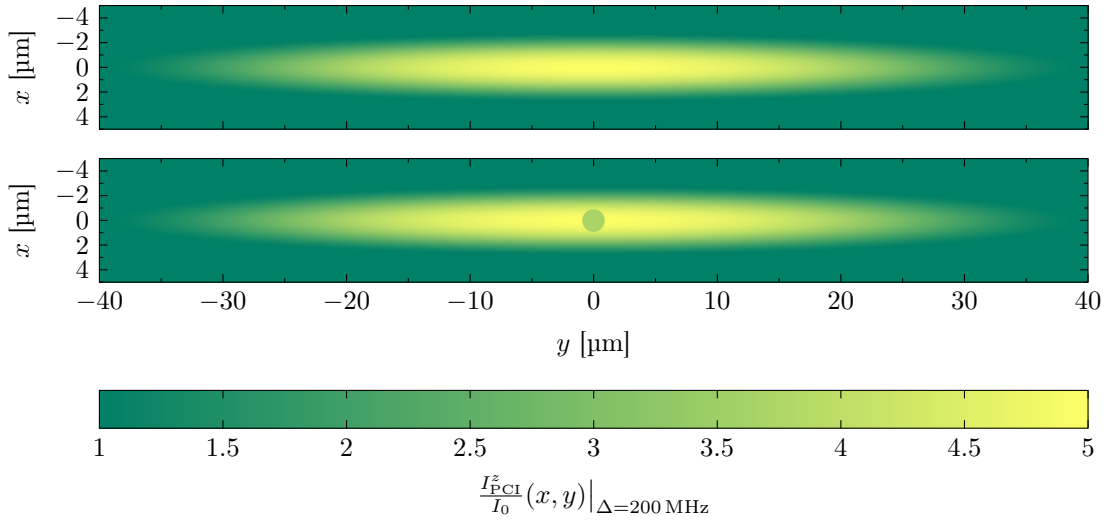

(a) Relative z-integrated phase contrast imaging intensity as a function of x and y for a detuning $\Delta = 200\,\mathrm{MHz}$, for the BEC without (upper density plot) and with (lower density plot) Rydberg excitations, respectively. The x-axis and the y-axis have the same scale.

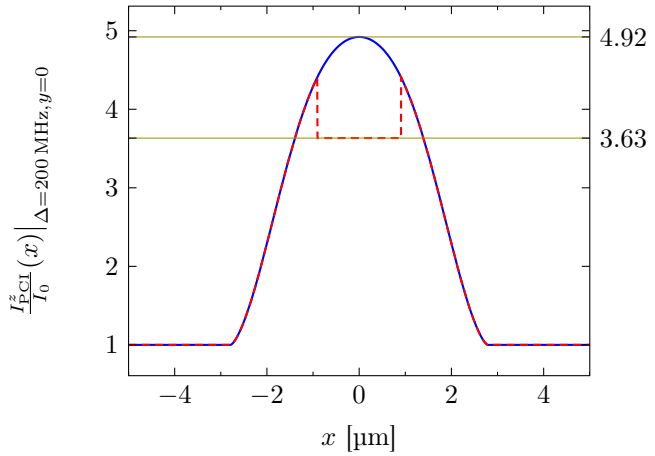

(b) Relative z-integrated phase contrast imaging intensity as a function of x for $y = 0$ and a detuning $\Delta = 200\,\mathrm{MHz}$. The blue solid line is a cut through the upper density plot and the red dashed line is a cut through the lower density plot of (a).

Figure 6.4: The upper density plot in (a) shows the simulated phase contrast image of an in-trap ^{87}Rb BEC for our experimental parameters (see section 3.3). The lower density plot in (a) displays the phase contrast image of this BEC after 55 consecutive Rydberg excitations into the 110S-state at the center of the BEC (see section 6.1). As can be seen, the imprint of the Rydberg electron orbital onto the density distribution of the BEC (see figure 6.1b) translates to a considerable reduction of the phase contrast imaging intensity in the region of the 110S Rydberg electron orbital. This significant reduction of the phase contrast imaging intensity amounts to approximately 26 %, as is shown in (b).

7. Summary and outlook

Summary In the scope of this thesis the highly precise excitation, manipulation and detection of ^{87}Rb Rydberg atoms in an ultracold gas was accomplished.

First, an experimental sequence with a cycle time of roughly 20 s for the production of an ultracold magnetically trapped spin-polarized sample of ^{87}Rb atoms in a glass cell at a pressure of approximately 2×10^{-11} mbar was successfully realized. At the beginning of this sequence the ^{87}Rb atoms were captured and cooled in a MOT, in a vacuum chamber at a pressure of approximately 8×10^{-9} mbar. After the MOT phase the temperature of the atoms was further reduced in an optical molasses. Then, the ^{87}Rb atoms were prepared in the low-field seeking $5S_{1/2}$, $F = 2$, $m_F = +2$ state via optical pumping. Subsequently, the atoms were magnetically transported from the MOT chamber to the glass cell where they were held in a QUIC-trap with a lifetime of the atomic cloud of roughly 25 s. The trapped atomic sample was then further cooled and made more dense by means of evaporative cooling. The Rydberg experiments reported on in this thesis were carried out with an ultracold, but still thermal, atomic sample with a temperature of a few µK, typically 5 µK, containing a few million atoms, usually around 4×10^6. Using the measured QUIC-trap frequencies $\omega_x = \omega_z = 2\pi \times 214$ Hz and $\omega_y = 2\pi \times 15$ Hz the in-trap size of this thermal cloud was calculated to be $R_x = R_z = 23$ µm and $R_y = 328$ µm, resulting in a peak density of 4.1×10^{12} cm^{-3}. The capability of the setup for the production of a Bose-Einstein condensate was also demonstrated, yielding a ^{87}Rb BEC with roughly 1×10^5 atoms at a temperature of 100 nK with an in-trap size of $R_x^{\mathrm{TF}} = R_z^{\mathrm{TF}} = 2.8$ µm and $R_y^{\mathrm{TF}} = 40$ µm, thus an aspect ratio of approximately 14, and a in-trap peak density of 1.9×10^{14} cm^{-3}.

Secondly, the experiment cage was assembled and inserted into the glass cell. With its six separately addressable electrodes the experiment cage allows for the precise manipulation of the electric field at the center of the cage, where the atomic sample is held in place by the QUIC-trap, and it enables the electric field ionization of the Rydberg atoms. There are two ion detectors mounted to the cage, a channeltron and an MCP detector, which facilitate single and multiple ion detection. The high NA aspheric lenses mounted in the top and bottom side of the experiment cage provide a high optical resolution of 0.7 µm at the center of the cage for light with a wavelength of 780 nm. For a pressure less than 2.2×10^{-7} mbar and up to an applied voltage of 2.5 kV we did not observe current breakthroughs between adjacent electrodes of the cage. With the experiment cage in the glass cell, the same pressure of 2×10^{-11} mbar as before the insertion was reached, thus the experiment cage did not deteriorate the required ultrahigh vacuum in the glass cell. With the assembly and insertion of the experiment cage, the set-up of the experimental apparatus, which was begun in May 2011 and mainly done during the master thesis of Christoph Tresp [Tre12], was completed and first Rydberg experiments could be carried out.

A two-photon excitation scheme, referred to as the inverted scheme, was used in the

scope of this thesis to excite spin-polarized ultracold ^{87}Rb atoms from the $5S_{1/2}$, $F = 2$, $m_F = +2$ state to a stretched $40S_{1/2}$ Rydberg state. A blue laser with σ^+ polarization operated at a wavelength $\lambda = 420.3\,\text{nm}$ close to the lower transition from the initial $5S_{1/2}$, $F = 2$, $m_F = +2$ state to the intermediate $6P_{3/2}$, $F = 3$, $m_F = 3$ state with a blue detuning $\Delta_\text{i} = 2\pi \times 80\,\text{MHz}$ to the intermediate state, corresponding to 56 times the natural linewidth of this state. Saturation spectroscopy was done in order to set the blue laser to such a frequency that the desired detuning Δ_i was obtained. An infrared laser at a wavelength $\lambda = 1018.576\,\text{nm}$ with σ^- polarization was used for the upper transition from the intermediate state into a stretched $40S_{1/2}$ Rydberg state. Both lasers were locked to an ultra-low expansion cavity using the Pound-Drever-Hall technique. This yielded laser linewidths of clearly less than 20 kHz. Thus, these laser linewidths are comparable to the natural linewidth of roughly 4.4 kHz of the ^{87}Rb $40S_{1/2}$ Rydberg state, hence allowing for high-resolution Rydberg spectroscopy. It was shown that for the chosen large detuning $\Delta_\text{i} = 2\pi \times 80\,\text{MHz}$ the intermediate state can be eliminated, resulting in an effective two-level system comprising only the ground state and the Rydberg state, which are coupled by the two light fields with an effective resonant two-photon Rabi frequency $\Omega_{2\gamma} = \frac{\Omega_\text{l}\Omega_\text{u}}{2\Delta_\text{i}}$, where Ω_l and Ω_u are the Rabi frequencies of the lower and upper transition, respectively. It was derived that for the mentioned transitions used in the scope of this thesis these Rabi frequencies can be calculated with $\Omega_\text{l} = \frac{\mathcal{E}_{0,\text{l}}}{\hbar}\frac{1}{2} \cdot 0.541 e a_0$ and $\Omega_\text{u} = \frac{\mathcal{E}_{0,\text{u}}}{\hbar}\sqrt{\frac{1}{3}} \cdot 8.438 e a_0 \left(n^*[40]\right)^{-1.5}$, respectively, where $\mathcal{E}_{0,i}$ $(i = \text{l}, \text{u})$ is the peak electric field of the respective laser beam and $n^*[40]$ is the effective principal quantum number of the ^{87}Rb $40S_{1/2}$ Rydberg state ($\hbar$ is the reduced Planck constant, e the elementary charge and a_0 the Bohr radius). A formula was given to calculate $\mathcal{E}_0$ for a Gaussian laser beam from its overall power P and its width w. Besides, a formula and required constants were given for the calculation of the effective principal quantum n^* for the ^{87}Rb $40S_{1/2}$ state. Using typically used values for P and w of the two Rydberg excitation beams, typical values for the one-photon Rabi frequencies and the two-photon Rabi frequency were calculated: $\Omega_\text{l} = 2\pi \times 380\,\text{kHz}$, $\Omega_\text{u} = 2\pi \times 13.279\,\text{MHz}$ and $\Omega_{2\gamma} = 2\pi \times 32\,\text{kHz}$.

For the detection of the photoexcited ^{87}Rb $40S_{1/2}$ Rydberg atoms, they were first ionized by an electric field pulse with an amplitude of roughly 1 kV (based on calculations carried out in [Tre12]), and with a length of 50 µs. The produced Rydberg ions were subsequently detected by one of the two mentioned ion detectors mounted to the experiment cage, either by the two-stage MCP detector (8×10^6 electron multiplier microchannels with 4 µm diameter; a specified gain of 1×10^6), or by the channeltron (6 electron multiplier channels with a diameter of a few mm; a specified gain of 5×10^7). The ion detector signal traces were recorded with a 1 GHz bandwidth oscilloscope, where care was taken to reduce the ringing after an ion signal pulse by means of impedance matching. The detector signal traces typically showed a few separated spikes with a width of a few ns, distributed over a time span of roughly 1 µs, each spike corresponding to a single detected ion. The dark count rate of both detectors was measured to be roughly $1\,\text{s}^{-1}$.

A 2 s long experimental sequence for recording a Rydberg spectrum with 50 frequency steps and 20 data points per frequency using only one cold atomic sample was successfully implemented. For this Rydberg spectrum sequence, the blue laser was pulsed with a

pulse duration of 10 µs and its frequency was held fixed, whereas the infrared laser was on constantly and its frequency was stepped to scan over the two-photon resonance of the Rydberg transition. The Rydberg signal was obtained out of the recorded ion detector signal traces either by counting the signal spikes (count signal) or by calculating the area underneath the signal traces (sum signal). An example of a recorded Rydberg spectrum of the ^{87}Rb $40S_{1/2}$ state was presented, which was measured in a thermal atomic sample of temperature $T = 15\,\mu K$ and with a two-photon Rabi frequency $\Omega_{2\gamma} = 2\pi \times 131\,kHz$. A pseudo-Voigt profile was fitted to the recorded count and sum spectrum in order to account for both homogeneous and inhomogeneous line broadening effects. The fitted FWHM linewidth $\Delta\nu_S$ of the sum spectrum was approximately 260 kHz. Several effects contributing to this linewidth were discussed: the 4.4 kHz natural linewidth of the $40S_{1/2}$ state, the Doppler broadening of 121 kHz for the mentioned temperature and counter-propagating excitation beams, the power broadening of 34 kHz for the cited two-photon Rabi frequency, and a frequency uncertainty of 89 kHz due to the finite interaction time between the 10 µs long rectangular excitation pulse of the blue laser and the Rydberg atoms. It was calculated that these effects result in a linewidth of approximately 169 kHz, thus 65 % of the fitted linewidth $\Delta\nu_S = 260\,kHz$. The deviation may be explained by an additional broadening due to the AC Stark effect as a result of AC electric field pickup from the environment over the feedthrough pins.

A measurement of the lifetime of the ^{87}Rb $40S_{1/2}$ state yielded $\tau_{exp} = 67\,\mu s$ and the deviation to the theoretically calculated value of 36 µs was thought to be due to the fact that for the measurement the Rydberg atoms were not ionized state-selectively.

It was discussed that Rydberg atoms are very susceptible to electric fields due to their large polarizability and that one expects a quadratic Stark shift of the Rydberg level to lower energies for the non-degenerate ^{87}Rb $40S_{1/2}$ state. This expectation was experimentally confirmed by recording a Stark map of the mentioned Rydberg state. On this behalf, the voltage U_{tb} between the top and the bottom electric field plate of the experiment cage was varied in steps in a certain range and for each value of U_{tb} a Rydberg spectrum was recorded. Using the value $\alpha_{0,|40S_{1/2}\rangle} = 10.57\,MHz/(V/cm)^2$ from [OS85] for the scalar polarizability of the Rydberg state, the factor $a = 1.003\,cm^{-1}$ to convert the voltage U_{tb} into the electric field inside the experiment cage was determined. Thus, a good agreement with the value $a = 0.991\,cm^{-1}$ extracted from simulations carried out in [Tre12] was found.

Finally, simulations were presented which were carried out in order to test if a technique proposed in [Bal13] to image the square of a Rydberg electron wavefunction is experimentally realizable. The proposed imaging technique is based on the strong interaction between a Rydberg electron within a BEC and the numerous ground state condensate atoms located inside the large Rydberg electron orbital. Simulations for the experimental parameters of [Bal13] were shown which illustrated that after several consecutive excitations of Rydberg atoms at the center of the BEC the structure of the Rydberg electron orbital was imprinted onto the in-trap density distribution of the BEC. In particular, for 55 consecutive Rydberg excitations into the spherically symmetric 110S-state it was

found that the column density of the BEC was reduced by roughly 35 % in a disk with dimensions corresponding to the size of the Rydberg electron orbital.

It was then discussed that phase contrast imaging would be a suitable technique to image the in-trap column density of the BEC and hence the imprinted Rydberg electron orbital. A formula for the phase contrast imaging intensity $I_{\mathrm{PCI}}(x, y)$ was derived and afterwards the phase contrast imaging signal was simulated for a ^{87}Rb BEC typically produced with our setup (trap frequencies, atom number) and with the imprinted 110S Rydberg electron orbital at the center. A blue detuning $\Delta = +200\,\mathrm{MHz}$ of the imaging light with respect to the ^{87}Rb imaging transition from $5\mathrm{S}_{1/2}$, $F = 2$, $m_F = 2$ to $5\mathrm{P}_{3/2}$, $F' = 3$, $m_{F'} = 3$ was found to be a suitable choice in order to avoid phase wrapping and heating of the condensate. Besides, it was found that for blue detuned imaging light a dimple in the phase plate imposing a phase shift $\alpha = -\frac{\pi}{2}$ on the unscattered light is preferable over a bump, with respect to the linear range of the phase contrast imaging signal. Using these imaging parameters, the simulated phase contrast image of the BEC with the imprinted 110S Rydberg electron orbital showed a measurable reduction of the phase contrast imaging signal of approximately 26 % in a disk at the center of the BEC. The diameter of this disk was given by the orbital diameter of roughly 1.8 µm of the 110S-state. Finally, it was pointed out that for a practicable imaging magnification, a suitable CCD camera, and an appropriate imaging pulse both the number of pixels the small disk would be imaged onto and the signal-to-noise ratio would be large enough to allow for the detection of the 110S Rydberg electron orbital imprinted onto the in-trap density distribution of the BEC.

Outlook Concerning the Rydberg spectroscopy, the experimental sequence to record a Rydberg spectrum in one cold atom cloud can be optimized. Since all Rydberg ions have arrived at the ion detector already approximately 4 µs after the start of the ionization pulse the 50 µs long electric field ionization pulse can be considerably shortened. Additionally, the 2 ms time span between two consecutive 420 nm excitation pulses can be shortened to the smallest possible value for which the frequency of the 1020 nm laser can still be changed without the laser falling out of lock. By this means, more data can be taken in the overall recording time of 2 s, therefore the error on the mean α_{f_i} for each frequency value f_i can be reduced.

The discrepancy between roughly 10^4 excited Rydberg atoms in a typical cold atomic cloud and only a few detected Rydberg ions needs to be investigated. Possibly the applied ionization voltage U_{ion} of 1 kV was not sufficient to ionize all $40\mathrm{S}_{1/2}$ Rydberg atoms in the atomic sample. The observation that with an increase of U_{ion} from 1 kV to 3 kV the ion detector could be saturated seems to suggest this. However, this rises the question if the calculation of the 400 V, which should be sufficient according to [Tre12] to ionize the 40S Rydberg state, is wrong or if the voltage which is applied to the feedthrough pins is not the voltage the Rydberg atoms inside the experiment cage are actually exposed to.

The proper shielding of the feedthrough pins of the feedthrough octagon may avoid the pickup of AC electric fields from the environment and thus may further reduce the linewidth of the recorded Rydberg spectra.

Concerning the phase contrast imaging, a phase plate with a dimple corresponding to a phase shift $\alpha = -\frac{\pi}{2}$ needs to be produced where the diameter of the dimple has to be chosen carefully since if it is too small only a part of the unscattered light propagates through it, however, if it is too large an unwanted phase shift α is imposed on a considerable amount of the scattered light (see figure 6.2a). Additionally, the surface roughness of the dimple has to be small in order to avoid distortions of the phase contrast image. The production of dimples with diameters of 50 µm and 170 µm via ion etching was reported in [Mep10] and [Wil11], respectively, with a surface roughness in the range of a few tens of nm.

Once the phase plate is produced, one could systematically take phase contrast images of the BEC with the imprinted Rydberg electron orbital for a series of different principal quantum numbers n of the Rydberg state in order to investigate how the size of the electron orbital changes with n. Additionally, the nodal structure of the Rydberg D-states may be imaged in comparison to the spherically symmetric structure of the Rydberg S-states.

A. Cleaning procedure for the ultrahigh vacuum

The following steps were applied to clean parts for the ultrahigh vacuum:

1. Ultrasonic bath in a degreaser solution for 30 min at a temperature of 50 °C.
2. Rinsing with distilled water.
3. Ultrasonic bath in acetone for 30 min at a temperature of 20 °C.
4. Rinsing with isopropanol.
5. Shaking off the isopropanol and letting the cleaned parts dry for 5 min.
6. Wrapping up the cleaned parts in aluminium foil for storage.

B. Pin assignment of the feedthrough octagon

The feedthrough octagon is a part of the vacuum chamber placed close to the glass cell (see figure 3.1), since the cables from the experiment cage, that stands inside the glass cell, are connected to the feedthroughs of this octagon. If you look in positive x-direction (see figure B.1), then the feedthroughs of the octagon are labeled A, B, ..., G counterclockwise starting at the bottom right. The pins of the 4-pin feedthroughs are numbered 1, 2, 3, 4 clockwise starting at the top (see figure B.2).

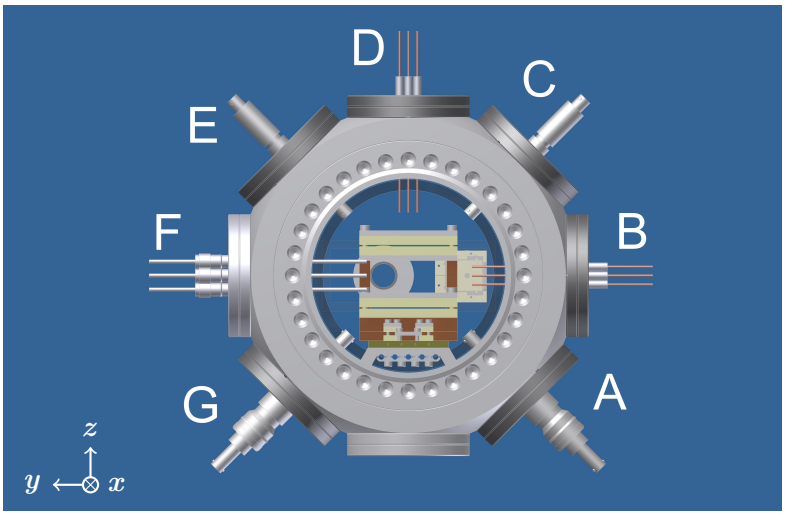

Figure B.1: Labeling of the feedthroughs of the feedthrough octagon. The look through the octagon shows the cable clamp, the experiment cage at the right and the tube, that connects the MOT chamber with the glass cell, at the left.

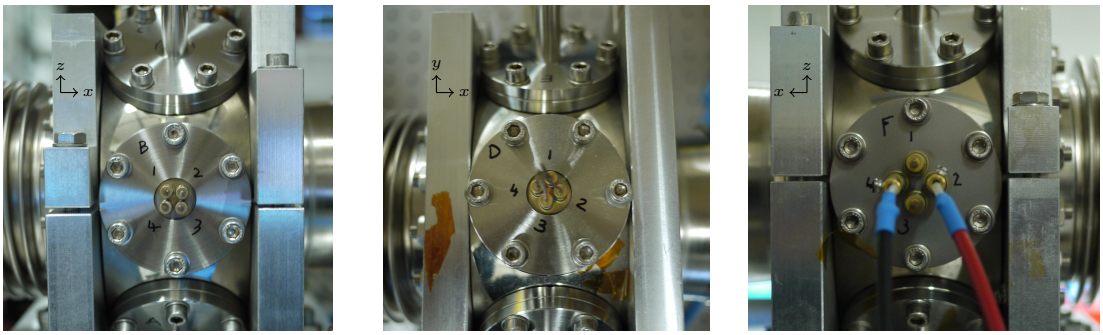

Figure B.2: Labeling of the pins of the 4-pin feedthroughs which are mounted to the feedthrough octagon.

Table B.1 provides the pin assignment of the feedthrough octagon, i. e. it lists which electrode of the experiment cage is connected to which pin of the feedthrough octagon.

feedthrough	pin	connected to
A		rf coil
B	1	MCP detector backplate
	2	top electric field plate
	3	bottom electric field plate
	4	MCP detector frontplate
C		MCP detector anode
D	1	-
	2	MCP detector baseplate
	3	atom side electric field plate
	4	MCP detector electric field plate
E		channeltron anode
F	1	cell wall electric field plate
	2	channeltron backplate
	3	channeltron electric field plate
	4	channeltron frontplate
G		-

Table B.1: The pin assignment of the feedthrough octagon. The six electric field plates are the six Ti plates of the experiment cage. Top and bottom electric field plate are self-explanatory. The MCP detector electric field plate is that Ti plate of the experiment cage which faces the MCP detector. Accordingly, the Ti plate which faces the channeltron is called channeltron electric field plate. The atom side electric field plate is that Ti plate through which the atom cloud enters the experiment cage. Opposite to this plate is the cell wall electric field plate which touches the glass cell wall. The MCP detector baseplate is the holder of the MCP detector through which the detector is mounted to the experiment cage (see figure 4.6).

Danksagung und Eigenständigkeitserklärung

Dank bedeutet ursprünglich „jemanden in seinen Gedanken halten“ [WD07]. Was die vorliegende Arbeit angeht haben sich folgende Personen in meinen Gedanken gehalten: Prof. Dr. Tilman Pfau; Prof. Dr. Peter Michler; Dr. Sebastian Hofferberth; Dr. Robert Löw; Doctor, Graham, Stuart, Lorenzo, Lochead; Michael Schlagmüller; Huan Nguyen; [Tre12]; Hannes Gorniaczyk; Anita & Elena Gaj; Alexander Krupp; Jonathan Balewski sowie Sonne, Mond und Sterne.
Wenn jemand meint, dass mir beim (Ge)denken ein Lapsus passiert ist, sprich, sollte jemand meinen, dass er zu Unrecht aus meinen Gedanken gefallen ist, dann bitte ich darum, dass dieser Jemand oder diese Jemandin sich wieder in meine Gedanken drängt. Auch wenn jemand seinen Namen in serifenloser, fetter, kursiver und roter Schrift abgedruckt sehen will, möge er sich einfach bei mir melden. Nur den Wunsch nach dem Namen in blauer Schrift kann ich natürlich aus offensichtlichen Gründen nicht erfüllen.

Ich habe diese Arbeit selbstständig verfasst und keine anderen als die angegebenen Quellen und Hilfsmittel verwendet.

Thomas Schmid
Stuttgart, den 12. November 2013

References

[Aln08] J. Alnis, A. Matveev, N. Kolachevsky, Th. Udem, and T. W. Hänsch. "Subhertz linewidth diode lasers by stabilization to vibrationally and thermally compensated ultralow-expansion glass Fabry-Pérot cavities". In: *Phys. Rev. A* **77**.5 (May 2008), p. 053809. URL: http://link.aps.org/doi/10.1103/PhysRevA.77.053809.

[And13] Andor Technology plc. *Data sheet for iXon Ultra 897 EMCCD camera*. http://www.andor.com/scientific-cameras/ixon-emccd-camera-series/ixon-ultra-897. July 2013.

[asp13] asphericon GmbH. *Technical data of the aspheric lense 15-12 HPX-S*. http://www.asphericon.net/en/spa-webshop. Sept. 2013.

[AVG98] W. R. Anderson, J. R. Veale, and T. F. Gallagher. "Resonant Dipole-Dipole Energy Transfer in a Nearly Frozen Rydberg Gas". In: *Phys. Rev. Lett.* **80**.2 (Jan. 1998), pp. 249–252. URL: http://link.aps.org/doi/10.1103/PhysRevLett.80.249.

[Bal09] Jonathan B. Balewski. „Hochauflösende Photoassoziationsspektroskopie von Rydberg-Dimeren und Trimeren". Diplomarbeit. Universität Stuttgart, Dez. 2009.

[Bal13] J. B. Balewski, A. T. Krupp, A. Gaj, D. Peter, H. P. Büchler, R. Löw, S. Hofferberth, and T. Pfau. "Coupling a single electron to a Bose-Einstein condensate". In: *ArXiv e-prints* (June 2013). Accepted for pupblication in Nature. arXiv: 1306.5181 [physics.atom-ph].

[Ber10] Karl-Heinz Bernhardt. *Vacuum Technology Compendium*. Pfeiffer Vacuum GmbH, Sept. 2010.

[Bet09] I. I. Beterov, I. I. Ryabtsev, D. B. Tretyakov, and V. M. Entin. "Quasiclassical calculations of blackbody-radiation-induced depopulation rates and effective lifetimes of Rydberg nS, nP, and nD alkali-metal atoms with $n \leq 80$". In: *Phys. Rev. A* **79** (May 2009), p. 052504. URL: http://link.aps.org/doi/10.1103/PhysRevA.79.052504.

[Bla01] Eric D. Black. "An introduction to Pound–Drever–Hall laser frequency stabilization". In: *American Journal of Physics* **69**.1 (2001), pp. 79–87. URL: http://link.aip.org/link/?AJP/69/79/1.

[BPM07] E. Brion, L. H. Pedersen, and K. Mølmer. "Adiabatic elimination in a lambda system". In: *Journal of Physics A: Mathematical and Theoretical* **40**.5 (2007), p. 1033. URL: http://stacks.iop.org/1751-8121/40/i=5/a=011.

[Bra10] D. B. Branden, T. Juhasz, T. Mahlokozera, C. Vesa, R. O. Wilson, M. Zheng, A. Kortyna, and D. A. Tate. "Radiative lifetime measurements of rubidium Rydberg states". In: *Journal of Physics B: Atomic, Molecular and Optical Physics* **43**.1 (2010), p. 015002. URL: http://stacks.iop.org/0953-4075/43/i=1/a=015002.

[Bra13] Branson Ultrasonics Corp. *Material safety data sheet for Branson industrial strength cleaner*. http://www.emersonindustrial.com/en-US/branson/Products/precision-cleaning/cleaning-solutions/industrial-strength/Pages/default.aspx. Mar. 2013.

[BS06] D. M. Brink and C. V. Sukumar. "Majorana spin-flip transitions in a magnetic trap". In: *Phys. Rev. A* **74**.3 (Sept. 2006), p. 035401. URL: http://link.aps.org/doi/10.1103/PhysRevA.74.035401.

[BS68] D. M. Brink and G. R. Satchler. *Angular Momentum*. 2nd ed. Oxford University Press, 1968.

[Buh09] Magnus Buhlert. *Elektropolieren: elektrolytisches Glänzen, Glätten und Entgraten von Edelstahl, Stahl, Messing, Kupfer, Aluminium und Titan*. 1. Aufl. Bad Saulgau: Leuze, 2009.

[BW08] Rainer Blatt and David Wineland. "Entangled states of trapped atomic ions". In: *Nature* **453** (2008), p. 1008. URL: http://dx.doi.org/10.1038/nature07125.

[CB66] Irwin Cohen and Thomas Bustard. "Atomic orbitals: Limitations and variations". In: *Journal of Chemical Education* **43**.4 (1966), p. 187. URL: http://pubs.acs.org/doi/abs/10.1021/ed043p187.

[Cor00] S. L. Cornish, N. R. Claussen, J. L. Roberts, E. A. Cornell, and C. E. Wieman. "Stable ^{85}Rb Bose-Einstein Condensates with Widely Tunable Interactions". In: *Phys. Rev. Lett.* **85**.9 (Aug. 2000), pp. 1795–1798. URL: http://link.aps.org/doi/10.1103/PhysRevLett.85.1795.

[Cor12] Corning Incorporated. *Data sheet MACOR®*. http://www.corning.com/specialtymaterials/products_capabilites/macor.aspx. 2012.

[CW08] John Clarke and Frank K. Wilhelm. "Superconducting quantum bits". In: *Nature* **453** (2008), p. 1031. URL: http://dx.doi.org/10.1038/nature07128.

[Dav04] Joseph R. David, ed. *Metallography and microstructures*. 1st ed. Materials Park, Ohio: ASM International, 2004.

[Dav93] R. S. Davis. "New method to measure magnetic susceptibility". In: *Measurement Science and Technology* **4**.2 (1993), pp. 141–147.

[Dem93] Wolfgang Demtröder. *Laserspektroskopie: Grundlagen und Techniken*. 3. Aufl. Springer, 1993.

[Deu85] D. Deutsch. "Quantum Theory, the Church-Turing Principle and the Universal Quantum Computer". In: *Proceedings of the Royal Society of London. A. Mathematical and Physical Sciences* **400**.1818 (1985), pp. 97–117. URL: http://rspa.royalsocietypublishing.org/content/400/1818/97.abstract.

[DK12] Y. O. Dudin and A. Kuzmich. "Strongly Interacting Rydberg Excitations of a Cold Atomic Gas". In: *Science* **336**.6083 (2012), pp. 887–889. URL: http://www.sciencemag.org/content/336/6083/887.abstract.

[Doh13] Marcus W. Doherty, Neil B. Manson, Paul Delaney, Fedor Jelezko, Jörg Wrachtrup, and Lloyd C. L. Hollenberg. "The nitrogen-vacancy colour centre in diamond". In: *Physics Reports* **528**.1 (2013), pp. 1–45. URL: http://www.sciencedirect.com/science/article/pii/S0370157313000562.

[Dop42] Christian Doppler. *Über das farbige Licht der Doppelsterne und einiger anderer Gestirne des Himmels: Versuch einer das Bradley'sche Aberrations-Theorem als integrirenden Theil in sich schliessenden allgemeineren Theorie*. Borrosch & André, 1842. URL: http://books.google.de/books?id=zl5RAAAAcAAJ.

[Dre83] R. W. P. Drever, J. L. Hall, F. V. Kowalski, J. Hough, G. M. Ford, A. J. Munley, and H. Ward. "Laser phase and frequency stabilization using an optical resonator". In: *Applied Physics B* **31**.2 (1983), pp. 97–105. URL: http://dx.doi.org/10.1007/BF00702605.

[Dud12] Y. O. Dudin, L. Li, F. Bariani, and A. Kuzmich. "Observation of coherent many-body Rabi oscillations". In: *Nature Physics* **8** (2012), p. 790. URL: http://dx.doi.org/10.1038/nphys2413.

[EBH98] Tilman Esslinger, Immanuel Bloch, and Theodor W. Hänsch. "Bose-Einstein condensation in a quadrupole-Ioffe-configuration trap". In: *Phys. Rev. A* **58**.4 (Oct. 1998), R2664–R2667. URL: http://link.aps.org/doi/10.1103/PhysRevA.58.R2664.

[EE10] Jürgen Eichler und Hans Joachim Eichler. *Laser: Bauformen, Strahlführung, Anwendungen*. 7. Aufl. Springer, 2010.

[Fey82] Richard P. Feynman. "Simulating physics with computers". In: *International Journal of Theoretical Physics* **21**.6-7 (1982), pp. 467–488. URL: http://dx.doi.org/10.1007/BF02650179.

[Gae09] Alpha Gaëtan, Yevhen Miroshnychenko, Tatjana Wilk, Amodsen Chotia, Matthieu Viteau, Daniel Comparat, Pierre Pillet, Antoine Browaeys, and Philippe Grangier. "Observation of collective excitation of two individual atoms in the Rydberg blockade regime". In: *Nature Physics* **5** (2009), p. 115. URL: http://dx.doi.org/10.1038/nphys1183.

[Gal94] Thomas F. Gallagher. *Rydberg atoms*. Cambridge University Press, 1994.

[Gre01] Markus Greiner, Immanuel Bloch, Theodor W. Hänsch, and Tilman Esslinger. "Magnetic transport of trapped cold atoms over a large distance". In: *Phys. Rev. A* **63**.3 (Feb. 2001), p. 031401. URL: http://link.aps.org/doi/10.1103/PhysRevA.63.031401.

[Gro11] Jürgen H. Gross. *Mass Spectrometry*. 2nd ed. Springer, 2011.

[Ham08] Hamamatsu Photonics K.K. *Data sheet for MCP detector F4655-13*. http://www.hamamatsu.com/resources/pdf/etd/F4655-13_TMCP1021E05.pdf. Nov. 2008.

[Ham13] Hamamatsu Photonics K.K. *MCP & MCP Assembly - Selection guide*. http://www.hamamatsu.com/resources/pdf/etd/MCPassy_TMCP0001E10.pdf. Apr. 2013.

[Han10] Yang Han, Bing He, Khabat Heshami, Cheng-Zu Li, and Christoph Simon. "Quantum repeaters based on Rydberg-blockade-coupled atomic ensembles". In: *Phys. Rev. A* **81**.5 (May 2010), p. 052311. URL: http://link.aps.org/doi/10.1103/PhysRevA.81.052311.

[Hec02] Eugene Hecht. *Optics*. 4th ed. San Francisco: Addison-Wesley, 2002.

[Hei07] Rolf Heidemann, Ulrich Raitzsch, Vera Bendkowsky, Björn Butscher, Robert Löw, Luis Santos, and Tilman Pfau. "Evidence for Coherent Collective Rydberg Excitation in the Strong Blockade Regime". In: *Phys. Rev. Lett.* **99**.16 (Oct. 2007), p. 163601. URL: http://link.aps.org/doi/10.1103/PhysRevLett.99.163601.

[Hei08] Rolf Heidemann. "Rydberg excitation of Bose-Einstein Condensates: coherent collective dynamics". PhD thesis. Universität Stuttgart, Mar. 2008.

[HH10] Ifan G. Hughes and Thomas P. A. Hase. *Measurements and their Uncertainties*. Oxford University Press, 2010.

[Hol10] Lotte Holmegaard, Jonas L. Hansen, Line Kalhoj, Sofie Louise Kragh, Henrik Stapelfeldt, Frank Filsinger, Jochen Kupper, Gerard Meijer, Darko Dimitrovski, Mahmoud Abu-samha, Christian P. J. Martiny, and Lars Bojer Madsen. "Photoelectron angular distributions from strong-field ionization of oriented molecules". In: *Nature Physics* **6** (2010), p. 428. URL: http://dx.doi.org/10.1038/nphys1666.

[Hon11] Jens Honer, R. Löw, Hendrik Weimer, Tilman Pfau, and Hans Peter Büchler. "Artificial Atoms Can Do More Than Atoms: Deterministic Single Photon Subtraction from Arbitrary Light Fields". In: *Phys. Rev. Lett.* **107**.9 (Aug. 2011), p. 093601. URL: http://link.aps.org/doi/10.1103/PhysRevLett.107.093601.

[Ise10] L. Isenhower, E. Urban, X. L. Zhang, A. T. Gill, T. Henage, T. A. Johnson, T. G. Walker, and M. Saffman. "Demonstration of a Neutral Atom Controlled-NOT Quantum Gate". In: *Phys. Rev. Lett.* **104**.1 (Jan. 2010), p. 010503. URL: http://link.aps.org/doi/10.1103/PhysRevLett.104.010503.

[Ita04] J. Itatani, J. Levesque, D. Zeidler, Hiromichi Niikura, H. Pepin, J. C. Kieffer, P. B. Corkum, and D. M. Villeneuve. "Tomographic imaging of molecular orbitals". In: *Nature* **432** (2004), p. 867. URL: http://dx.doi.org/10.1038/nature03183.

[Jak00] D. Jaksch, J. I. Cirac, P. Zoller, S. L. Rolston, R. Côté, and M. D. Lukin. "Fast Quantum Gates for Neutral Atoms". In: *Phys. Rev. Lett.* **85**.10 (Sept. 2000), pp. 2208–2211. URL: http://link.aps.org/doi/10.1103/PhysRevLett.85.2208.

[Jen12] Daniel L. Jenkin. "Feshbach spectroscopy of an ultracold Rb-Cs mixture". PhD thesis. Durham University, 2012.

[Jul97] P. S. Julienne, F. H. Mies, E. Tiesinga, and C. J. Williams. "Collisional Stability of Double Bose Condensates". In: *Phys. Rev. Lett.* **78**.10 (Mar. 1997), pp. 1880–1883. URL: http://link.aps.org/doi/10.1103/PhysRevLett.78.1880.

[KD96] Wolfgang Ketterle and N.J. Van Druten. "Evaporative Cooling of Trapped Atoms". In: *Advances In Atomic, Molecular, and Optical Physics* **37** (1996). Ed. by Benjamin Bederson and Herbert Walther, pp. 181–236. URL: http://www.sciencedirect.com/science/article/pii/S1049250X08601019.

[KDS99] W. Ketterle, D. Durfee, and D. M. Stamper-Kurn. "Making, probing and understanding Bose-Einstein condensates". In: *Bose-Einstein Condensation in Atomic Gases*. Ed. by S. Stringari, M. Inguscio, and C. E. Wieman. IOS Press, 1999, pp. 67–176.

[KL13] C. Kloeffel and D. Loss. "Prospects for Spin-Based Quantum Computing in Quantum Dots". In: *Annual Review of Condensed Matter Physics* **4**.1 (2013), pp. 51–81. URL: http://www.annualreviews.org/doi/abs/10.1146/annurev-conmatphys-030212-184248.

[Kur09] Kurt J. Lesker Company. *Data sheet for Kapton® insulated wires*. http://www.lesker.com/newweb/literature/CDC/catalog_download.cfm. Nov. 2009.

[Lem01] Serge G. Lemay, Jorg W. Janssen, Michiel van den Hout, Maarten Mooij, Michael J. Bronikowski, Peter A. Willis, Richard E. Smalley, Leo P. Kouwenhoven, and Cees Dekker. "Two-dimensional imaging of electronic wavefunctions in carbon nanotubes". In: *Nature* **412** (2001), p. 617. URL: http://dx.doi.org/10.1038/35088013.

[Li03] Wenhui Li, I. Mourachko, M. W. Noel, and T. F. Gallagher. "Millimeter-wave spectroscopy of cold Rb Rydberg atoms in a magneto-optical trap: Quantum defects of the *ns*, *np*, and *nd* series". In: *Phys. Rev. A* **67**.5 (May 2003), p. 052502. URL: http://link.aps.org/doi/10.1103/PhysRevA.67.052502.

[Lid10] David R. Lide, ed. *CRC Handbook of Chemistry and Physics*. 90th ed. CRC Press, 2010.

[LLL11] Ariel Lipson, Stephen G. Lipson, and Henry S. Lipson. *Optical physics*. 4th ed. Cambridge Univ. Press, 2011.

[Low12] Robert Löw, Hendrik Weimer, Johannes Nipper, Jonathan B Balewski, Björn Butscher, Hans Peter Büchler, and Tilman Pfau. "An experimental and theoretical guide to strongly interacting Rydberg gases". In: *Journal of Physics B: Atomic, Molecular and Optical Physics* **45**.11 (2012), p. 113001. URL: http://stacks.iop.org/0953-4075/45/i=11/a=113001.

[Luk01] M. D. Lukin, M. Fleischhauer, R. Cote, L. M. Duan, D. Jaksch, J. I. Cirac, and P. Zoller. "Dipole Blockade and Quantum Information Processing in Mesoscopic Atomic Ensembles". In: *Phys. Rev. Lett.* **87**.3 (June 2001), p. 037901. URL: http://link.aps.org/doi/10.1103/PhysRevLett.87.037901.

[Mac11] Markus Mack, Florian Karlewski, Helge Hattermann, Simone Höckh, Florian Jessen, Daniel Cano, and József Fortágh. "Measurement of absolute transition frequencies of ^{87}Rb to nS and nD Rydberg states by means of electromagnetically induced transparency". In: *Phys. Rev. A* **83**.5 (2011), p. 052515. URL: http://link.aps.org/doi/10.1103/PhysRevA.83.052515.

[MC05] I. Martinson and L. J. Curtis. "Janne Rydberg – his life and work". In: *Nuclear Instruments and Methods in Physics Research Section B: Beam Interactions with Materials and Atoms* **235** (2005), pp. 17–22. URL: http://www.sciencedirect.com/science/article/pii/S0168583X05003617.

[Mep10] R. Meppelink, R. A. Rozendaal, S. B. Koller, J. M. Vogels, and P. van der Straten. "Thermodynamics of Bose-Einstein-condensed clouds using phase-contrast imaging". In: *Phys. Rev. A* **81**.5 (May 2010), p. 053632. URL: http://link.aps.org/doi/10.1103/PhysRevA.81.053632.

[MI95] Michio Minato and Yoshio Itoh. "Vacuum characteristics of titanium". In: *Journal of Vacuum Science Technology A: Vacuum, Surfaces, and Films* **13**.3 (1995), pp. 540–544.

[Mou98] I. Mourachko, D. Comparat, F. de Tomasi, A. Fioretti, P. Nosbaum, V. M. Akulin, and P. Pillet. "Many-Body Effects in a Frozen Rydberg Gas". In: *Phys. Rev. Lett.* **80**.2 (Jan. 1998), pp. 253–256. URL: http://link.aps.org/doi/10.1103/PhysRevLett.80.253.

[MS99] Harold J. Metcalf and Peter van der Straten. *Laser Cooling and Trapping*. Springer, 1999.

[MSD94] M. Marinescu, H. R. Sadeghpour, and A. Dalgarno. "Dispersion coefficients for alkali-metal dimers". In: *Phys. Rev. A* **49**.2 (Feb. 1994), pp. 982–988. URL: http://link.aps.org/doi/10.1103/PhysRevA.49.982.

[MV99] Kurt Meyberg und Peter Vachenauer. *Höhere Mathematik 2 - Differentialgleichungen, Funktiontheorie, Fourier-Analysis, Variationsrechnung*. 3. Aufl. Springer, 1999.

[Naz89] M. Nazarathy, W. V. Sorin, D. M. Baney, and S. A. Newton. "Spectral analysis of optical mixing measurements". In: *Journal of Lightwave Technology* **7**.7 (1989), pp. 1083–1096.

[Nol06] Wolfgang Nolting. *Grundkurs Theoretische Physik 5/2: Quantenmechanik - Methoden und Anwendungen*. 6. Aufl. Springer, 2006.

[OL77] J. J. Olivero and R. L. Longbothum. "Empirical fits to the Voigt line width: A brief review". In: *Journal of Quantitative Spectroscopy and Radiative Transfer* **17**.2 (1977), pp. 233–236. URL: http://www.sciencedirect.com/science/article/pii/0022407377901613.

[OS85] M. S. O'Sullivan and B. P. Stoicheff. "Scalar polarizabilities and avoided crossings of high Rydberg states in Rb". In: *Phys. Rev. A* **31**.4 (Apr. 1985), pp. 2718–2720. URL: http://link.aps.org/doi/10.1103/PhysRevA.31.2718.

[Pfe11] Pfeiffer Vacuum GmbH. *HiCube™ Turbopumpstände*. http://www.pfeiffer-vacuum.de/produkte/pumpstaende/turbopumpstaende/container.action. Sep. 2011.

[PHO09] PHOTONIS. *Data sheet for MAGNUM™ electron mulitplier 5900 series*. http://www.photonis.com/en/ism/59-magnum-electron-multipliers.html. Nov. 2009.

[Pri11] Jonathan D. Pritchard. "Cooperative Optical Non-linearity in a blockaded Rydberg Ensemble". PhD thesis. Durham University, 2011.

[PS08] C. J. Pethick and H. Smith. *Bose-Einstein Condensation in Dilute Gases*. 2nd ed. Cambridge Univ. Press, 2008.

[Pus09] Peter Puschnig, Stephen Berkebile, Alexander J. Fleming, Georg Koller, Konstantin Emtsev, Thomas Seyller, John D. Riley, Claudia Ambrosch-Draxl, Falko P. Netzer, and Michael G. Ramsey. "Reconstruction of Molecular Orbital Densities from Photoemission Data". In: *Science* **326**.5953 (2009), pp. 702–706. URL: http://www.sciencemag.org/content/326/5953/702.abstract.

[Rep05] Jascha Repp, Gerhard Meyer, Sladjana M. Stojković, André Gourdon, and Christian Joachim. "Molecules on Insulating Films: Scanning-Tunneling Microscopy Imaging of Individual Molecular Orbitals". In: *Phys. Rev. Lett.* **94**.2 (2005), p. 026803. URL: http://link.aps.org/doi/10.1103/PhysRevLett.94.026803.

[RS85] A. A. Radzig and B. M. Smirnov. *Reference Data on Atoms, Molecules, and Ions*. Springer, 1985.

[Rui12] Han Rui. "Robust quantum storage with three atoms". PhD thesis. Centre for Quantum Technologies, National University of Singapore, 2012.

[San06] J. E. Sansonetti. "Wavelengths, Transition Probabilities, and Energy Levels for the Spectra of Rubidium (Rb I through Rb XXXVII)". In: *Journal of Physical and Chemical Reference Data* **35**.1 (2006), pp. 301–421. URL: http://link.aip.org/link/?JPR/35/301/1.

[SC09] J. Stanojevic and R. Côté. "Many-body Rabi oscillations of Rydberg excitation in small mesoscopic samples". In: *Phys. Rev. A* **80**.3 (Sept. 2009), p. 033418. URL: http://link.aps.org/doi/10.1103/PhysRevA.80.033418.

[Sch00] Rainer Scheunemann. „Lichtgebundene Atome: Manipulation kalter Atome in mesoskopischen optischen Gittern". Doktorarbeit. Ludwig-Maximilians Universität München, Dez. 2000.

[Sch07] Franz Schwabl. *Quantenmechanik (QM I): Eine Einführung*. 7. Aufl. Springer, 2007.

[Sch11] Adolf Schwab. *Elektromagnetische Verträglichkeit*. 6. Aufl. Springer, 2011.

[Sch26] Erwin Schrödinger. "An Undulatory Theory of the Mechanics of Atoms and Molecules". In: *Phys. Rev.* **28**.6 (Dec. 1926), pp. 1049–1070. URL: http://link.aps.org/doi/10.1103/PhysRev.28.1049.

[Sho95] P. W. Shor. "Polynomial-Time Algorithms for Prime Factorization and Discrete Logarithms on a Quantum Computer". In: *ArXiv e-prints* (Aug. 1995). URL: http://arxiv.org/abs/quant-ph/9508027v2.

[Sin04] Kilian Singer, Markus Reetz-Lamour, Thomas Amthor, Luis Gustavo Marcassa, and Matthias Weidemüller. "Suppression of Excitation and Spectral Broadening Induced by Interactions in a Cold Gas of Rydberg Atoms". In: *Phys. Rev. Lett.* **93**.16 (Oct. 2004), p. 163001. URL: http://link.aps.org/doi/10.1103/PhysRevLett.93.163001.

[ST07] Bahaa Saleh and Malvin Carl Teich. *Fundamentals of Photonics*. 2nd ed. Wiley, 2007.

[Ste10] Daniel A. Steck. *Rubidium 87 D Line Data*. http://steck.us/alkalidata. Revision 2.1.4. Dec. 2010.

[Ste13] Daniel A. Steck. *Rubidium 85 D Line Data*. http://steck.us/alkalidata. Revision 2.1.6. Sept. 2013.

[Sto13] A. S. Stodolna, A. Rouzée, F. Lépine, S. Cohen, F. Robicheaux, A. Gijsbertsen, J. H. Jungmann, C. Bordas, and M. J. J. Vrakking. "Hydrogen Atoms under Magnification: Direct Observation of the Nodal Structure of Stark States". In: *Phys. Rev. Lett.* **110**.21 (May 2013), p. 213001. URL: http://link.aps.org/doi/10.1103/PhysRevLett.110.213001.

[SWC04] M. S. Safronova, Carl J. Williams, and Charles W. Clark. "Relativistic many-body calculations of electric-dipole matrix elements, lifetimes, and polarizabilities in rubidium". In: *Phys. Rev. A* **69** (Feb. 2004), p. 022509. URL: http://link.aps.org/doi/10.1103/PhysRevA.69.022509.

[SWM10] M. Saffman, T. G. Walker, and K. Mølmer. "Quantum information with Rydberg atoms". In: *Rev. Mod. Phys.* **82** (Aug. 2010), pp. 2313–2363. URL: http://link.aps.org/doi/10.1103/RevModPhys.82.2313.

[SZ08] Marlan O. Scully and Muhammad S. Zubairy. *Quantum optics*. 6th ed. Cambridge Univ. Press, 2008.

[The05] Matthias Theis. "Optical Feshbach Resonances in a Bose-Einstein Condensate". PhD thesis. Leopold-Franzens Universität Innsbruck, Apr. 2005.

[Ton04] D. Tong, S. M. Farooqi, J. Stanojevic, S. Krishnan, Y. P. Zhang, R. Côté, E. E. Eyler, and P. L. Gould. "Local Blockade of Rydberg Excitation in an Ultracold Gas". In: *Phys. Rev. Lett.* **93**.6 (Aug. 2004), p. 063001. URL: http://link.aps.org/doi/10.1103/PhysRevLett.93.063001.

[TOP12] TOPTICA Photonics AG. *Lasers for Scientific Challenges - Catalog 2011/2012*. http://www.toptica.com/uploads/media/toptica_BR_product_catalog_48.pdf. Jan. 2012.

[Tre12] Christoph Tresp. „A setup for highly precise excitation and detection of Rydberg atoms“. Masterarbeit. Universität Stuttgart, Okt. 2012.

[Var08] T. Varzhapetyan, A. Nersisyan, V. Babushkin, D. Sarkisyan, S. Vdović, and G. Pichler. “Study of atomic transition self-broadening and shift with the help of a nano-cell”. In: *Journal of Physics B: Atomic, Molecular and Optical Physics* **41**.18 (2008), p. 185004. URL: http://stacks.iop.org/0953-4075/41/i=18/a=185004.

[Vdo00] E. E. Vdovin, A. Levin, A. Patanè, L. Eaves, P. C. Main, Yu. N. Khanin, Yu. V. Dubrovskii, M. Henini, and G. Hill. “Imaging the Electron Wave Function in Self-Assembled Quantum Dots”. In: *Science* **290**.5489 (2000), pp. 122–124. URL: http://www.sciencemag.org/content/290/5489/122.abstract.

[Vit11] M. Viteau, J. Radogostowicz, M. G. Bason, N. Malossi, D. Ciampini, O. Morsch, and E. Arimondo. “Rydberg spectroscopy of a Rb MOT in the presence of applied or ion created electric fields”. In: *Opt. Express* **19**.7 (Mar. 2011), pp. 6007–6019. URL: http://www.opticsexpress.org/abstract.cfm?URI=oe-19-7-6007.

[Wad07] C. L. Wadhwa. *High voltage engineering*. 2nd ed. New Age International Publishers, 2007.

[WD07] Matthias Wermke und Günther Drosdowski, Hrsg. *Duden - Das Herkunftswörterbuch: Etymologie der deutschen Sprache*. 4. Aufl. Dudenverlag, 2007.

[Wei10] Hendrik Weimer, Markus Müller, Igor Lesanovsky, Peter Zoller, and Hans Peter Büchler. “A Rydberg quantum simulator”. In: *Nature Physics* **6** (2010), p. 382. URL: http://dx.doi.org/10.1038/nphys1614.

[Wer74] G. K. Wertheim, M. A. Butler, K. W. West, and D. N. E. Buchanan. “Determination of the Gaussian and Lorentzian content of experimental line shapes”. In: *Review of Scientific Instruments* **45**.11 (1974), pp. 1369–1371. URL: http://link.aip.org/link/?RSI/45/1369/1.

[Whi34] Harvey Elliott White. *Introduction to atomic spectra*. McGraw-Hill Book Company, 1934.

[Wil10] T. Wilk, A. Gaëtan, C. Evellin, J. Wolters, Y. Miroshnychenko, P. Grangier, and A. Browaeys. “Entanglement of Two Individual Neutral Atoms Using Rydberg Blockade”. In: *Phys. Rev. Lett.* **104**.1 (Jan. 2010), p. 010502. URL: http://link.aps.org/doi/10.1103/PhysRevLett.104.010502.

[Wil11] Sebastian Will. “Interacting bosons and fermions in three-dimensional optical lattice potentials”. PhD thesis. Johannes Gutenberg Universität Mainz, Sept. 2011.

[Win84] William H. Wing. "On neutral particle trapping in quasistatic electromagnetic fields". In: *Progress in Quantum Electronics* **8** (1984), pp. 181–199. URL: http://www.sciencedirect.com/science/article/pii/0079672784900120.

[Wiz79] Joseph Ladislas Wiza. "Microchannel plate detectors". In: *Nuclear Instruments and Methods* **162** (1979), pp. 587–601. URL: http://www.sciencedirect.com/science/article/pii/0029554X79907341.

[Woo83] G. K. Woodgate. *Elementary Atomic Structure*. 2nd ed. Oxford University Press, 1983.

[Zha10] Bo Zhao, Markus Müller, Klemens Hammerer, and Peter Zoller. "Efficient quantum repeater based on deterministic Rydberg gates". In: *Phys. Rev. A* **81**.5 (May 2010), p. 052329. URL: http://link.aps.org/doi/10.1103/PhysRevA.81.052329.